A sensitivity study on the effect of blade sweep on the trade-off between propeller efficiency and noise with panel method analysis

T. H. Keil

Technische Universiteit Delft

Cover image by: E. Hughes https://unsplash.com/photos/3xvPgpquX4s

A sensitivity study on the effect of blade sweep on the trade-off between propeller efficiency and noise with panel method analysis

by

T. H. Keil

to obtain the degree of
Master of Science
at the Delft University of Technology,
to be defended publicly on Wednesday October 27, 2021 at 14:00.

Student number:	4155637		
Thesis committee:	Dr. ir. T. Sinnige,	TU Delft	Supervisor, Assistant Professor
	Prof. dr. ing. G. Eitelberg,	TU Delft	Full Professor
	dr. J. Sodja,	TU Delft	Senior Researcher
	dr. F. Avallone	TU Delft	Assistant Professor

An electronic version of this thesis is available at http://repository.tudelft.nl/.

TU Delft Delft University of Technology

Preface

This Master thesis report will be the final deliverable in my studies before I can call myself an Aerospace Engineer. I can say with certainty that this project has been one of the longest in my life with a lot of ups and downs. As I am writing this, I am glad to say that it is almost completed.

I have received a lot of support from a number of people during this project which I would like to acknowledge here. First and foremost, I would like to thank my family, for their unconditional love, (financial) support and encouragement during the entire time of my studies in Delft. It has been invaluable to me. Secondly, I would like to thank all the friends that I have made during my studies, who stood beside me all the time and has made my study time one to cherish and unforgettable. My thanks to my housemates Pjotr, Max and Hubald who have had to endure me while working on this thesis. A special thanks to Hubald for the ”extraordinary” kind of support in these last couple of months :). Shout-out to my friends from WTOS: Robin, Marlon, Lars, and Arjan for all the apple pie and choco mit sahne rides, but also the utterly exhausting ones that we have made so far. A wise man once said that pain is temporarily, but victory is permanent. I am looking forward to the road that lies ahead of us! Victor, thanks for being an excellent listener, your great sense of humor, and for pulling me through the final phase of this thesis project.

From the TU Delft, I would first like to thank Tomas for the guidance and feedback during the complete duration of the thesis. Secondly, I would like to thank Akshay Raju Kulkarni for the support regarding ParaPy.

Last but not least, I would like to thank Vivek Ahuja from Research in Flight for allowing me to conduct my research with FlightStream, and for the support during the project’s duration.

T. H. Keil
Delft, October 2021

Summary

In the last decades, the rise in fuel prices and increased awareness of the environmental impact of aviation have led to the desire for more fuel-efficient aircraft. As a result, there is a renewed interest in the field of propeller propulsion systems. Propellers can reduce the fuel consumption for future aircraft with respect to turbofan engines due to the high effective bypass ratios. Besides the potential fuel-saving benefits, they also have the potential to reduce the environmental impact of future aircraft in the form of electric propulsion. However, propellers, unlike turbofans, do not have ducts that contain the noise. As a result, propellers are generally associated with higher noise levels. Studies have been conducted to determine how the noise emissions of isolated propellers can be reduced while maintaining a high propeller efficiency. The studies indicate that blade sweep plays an important role in the trade-off between propeller efficiency and noise. However, a quantitative assessment of this trade-off is still missing. Furthermore, the studies highlight that the choice of the numerical model is important since this determines the accuracy with which the effect of sweep on the trade-off is assessed.

In this thesis, the effect of blade sweep on the trade-off between propeller efficiency and noise for an isolated propeller is quantified by means of a sensitivity study. The propeller aerodynamics are assessed using the commercial panel method FlightStream. The panel method employs the method of integrated circulation to convert the arbitrarily oriented vorticity into directed circulation distributions. Comparison of the panel method with experimental data shows disagreement in the prediction of the propeller efficiency, especially at a high advance ratio. The offset of the panel method with respect to experimental data is likely due to neglecting viscosity. The propeller aeroacoustics are assessed using Hanson's frequency-domain formulation. This formulation has been validated previously by Parry. The propeller blade geometry is generated using the *Multi-Model Generator*, which is a tool based on the knowledge-based-engineering platform ParaPy. An automated workflow was created to analyze the propeller aerodynamics and acoustics, which includes the panel method, the tonal far-field formulation from Hanson, and the Multi-Model Generator tool. Besides the propeller blades, also a nacelle geometry is modeled. The nacelle geometry that was used is adapted from the baseline propeller and is kept constant in the thesis. The baseline propeller in the thesis is the 6-bladed XPROP propeller with a diameter of 0.4064 m. Next to these methods, a Bézier curve implementation is used to parameterize the radial distribution of blade sweep, and a Sobol sequence is used in the Design of Experiments.

In this thesis, 1000 different swept propeller blade designs are evaluated. Other blade parameters such as the airfoil shape, chord distribution, and twist distribution are kept constant throughout the thesis and are equal to the design of the baseline propeller. Also, the advance ratio is kept constant. Each blade is evaluated at three pitch angles. Then the three observations are interpolated for each design to estimate the efficiency and noise at $T_c = T/\rho_\infty V_\infty^2 D^2 = 0.0371$. This value is obtained by using the ATR72-500 aircraft as reference aircraft.

In the study, 767 out of 1000 designs were evaluated successfully. Investigation of the predicted noise components shows that the thickness noise was dominant for all designs. The mean Thrust Specific Sound Pressure (TSSP) due to the thickness source is -130 dB, while the mean TSSP due to the axial and tangential loading sources were -148.7 and -140.7 dB, respectively. Investigation of the loading noise showed discrepancies in the radial blade loading distributions predicted by the panel method. This means that the loading noise component in the thesis is not predicted accurately. However, the acoustic benefit of sweep on the thickness noise component is still captured.

Analysis of the propeller efficiency and noise results of all designs showed a spread of 4.4 dB in TSSP and 7.7 % in propeller efficiency. The majority of designs form a point cloud, where the propeller efficiency is in between 80 and 90 %. However, the efficiency of several designs is significantly lower than this point cloud.

The relation of sweep on the propeller efficiency and noise was investigated. The effect is assessed by splitting the propeller blade into three segments of equal radial length. For the efficiency results, it is concluded that a blade with moderate forward swept mid segment and a backward swept tip is most favorable in terms of the propeller efficiency. As was indicated in the study by Burger, forward sweep can lead to a favorable radial blade loading distribution, thereby explaining the higher efficiency. No distinct relation between sweep angle and propeller efficiency for the root segment was found. For the noise results, it was concluded that a higher forward or backward sweep angle for all three segments leads to lower noise. A higher sweep angle is associated with a higher mid-chord alignment, which is related to the amount of phase delay. As mentioned by Hanson, the amount of total noise reduction depends on the relative phase between the stations. When comparing the results of this study to those from Burger, similar trends for the effect of sweep on the propeller efficiency and noise were seen, except for the root segment sweep and the propeller efficiency. The difference in results may be explained by the difference in parameterizations.

Four designs represent the Pareto front between propeller efficiency and noise. The spread in terms of efficiency is roughly 5.5 %, while the spread in TSSP is 2 dB. A power-law function is applied to the Pareto front. From the numerical fit, the gradient is determined. This quantification shows that the amount of noise reduction decreases as the amount of allowable penalty in the propeller efficiency is increased. The results highlight that propeller efficiency and noise emissions are conflicting requirements. At the design point of maximum efficiency, the gradient is equal to 4.48 dB change in TSSP for a penalty of 1% in efficiency, while at the design point of minimum noise, the gradient is approximately 2×10^{-5} dB per 1% penalty in the propeller efficiency. This shows that the penalty in the propeller efficiency to achieve a certain amount of noise emission reduction is relatively low for propeller designs that are close to the design point of maximum efficiency, while the penalty in the propeller efficiency becomes relatively high for designs that have already achieved a particular reduction in noise emissions. The knowledge from this thesis can be used to reduce the noise emissions of future propellers more effectively.

Contents

List of Figures

List of Tables

Nomenclature

Greek Symbols

α	Angle of attack	[rad]
β	Blade twist angle	[rad]
$\beta_{.7R}$	Blade pitch angle with respect to the station at 70 % of the propeller radius	[rad]
η	$\frac{c_T}{c_P}J$, Propeller efficiency	
η_p	$\eta_p = \frac{2}{2+\Delta V/V_\infty}$. Propulsive efficiency	
Λ	Blade sweep angle	[rad]
Ω	Shaft rotation frequency times 2π	[rad/s]
ω	Wavenumber integration variable	
ω_0	$\frac{n+q}{1-M_x\cos\theta}$, Stationary phase point	
Ω_D	$\frac{\Omega}{1-M_x\cos\theta}$	[rad/s]
ϕ	Inflow angle	[rad]
ϕ	Perturbation velocity potential	
ϕ_i	Phase lag of radial section j	
ϕ_o	Phase lag due to offset or Face Alignment	
ϕ_s	Phase lag due to sweep or Mid-chord Alignment	
ψ_V	Transform of thickness source term	
ψ_X	Transform of axial loading source term	
ψ_Z	Transform of tangential loading source term	
ρ	Fluid density	[kg /m^3]
σ	$\frac{U}{V}$, Ratio of local blade section speed to flight speed	
θ	Radiation angle from propeller axis to observer	[rad]

Latin Symbols

$\dot{m}$	Mass flow	[kg/s]
a	Ratio of tip speed to flight speed	
A_j	Noise amplitude of radial section j	
A_R	Noise amplitude resultant over all radial sections	
B	Number of blades	

c	Chord length	[m]
c_0	Speed of sound	[m/s]
c_D	Drag coefficient	
c_L	Lift coefficient	
c_P	$\frac{P}{\rho n^3 D^5}$, Power coefficient	
c_Q	$\frac{Q}{\rho n^2 D^5}$, Torque coefficient	
c_T	$\frac{T}{\rho n^2 D^4}$, Thrust coefficient	
C_x	Force coefficient in the X-direction of the specified coordinate system defined in FlightStream, see Equation (3.4)	
$c_{f_x}(z)$	Axial force coefficient at radial coordinate z	
$c_{f_\phi}(z)$	Tangential force coefficient at radial coordinate z	
C_{M_x}	Moment coefficient about the X-direction of the specified coordinate system defined in FlightStream, see Equation (3.5)	
D	Drag	[N]
D	Propeller diameter	[m]
D'	Drag per unit span	$\mathrm{N\,m^{-1}}$
F	Force	[N]
$f_X(X)$	Axial loading shape function	
$f_\phi(X)$	Tangential loading shape function	
FA	Face Alignment, see Figure 4.1	
$H(X)$	Thickness shape function	
J	$\frac{V_\infty}{nD}$, Advance ratio	
L	Lift	[N]
L'	Lift per unit span	[N/m]
L_{ref}	Reference length used to nondimensionalize the force and moments in FlightStream	[m]
M	Mach number	
m	Harmonic of blade passing frequency	
M_r	$\sqrt{M_x^2 + z^2 M_T^2}$, Section relative Mach number	
M_T	$\frac{V_T}{c_0}$, Tip Mach number	
M_x	$\frac{V_\infty}{c_0}$, Free stream Mach number	
MCA	Mid-chord Alignment, see Figure 4.1	
n	mB, Harmonic of shaft frequency	

n	Shaft rotation frequency	[Hz]
N_{crit}	Critical amplification factor	
P	Shaft Power	[W]
p	Acoustic pressure	[Pa]
p_0	Reference acoustic pressure	[Pa]
p_∞	Ambient pressure	[Pa]
p_{rms}	Root mean square form of the acoustic pressure	[Pa]
P_{Vm}	Volume component of complex Fourier coefficient at mth harmonic	
P_{Xm}	Axial loading component of complex Fourier coefficient at mth harmonic	
P_{Zm}	Tangential loading component of complex Fourier coefficient at mth harmonic	
Q	Torque	[Nm]
q	$\frac{1}{2}\rho V^2$, Dynamic pressure	[Pa]
q	Unsteady loading order	
R	Gas constant	[J/kgK]
r	Radial coordinate	[m]
R_t	Propeller radius	[m]
Re	Reynolds number	
S_{ref}	Reference area used to nondimensionalize the force and moments in FlightStream	[m^2]
SPL	Sound pressure level	[dB]
T	Temperature	[K]
T	Thrust	[N]
t	Observer time	[s]
t	Time	[s]
t_b	Maximum thickness-to-chord ratio	
T_c	$\frac{T}{\rho_\infty V_\infty^2 D^2}$, Thrust coefficient with respect to freestream velocity	
$TSSP$	Thrust Specific Sound Pressure	[dB]
V	Velocity	[m/s]
V_∞	Free stream velocity	[m/s]
V_{ref}	Reference velocity used to nondimensionalize the force and moments in FlightStream	[m/s]
W	Weight	[N]
w_a	Induced velocity in axial direction	[m/s]
w_t	Induced velocity in tangential direction	[m/s]
X	x/c Normalized chordwise coordinate	

x	Design variable	
x_{CP_i}	X-coordinate of the i-th control point	
y	Observer distance from propeller axis,	[m]
y_{CP_i}	Y-coordinate of the i-th control point	
z	r/R, Normalized radial coordinate	

I

Background

1

Introduction

When the Wright brothers achieved the first-ever successful powered heavier-than-air controlled flight, they relied on propellers to generate thrust. In the decades that followed the historic achievement, propellers became the primary propulsion system for aircraft. Since propellers were driven by piston engines, the performance of the aircraft was limited in terms of the service ceiling and flight velocity. However, at the end of the Second World War, a radically new propulsion system overcame these drawbacks: the jet engine. Since jet engines allowed aircraft to achieve higher flight speeds than propellers, this became the dominant propulsion type for most passenger transport aircraft until today. However, in the last few decades, increased awareness about the environmental impact of aviation and rising fuel prices have led to a desire for more fuel-efficient aircraft. Due to their higher propulsive efficiency, there is a renewed interest in propeller propulsion systems.

The reason for the high potential propulsive efficiency can be explained with two equations:

$$T = \dot{m}\Delta V \tag{1.1}$$

$$\eta_p = \frac{2}{2 + \Delta V / V_\infty} \tag{1.2}$$

In the first equation, the thrust is defined as the product of the mass flow: $\dot{m}$ and the velocity increment of the accelerated flow: ΔV. Equation (1.2) shows that a high propulsive efficiency is achieved if the velocity increment with respect to the freestream: $\Delta V / V_\infty$, is decreased. Thus, it can be seen that in order to achieve a high propulsive efficiency, the thrust should be produced with a high mass flow instead of with a high velocity increment. Propellers, in general, accelerate large mass flows with a small increment, and thus they can achieve a high propulsive efficiency. This is further illustrated in Figure 1.1, where the propulsive efficiency of a turboprop is higher than the propulsive efficiency of a turbofan. As a result of the higher propulsive efficiency, there is a renewed interest in turboprop aircraft [1, 2].

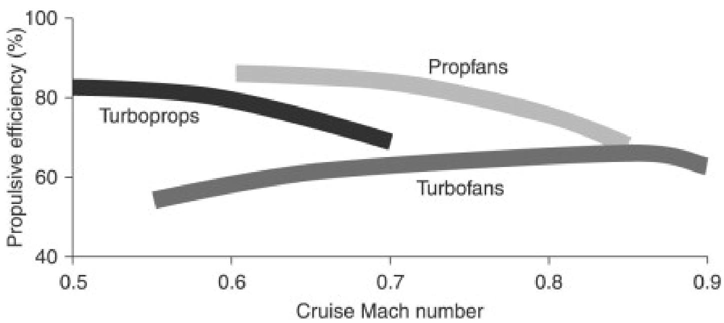

Figure 1.1: Propulsive efficiency for different propulsion systems [3]

Besides the higher potential propulsive efficiency, research interest in propellers has been regained due to the potential benefits of electric propulsion. Electric propulsion provides several potential benefits compared to propulsion systems relying on fossil fuels [4]:

- Carbon emission reduction
- Cost per unit energy reduction
- Decoupling of propulsive device and power system
- Engine scalability [5]
- Energy recuperation [6]

Propellers are ideal propulsive devices for electric aircraft since they can be scaled and connected to electric motors. They are used in drones of all kinds of sizes, in Unmanned Aerial Vehicles (UAVs), and on all-electric trainer aircraft [7]. Due to the engine scalability of electric engines, distributed electric propulsion (DEP) aircraft concepts are enabled. For such aircraft, the thrust is generated by a series of propellers mounted on the airframe. An example of an aircraft with a distributed electric propulsion system is NASA's X-57 Maxwell, which is shown in Figure 1.2.

Figure 1.2: Artist impression of the NASA X-57 Maxwell [1]

Despite their potential fuel-saving benefits, propellers are associated with higher noise levels. This is because, unlike turbofan engines, propeller propulsion systems do not have ducts that contain the noise. As propellers are exposed to the freestream air, their flight velocity is limited due to the tip Mach number. If the tip Mach number is high, shock waves can appear, leading to a high drag. A high tip Mach number will also lead to excessive noise emissions. Studies have assessed the effect of excessive noise levels on the health of people living near airports. They highlight that exposure to high aircraft noise levels causes sleep deprivation [8], and can lead to other detrimental health effects [9, 10]. A reduction in the noise emissions could lead to more widespread use of the propeller, which ultimately can lead to a reduction in environmental impact. This can be achieved by careful design of the propeller blade.

The propeller blade design heavily depends on the design objective that is to be achieved. If there are multiple objectives, there will be a compromise in the design. For example, if the design objectives are to maximize the propeller efficiency and minimize the propeller noise, the resulting design will be a trade-off between the two objectives. In a study by Miller et al. [11], the effect of a number of blade parameters on the trade-off between propeller efficiency and propeller noise was investigated with respect to a straight-bladed propeller. The study shows that the most beneficial approach to improve both the aerodynamic and acoustic performance is to increase the number of blades, while the second most beneficial approach is to apply blade sweep [11]. Figure 1.3 shows an example of swept blades from the propeller of the C130 Hercules.

[1]Credits: NASA Graphic / NASA Langley/Advanced Concepts Lab, AMA, Inc
[2]Credits: Timothy Newman, https://unsplash.com/photos/qFs9XEFwqE8

Figure 1.3: Propeller blades of the C130 Hercules at the Singapore Airshow [2]

More recently, a number of optimization studies have been conducted with varying objective functions, constraints, and varying aerodynamic and aeroacoustic models [12–16]. Due to the different approaches of the studies, the resulting propeller blade shape differs, thus underlining the importance of accurate numerical models. Gur et al. [12, 13] relied solely on a Blade Element Momentum (BEM) model to predict the propeller aerodynamics. Pagano et al. [14] used a BEM model in conjunction with a physics-based surrogate model. On the other hand, Marinus et al. [15] performed Reynolds Averaged Navier-Stokes simulations to build a metamodel, which was used in the optimization scheme. The optimized blade shapes in Pagano et al. [14] and Marinus et al.[15] showed an increase in blade sweep, either at the tip or along the radius of the blade, with respect to the benchmark blade. The optimized blades from Pagano et al. and Marinus et al. are shown in Figures 1.4 and 1.5, respectively. Blade A shown in Figure 1.4 is the benchmark blade, blade B is the design of minimum noise, and blade C is the design of maximum efficiency. Blades A to C in Figure 1.5 are the optimum blades with respect to a different design objective. Blade A achieves the highest efficiency for multiple advance ratios in take-off and cruise conditions, blade B has the lowest Sound Pressure Level (SPL) in the propeller plane at take-off and cruise conditions, blade C has the lowest SPL at various receiver locations, and blade D is the benchmark design.

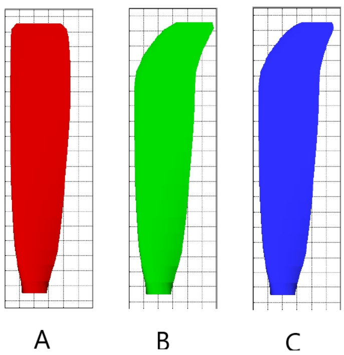

Figure 1.4: A: Benchmark blade. B: Design of minimum noise. C: Design of maximum efficiency. From Ref: [14]

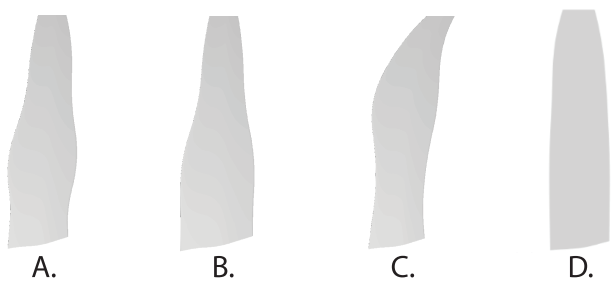

Figure 1.5: A-C: Optimized blades. D: benchmark blade. From Ref: [15]

From these studies, it is clear that blade sweep plays an important role in the trade-off between propeller efficiency and noise. However, the optimization studies do not provide a quantitative estimate of the effect of blade sweep on the trade-off between propeller efficiency and noise. Besides this gap in knowledge, as mentioned before, the choice of the numerical model to predict the aerodynamics and acoustics is of great importance. In the BEM studies, the effect of blade sweep is not present [12] or in the case of a more recent sensitivity study done by Burger [17] is not captured accurately enough. On the other hand, the study by Marinus et al. [18] highlights that selecting a numerical model of too high fidelity is undesirable due to the high computational cost and the high complexity that comes with implementing the model. Thus, this highlights the need for a study where the effect of sweep on the trade-off between propeller and efficiency is quantified, using a numerical model that is of lower fidelity than RANS, but is able to more accurately capture the effects of sweep than BEM models.

Research objective and questions

There is a lack of quantitative knowledge on the trade-off between propeller efficiency and noise and the need for a numerical model that can more accurately capture the effect of blade sweep compared to BEM models. In contrast to previous studies, this study will not perform an optimization, but will perform a sensitivity study between blade sweep and the trade-off between propeller efficiency and noise. This leads to the following research objective:

> *Quantify the trade-off between propeller efficiency and noise for an isolated, unducted propeller by means of a sensitivity study*

Two research questions are formulated to aid in achieving this research objective:

1. How does sweep affect the propeller aerodynamics and aeroacoustics for an isolated, unducted propeller?
2. How is the trade-off in propeller efficiency and noise due to sweep for an isolated, unducted propeller quantified?

It is important to note that only the propeller aerodynamics and aeroacoustics are considered in this thesis. Structural aspects are not considered.

Thesis outline

The report is divided into four parts, as shown in Figure 1.6. Part I covers the background theory on propeller aerodynamics and aeroacoustics including the principle of noise reduction due to sweep. Then, Part II discusses the methodology that was implemented in the research. First, the aerodynamic analysis method is discussed in Chapter 3. Second, the noise prediction method that was employed to study the propeller noise is discussed in Chapter 4. Thirdly, the parametrization method, geometry generation and discretization is discussed in Chapter 5. And fourthly the entire workflow of the tool used to perform the sensitivity analysis is covered in Chapter 6. Part III covers the sensitivity study. First, Chapter 7 discusses the study set-up. Then, Chapter 8 discusses the numerical results. Finally, the work is concluded in Part IV. In Chapter 9, the conclusions are presented, and recommendations for future work are given.

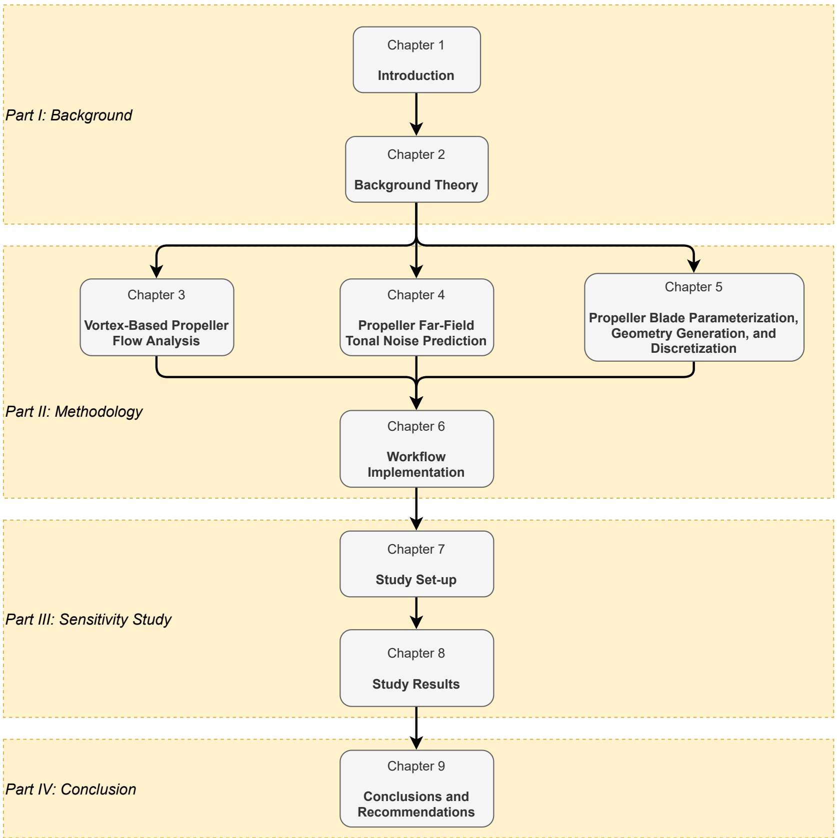

Figure 1.6: Report outline

2
Propeller Aerodynamics and Acoustics

This chapter gives an introduction to propeller aerodynamics and acoustics. First Section 2.1 discusses the propeller aerodynamics, then Section 2.2 discusses the propeller acoustics.

2.1. Propeller Aerodynamics

In this section, the theory on the prediction of propeller performance is discussed. First, Section 2.1.1 discusses the fundamentals, after which Section 2.1.2 explains the selection of the method that will be used to predict the propeller performance in the thesis.

2.1.1. Propeller Forces and Moments

The function of a propeller is to generate a force in the forward direction, known as thrust (T). This thrust is a result of the rotation of the blades, which are placed at an angle with respect to the rotation axis of the propeller. The rotation of the blades creates a pressure difference across the surface of the blades. This pressure difference results in a force perpendicular to the incoming flow, which is known as lift. Besides lift, the blades also experience a drag force, which acts parallel to the incoming flow direction. These two forces on a blade element are shown graphically in Figure 2.1. Since the blades are moving, they also experience a drag force, which acts parallel to the blade section. A schematic of the forces acting on a blade element can be seen in Figure 2.1. Alternatively, the forces on the blade can also be decomposed in a force component acting parallel to the rotation shaft, which is the thrust, and a force component acting along the direction of rotation, known as torque Q.

A propeller adds axial and angular momentum to the flow field. As a result of the thrust, the air in front of the propeller is sucked in front of it and accelerated downstream. This explains why the stream tube of air contracts as it passes through the blades, which can be seen in Figure 2.2. The axial velocity is increased behind the propeller, but also slightly in front of it. This increase of axial velocity, which is denoted by $w_a(r)$ depends on the loading of the propeller. Besides an increase in the axial velocity, the rotation of the propeller also causes an increase in tangential velocity, which is denoted by the term w_t in Figure 2.1. In Figure 2.1 it can be seen that the induced velocities alter the inflow angle ϕ of the blade element and this, in turn, will also determine the lift and drag force that the blade experiences.

In order to compare the performance between two propellers of different dimensions, it is typical to use dimensionless performance parameters. These parameters are obtained by non-dimensionalization of the desired parameter. For example, in the case of propeller thrust, the thrust coefficient is obtained by scaling the thrust with respect to fluid density ρ, the rotation speed n, and the propeller diameter D, which can be seen in eq. (2.1). Likewise, the same can be done for the propeller torque (Q) and power (P) which results in a torque coefficient c_Q and power coefficient c_P, which are given by Equation (2.2) and Equation (2.3).

$$c_T = \frac{T}{\rho n^2 D^4} \tag{2.1}$$

$$c_Q = \frac{Q}{\rho n^2 D^5} \tag{2.2}$$

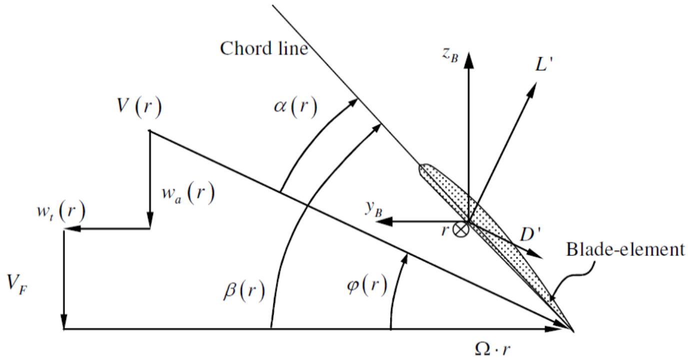

Figure 2.1: Velocities and forces of a blade element, Ref. [12]

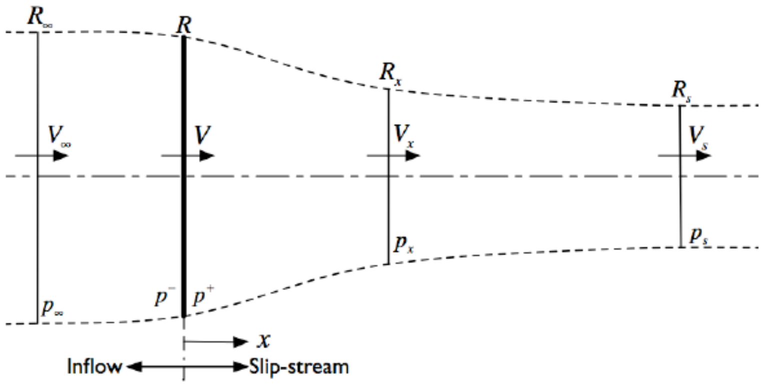

Figure 2.2: Schematic of a streamtube due to a propeller, Ref. [19]

$$c_P = \frac{P}{\rho n^3 D^5} \tag{2.3}$$

Besides the thrust and torque coefficient, an important dimensionless flow parameter is the advance ratio denoted by J. It relates the tip speed of the propeller to the freestream velocity, given by Equation (2.4):

$$J = \frac{V_\infty}{nD} \tag{2.4}$$

The propeller efficiency denoted by η is defined as the ratio of generated power due to thrust and to the input power from the propeller shaft, which can be rewritten as a ratio of the thrust coefficient, power coefficient, and the advance ratio as follows:

$$\eta = \frac{V_\infty T}{\Omega Q} = \frac{c_T}{c_P} J \tag{2.5}$$

2.1.2. Propeller Aerodynamic Performance Prediction Method Selection

The fluid dynamics around the propeller can be described with varying accuracy. It can be represented as a one-dimensional potential flow as is done in the actuator disk theory or as a fully developed turbulent three-dimensional flow as is the case in Computation Fluid Dynamics (CFD). Typically, the computational cost of the method scales with its accuracy; a calculation with the actuator disk theory can be done very quickly, while a simulation with CFD can take days. As was seen before in the introduction, most of the studies that were mentioned relied on the Blade Element Momentum theory (BEMT), which is a combination of the actuator disk theory (momentum theory) and blade element theory. This theory provides quick and relatively accurate results, which Gur and Rosen indicated in their paper[20]. However, BEM methods generally do not have a dependency to blade sweep. The studies by Miller, Pagano and Marinus have shown that this parameter plays an important role in the trade-off between efficiency and noise and therefore sweep should be included in the aerodynamic analysis. In a novel BEMT developed by Gur and Rosen, a radial induction factor was introduced, thereby accounting for the radial influence due to sweep [21]. This novel BEMT was implemented in a parallel study done by Burger [17]. In the paper however, the author mentions that the method was inaccurate for relatively large sweep angles, and a more expensive method should be used in future studies. This leaves either CFD or vortex-based methods. The use of CFD is undesirable as the computational cost will become very high. This leaves vortex-based methods for possible implementation. In contrast to BEM methods the computational effort is higher, but should be in the order of minutes [22], which is acceptable.

Selection of Vortex-Based Implementations

Several vortex-based implementations available either from open-source or commercially are the following:

- XROTOR, which is a fixed wake solver developed by Mark Drela from MIT [1]. It also includes two other formulations besides the vortex implementation: a graded momentum formulation and potential formulation.

- VAP3, a free wake rotary solver developed by Ryerson Applied Aerodynamics Laboratory of Flight (RAALF). [2]

- and FlightStream, a free wake solver from ResearchinFlight. [3]

Inspection of XROTOR and VAP3 revealed that specifying the sweep of the geometry in both XROTOR and VAP3 is not possible. Thus the input/output relation can not be assessed with these methods. Therefore FlightStream's vortex panel method was selected in this thesis. More information on the panel method can be found in Chapter 3.

2.2. Propeller Acoustics

Sound is a pressure wave that propagates through a medium, while noise is usually defined as sound that is undesired by the observer. The same pressure fluctuations that result in a forward force of the propeller, also causes noise. In this thesis, only the noise of isolated propellers is considered. Installed and interactions effects are not considered. First, the various noise sources of isolated propellers are discussed. Then, Section 2.2.2 explains how sweep affects the propeller noise. Finally, Section 2.2.3 discusses the available methods to predict the propeller noise.

2.2.1. Propeller Noise Sources

The noise of propellers can be divided into two categories: "Tonal" or "Harmonic" noise which occurs at specific frequencies and "Broadband" noise which occurs at multiple frequencies [23]. First, tonal noise is explained.

Tonal noise appears constant in time with respect to an observer on the rotating surface [23]. It is related to the Blade Passing Frequency (BPF) or fundamental frequency of the propeller, which is equal to the number of blades B times the rotational speed n (Bn). Typically, the pulse that is generated is not a pure sinusoid, but multiple harmonics exist [23]. These occur at integer multiples of the fundamental frequency. For example, the first harmonic is the fundamental frequency Bn, the second harmonic occurs at twice the the fundamental frequency $2Bn$, and so on. These harmonics are characterized by sharp peaks when the sound pressure level of the noise is plotted against the frequency of the source, as in Figure 2.3. Tonal noise can be further divided into three categories [23]:

- **Thickness noise** occurs from the displacement of the fluid by the passing blade. The amplitude of the noise is proportional to the blade volume, with frequency characteristics dependent on the shape of the blade cross section and the rotational speed [23]. This noise can be represented by a monopole source distribution and becomes important at high speeds [23].

[1] http://web.mit.edu/drela/Public/web/xrotor/, accessed 18-3-2021
[2] https://github.com/raalf/VAP3, accessed 18-3-2021
[3] https://researchinflight.com, accessed 18-3-2021

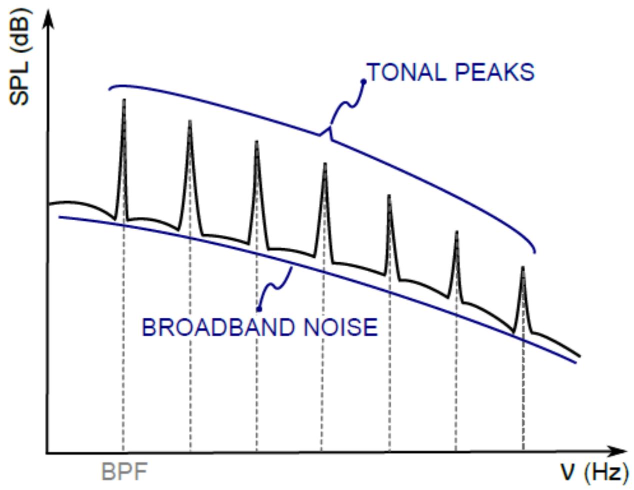

Figure 2.3: Typical envelope of propeller noise, from Ref. [18, p. 13]

- **Steady-loading noise** is caused by the pressure disturbances which are a result of the pressure fields associated with the loading on the propeller blades. This pressure disturbance moving in the medium propagates as noise. This is an important mechanism at low to moderate speeds [23].
- **Unsteady-loading noise** occurs when the blade loading is not constant over time. This can be caused by circumferential variations in inflow due to a nonzero incidence angle of the propeller axis with respect to the inflow or airframe installation effects. This noise source can lead to constructive and destructive interference with steady loading, thereby introducing a circumferential variation into the noise emissions [24].
- **Quadrupole noise** sources account for the possible transonic effects that are not covered by the thickness and steady-loading noise. This noise source is especially relevant for unswept blades operating at high tip Mach number [23, 24].

Broadband noise sources are considered as a secondary contribution to propeller noise. Full-scale tests with propellers have shown that broadband noise is relatively insignificant with respect to tonal noise [23]. Therefore broadband noise is neglected in this study. For completeness, the possible broadband noise sources for single propellers are discussed here:

- **Turbulence-ingestion noise** is caused by the interaction of inflow turbulence with the blade leading-edges. Due to the inflow being turbulent, the resulting noise is random in nature. The importance of this noise source depends on the magnitude of the inflow turbulence. It becomes significant in conditions of high turbulence and at low speeds [23, 24].
- **Trailing-edge noise** is generated near the trailing edge of the blades due to diffusion of the turbulent boundary layer [23, 24].

2.2.2. Propeller Noise Prediction Method Selection

Any of the propeller noise prediction methods that currently exist are derived from the Ffowes-Williams and Hawkings equation [23]. It is a fundamental equation of sound generation and is attractive since it combines the equations of momentum, continuity and state into a wave equation, which can be solved to varying degree of precision by a variety of analytical methods. A review of linear noise prediction methods was done by Magliozzi [23] and will be briefly summarized here.

The linear form of the Ffowes Williams and Hawkings equation is given by:

$$\nabla^2 p - \frac{1}{c^2}\frac{\partial^2 p}{\partial t^2} = -\frac{\partial}{\partial t}\left[\rho_o v_n |\nabla f| \delta(f)\right] + \frac{\partial}{\partial x_i}\left[l_i |\nabla f| \delta(f)\right] \tag{2.6}$$

Where the left side is the linear wave operator acting on the acoustic pressure p. The right side contains the source terms resulting from the motion of surfaces in the fluid: ρ_o is the ambient density, c is the ambient speed of sound, v_n is the local velocity of the surface normal to itself, $\delta(f)$ is the Dirac delta function, x_i is the observer position, and l_i is the ith component of the surface force. The first source term represents volume displacement of the blades and produces thickness noise. The second term represents the action of the blade forces on the air and produces loading noise. Equation (2.6) can be solved to find the acoustic waveform p as a function of time. Methods based on this approach are known as time-domain methods. The acoustic waveform p however can also be Fourier transformed to give the acoustic waveform as a harmonic. These methods are known as frequency-domain methods.

Time-domain methods

Time-domain methods solve Equation (2.6) directly in terms of the space-time variables. The advantage of these methods are that they can treat the blade geometry to any desired level of precision. Solving the equations results in the acoustic pressure waveform $p(t)$. The methods formulated by Farassat are the most prominent in literature. Farassat has published his works since 1975 [18]. He solves Equation (2.6) with the use of a convolution of free-space Green's functions and a source distribution [18] so that:

$$4\pi p'(\mathrm{x},t) = \frac{\partial^2}{\partial x_i \partial x_j}\int_V \left[\frac{T_{ij}}{r|1-M_r|}\right]_{\tau_e} dy - \frac{\partial}{\partial x_i}\int_{f=0}\left[\frac{l_i}{r|1-M_r|}\right]_{\tau_e} dS + \frac{\partial}{\partial t}\int_{f=0}\left[\frac{\rho_\infty v_n}{r|1-M_r|}\right]_{\tau_e} dS \quad (2.7)$$

where the quadrupole source terms contribution is integrated over a finite volume $\mathcal{V}$ surrounding the blade, whereas the monopole and dipole terms are integrated over the blade surface $f = 0$. The free-space Green's function introduces a Doppler factor depending on M_r the relative section Mach number of the blade surface, projected in the radiation direction $\mathbf{r} = \mathrm{x} - \mathrm{y}$ between the observer in x and the source in y. This Mach number depends purely on the kinematics of the helical movement of the blade. The integrands are evaluated at the retarded time τ_e. This is the time when the sound received by an observer in position x at time t was actually emitted by the source in position y. It is computed by solving the following equation:

$$g(\mathrm{x},\mathrm{y},\mathrm{t}) = \tau - t + r/c = 0 \quad (2.8)$$

Where r is the distance between the observer and the source, t is the time and τ is the Farassat's work is based on generalized functions and their generalized derivatives [18]. The derivation of all solutions is beyond the scope of this review. For those interested in Farassat's time-domain formulations, the reader is referred to a summary in Marinus' thesis [18] starting on page 83.

Frequency-domain methods

Frequency domain methods eliminate time from the wave equation by means of Fourier transformation of the waveform $p(t)$[23]. Due to the transformation there is no need to compute retarded blade locations or numerical derivatives. Usually some precision in the representation of the blade geometry is lost through this transformation, but in general this loss is acceptable for harmonics to a fairly high order [23]. The Fourier transformation gives rise to Bessel functions which indicate the radiation efficiency. The harmonics are computed one at a time, and a waveform is generated by means of summing a Fourier series. By representing the blades as helicoidal surfaces, far-field noise formulas can be easily coded on a personal computer [23]. These formulas give direct insight into the influence of the blade geometry and operating conditions on the sound harmonics. The first successful propeller noise theory by Gutin was in harmonic form [23]. This theory was extended by many investigators; one of which was Hanson, whose versions include effects of thickness, forward flight, and blade sweep [23].

Since time-domain methods require accurate time computations, they are an additional computational burden. Therefore frequency-domain methods are preferred over time-domain methods. The frequency formulas by Hanson are based on the thin-blade assumption, which can not be used for blades with relatively thick sections. However this will not pose a problem for this thesis. The frequency domain method formulation is covered in detail in Chapter 4.

2.2.3. Propeller Noise Reduction due to Sweep

Since sweep is the blade parameter of interest in this study, a brief explanation is given on the conceptual mechanism of noise reduction due to blade sweep. As Hanson [25] states in his paper, there are two beneficial effects of sweep. The first is the relief of transonic compressibility effects in the same way as for swept wings. This reduces the strength of the quadrupole sources as they are primarily transonic flow phenomena [25]. The second effect of sweep is that it changes the phase of the noise signals from different portions of the blade [25]. This is illustrated in Figure 2.4 where one harmonic of the noise is considered. Since only one harmonic at a time is considered, the noise of each section on the blade is only dependent on its amplitude A_j and its phase ϕ_j. By summing the contributions of each section, the total noise is determined. This is illustrated in the top of the figure by the vector addition and mathematically by Equation (2.9). Figure 2.4 illustrates that by summing contributions with varying phases causes phase interference, which can have a positive effect on the total noise of the blade.

$$A_R e^{i\phi_R} = \sum_{j=1}^{N} A_j e^{i\phi_j} \tag{2.9}$$

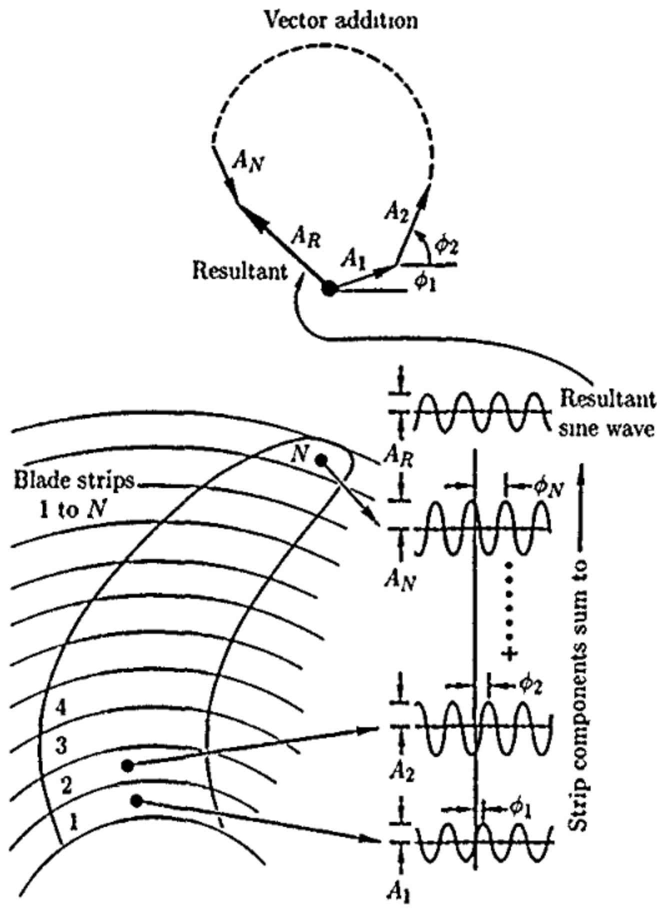

Figure 2.4: Conceptual benefit of blade sweep for reducing noise, from Ref: [25]

II

Methodology

3

Vortex-based Propeller Flow Analysis

This chapter discusses the FlightStream vortex panel method, which is used to analyze the isolated propeller performance in this thesis. First, Section 3.1 covers background theory of panel methods. Then, Section 3.2 explains the characteristics of FlightStream. Lastly, Section 3.3 discusses a validation study of FlightStream with experimental data.

3.1. Panel Methods

Panel methods are numerical schemes that solve the velocity potential equation for linear, inviscid, irrotational flow for subsonic or supersonic Mach numbers[26]. For three-dimensional, steady, subsonic flow this equation is written as:

$$\nabla^2\phi = \left(1 - M_\infty^2\right)\phi_{xx} + \phi_{yy} + \phi_{zz} = 0 \tag{3.1}$$

Where M_∞ is the free stream Mach number and ϕ is the perturbation velocity potential [26].

Typically, panel methods discretize the geometry with rectangles or quadrilaterals and then apply a singularity distribution on each panel. Three types of singularities can be applied: sources, doublets, and vortex singularities [27]. A distinction exists between lifting and non-lifting bodies. Since lifting bodies involve circulation, singularities that can represent circulating flows must be used, such as doublets or vortices. Non-lifting bodies can be approximated with source panels, as these do not represent circulation [28]. An example of a three-dimensional non-lifting body represented by source panels is shown in Figure 3.1.

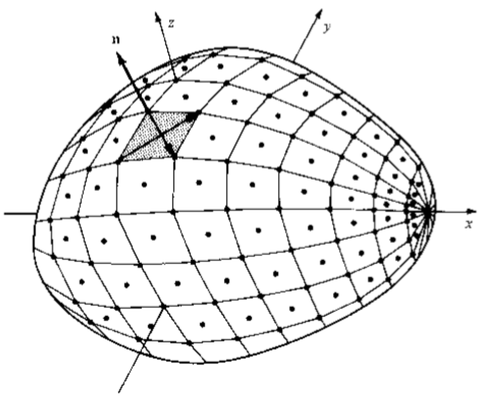

Figure 3.1: Representation of a non-lifting bodies using source panels, Ref: [28]

Since Equation (3.1) remains the same for each geometry, additional boundary conditions are needed to obtain a unique solution. One important boundary condition is the flow tangency condition which is imposed on the geometry. This condition states that the flow must be tangent to the panel surface, which translates into the condition that the velocity component normal to the panels is zero [28].

For cases where lifting bodies are predicted, applying only this condition will not result in a unique solution. Thus, a wake model is needed to find a unique solution for lifting bodies in subsonic flows, specifying the wake strength at the trailing edge, as well as the shape and location where the wake is shed [27]. The wake strength problem is often quickly solved by applying the Kutta condition to the trailing edge along the wing, as shown in Figure 3.2. Then the strength of the wake panels is obtained by computing the difference in wake strength between the upper and lower sides of the panels at the trailing edge. The problem of defining the wake shape and location is typically more difficult to solve, especially for three dimensions. Depending on the shape of the trailing edge, boundary conditions can be applied to determine the wake shedding location [27], as shown in Figure 3.3. In terms of the wake shape, this can be defined a priori or computed by the wake model.

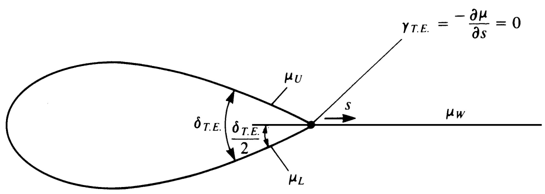

Figure 3.2: Implementation of the Kutta condition for a surface doublet distribution, Ref: [27]

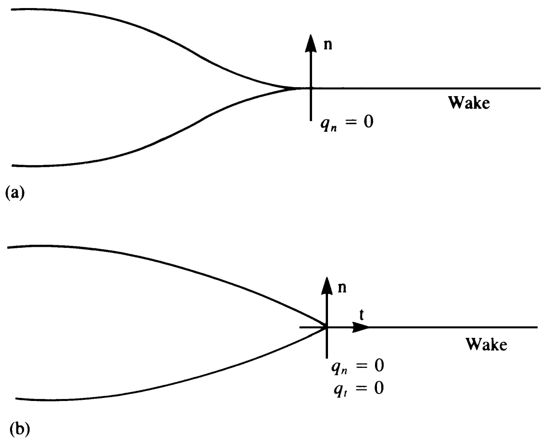

Figure 3.3: Conditions applied for for (a) a cusp trailing edge and (b) a finite trailing edge, Ref [27]

Panel methods that solve the perturbation velocity potential, as in Equation (3.1), do not take into account the effects from viscosity or compressibility. However, panel methods try to account for viscosity by including boundary-layer models or using compressibility corrections[27]. One example of a compressibility correction is the Prandtl-Glauert rule [26].

Similarly, by adding a boundary layer model, panel codes try to account for viscosity effects [27]. The boundary layer model uses the pressure distribution from the panel-code solution and then computes the displacement thickness [26]. When the geometry is a wing, the displacement thickness is added to the wing in either of the following two approaches [26]:

1. the wing shape is updated by adding the displacement thickness to the initial shape or
2. the source strengths of the wing panels are adjusted such that the resultant flow field is approximately displaced by the displacement thickness that was computed before.

For either approach, the resultant change in shape has two effects: it reduces the effective camber of the wing and increases the wing thickness. The primary effect of these changes is a reduced lift due to the reduced effective camber. The second, usually less important effect is a slight increase in lift due to the increased thickness [26].

3.2. FlightStream Surface Vorticity Solver

First Section 3.2.1 briefly provides background theory on FlightStream. Then, Section 3.2.2 shortly discusses the different solver modes and settings of FlightStream.

3.2.1. Background

FlightStream is a panel method developed by Research in Flight [1]. It uses triangles to represent geometries. However, the solver can also handle quadrilaterals and then converts these into triangles.

[1] https://researchinflight.com/; Accessed on 18-1-2021

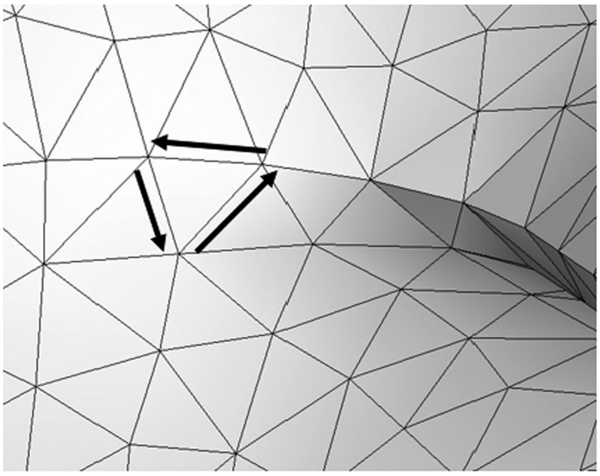

Figure 3.4: A mapped vortex ring of a mesh face, Ref: [29]

Distinctive of this panel method is the use of unstructured meshes to discretize the geometry. This provides two benefits compared to structured meshes [29]. Firstly, they require fewer facets since they do not have to be forced to become a triangle. Secondly, in contrast to quadrilaterals, triangles do not have to be 'sanitized' to establish the effective surface normal direction [29]. Each of the edges of the triangle represents the segment of a vortex ring in three-dimensional space, as shown in Figure 3.4. The velocity induced by a linear segment of a face at an arbitrary point P is then obtained according to the Biot-Savart law [29], given by:

$$\mathrm{d}V_i = \frac{\Gamma}{4\pi}\frac{\mathrm{d}\vec{l}\times\vec{r}}{r^3} \tag{3.2}$$

In FlightStream, the arbitrarily oriented vorticity is converted into directed circulation distributions through the method of integrated circulation. This method works by evaluating the vorticity along a series of two-dimensional cross-sections that enclose the entire geometry, as shown in Figure 3.5 (a). First, the induced velocity of the vortex rings of the faces is evaluated at the perimeter of a rectangular cross-section. By adding all the contributions, the induced velocity from all the surface vortex rings at the vertices of the cross-section can be evaluated. Then, the net integrated circulation of that cross-section is evaluated using Stokes' theorem [29], given by :

$$\Gamma_k = \int_0^L V_{\mathrm{induced},l}\cdot \mathrm{d}l \tag{3.3}$$

If the cross-section planes are aligned orthogonal to the free stream and lift vectors, their alignment is identical to a lifting-line distribution of integrated circulation along a rectangular wing [29]. Thus, the integrated vorticity of each cross-section becomes identical to the "bound" vorticity from Prandtl's lifting-line theory. This is shown in Figure 3.5 (b). Thus, after obtaining the net integrated circulations of each cross-section, the forces and moments can be evaluated using Prandtl's Lifting-Line formulation, and Kutta-Joukowsky's theorem of circulation [29].

3.2.2. Solver Modes and Settings

FlightStream contains four different solver types:

- Steady
- Steady Rotary
- Steady Viscous
- Unsteady

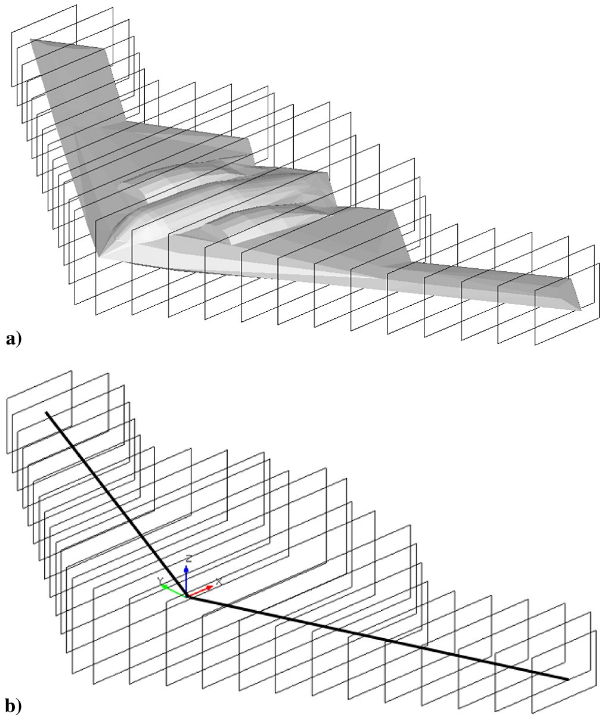

Figure 3.5: Representations of (a) integrated circulation cross-sections on a sample geometry and (b) equivalent Prandtl lifting line, Ref: [29]

The steady solver is the default solver type. This option should be chosen to model non-rotating flows, such as when analyzing the forces and moments of an aircraft in steady flow. The steady rotary solver should be used for the analysis of rotors, propellers, and turbines in steady flow. In this mode, the free stream is rotated about the X-axis of a reference coordinate system according to a user-defined rotation rate (in revolutions per minute). This solver type assumes the flow to be axis-symmetric about the X-axis of the reference coordinate system. Besides these two, there is a viscous variation of the steady solver, and an unsteady type, which can simulate non-axis-symmetric geometries. Since it is assumed in this thesis that the flow is axis-symmetric, the steady rotary solver is selected to analyze the propeller flow.

Besides the solver types, FlightStream can be operated in two analysis modes: the vorticity mode or the pressure mode. In the vorticity mode, the forces and moments are purely inviscid. On the other hand, the pressure mode uses the surface pressure fields from the vorticity mode and applies a boundary layer model to predict skin-friction drag and flow separation. Both modes are used to compute the efficiency and noise of a design. In Section 3.2.3 it is explained which of these modes are used to derive the propeller efficiency and noise in this thesis.

The boundary layer module of FlightStream is based on the Panel Method Ames Research Center (PMARC) panel code developed by NASA [30]. It is a two-dimensional integral boundary layer method, which is applied along surface streamlines. The boundary layer method consists of a laminar boundary layer analysis, a transition and separation analysis, and a turbulent boundary layer analysis:

- The laminar boundary layer analysis is a two-parameter extension of Thwaites method developed by Curle [31].
- The transition/laminar separation analysis is based on empirical relationships from a wide variety of sources. A check is performed at each point as the boundary layer is computed, to determine if the boundary layer continues to the next point, undergoes natural transition, separates and reattaches as a turbulent boundary layer, or separates with no reattachment.
- The turbulent boundary layer analysis is based on the Nash-Hicks model [32].

For more information on these different boundary layer analysis methods, the reader is referred to the paper by Ashby et al. [30]. The next subsection explains how the forces and moments are evaluated in FlightStream.

3.2.3. Evaluation of the Propeller Forces and Moments

FlightStream can provide the loads and moments per mesh element, component, or a global value. This can be retrieved from inside the Analysis Simulation Tab, which is shown in Figure 3.6.

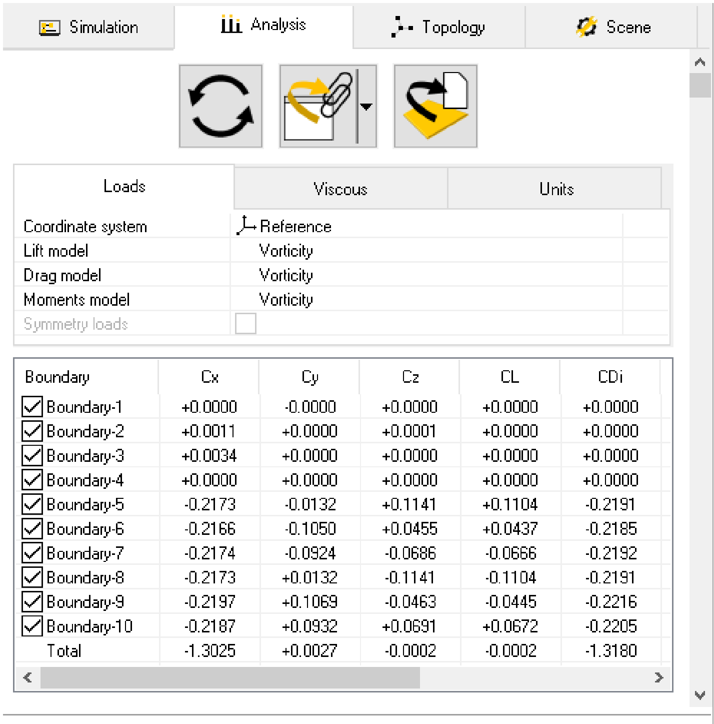

Boundary	Cx	Cy	Cz	CL	CDi
Boundary-1	+0.0000	-0.0000	+0.0000	+0.0000	+0.0000
Boundary-2	+0.0011	+0.0000	+0.0001	+0.0000	+0.0000
Boundary-3	+0.0034	+0.0000	+0.0000	+0.0000	+0.0000
Boundary-4	+0.0000	+0.0000	+0.0000	+0.0000	+0.0000
Boundary-5	-0.2173	-0.0132	+0.1141	+0.1104	-0.2191
Boundary-6	-0.2166	-0.1050	+0.0455	+0.0437	-0.2185
Boundary-7	-0.2174	-0.0924	-0.0686	-0.0666	-0.2192
Boundary-8	-0.2173	+0.0132	-0.1141	-0.1104	-0.2191
Boundary-9	-0.2197	+0.1069	-0.0463	-0.0445	-0.2216
Boundary-10	-0.2187	+0.0932	+0.0691	+0.0672	-0.2205
Total	-1.3025	+0.0027	-0.0002	-0.0002	-1.3180

Figure 3.6: View of the Analysis Simulation Tab in the graphical user interface of FlightStream

Inside this tab, the following force and moment information can be retrieved [33]:

- Force vector coefficients in the X, Y, and Z directions, evaluated in the specified coordinate system,
- Lift coefficients, induced drag coefficients, and skin-friction coefficients, evaluated in the specified coordinate system,
- Moment coefficients about the X, Y, and Z axes, evaluated in the specified coordinate system,
- and local Reynolds numbers for each component of the geometry.

Two different data sources are obtained from this tab:

1. A spreadsheet results file, similar to the table as shown in Figure 3.6, which provides force and moment coefficients of a desired geometry component in FlightStream.
2. and a force export file, which provides force coefficients of each mesh face in the X, Y, and Z direction of a desired geometry component

The former one is needed to compute the propeller efficiency, while the latter one is required to obtain the radial blade loading distributions. The spreadsheet results file is generated using the vorticity mode in FlightStream. This means that the forces computed for the efficiency are purely inviscid. However, the force coefficients that are obtained from the force export file are computed using the pressure mode in FlightStream. Figure 3.7 shows how the two modes are used to compute the propeller efficiency and noise, respectively. In the next section, it is explained how the propeller efficiency is determined using the vorticity mode.

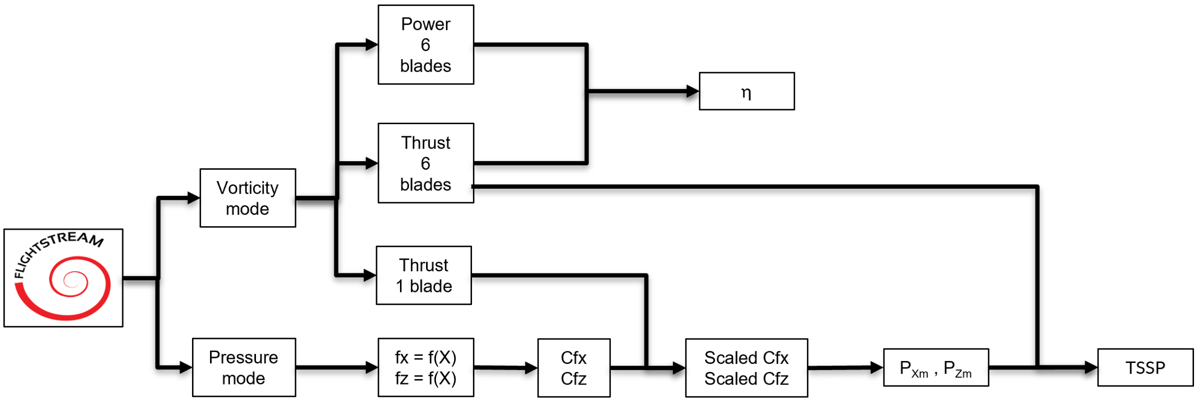

Figure 3.7: Flowchart showing which modes are used in FlightStream to compute the efficiency and noise of the propeller

3.2.4. Determination of the Propeller Efficiency

The propeller efficiency η is determined from two quantities from the vorticity mode in FlightStream:

- C_x
- C_{M_x}

These are defined as follows:

$$C_x = \frac{\texttt{Force in X-direction in the specified coordinate system}}{q \cdot S_{ref}} \tag{3.4}$$

$$C_{M_x} = \frac{\texttt{Moment about the X-direction of the specified coordinate system}}{q \cdot S_{ref} \cdot L_{ref}} \tag{3.5}$$

Here q is the dynamic pressure defined with respect to the reference quantities: $\frac{1}{2}\rho V_{ref}^2$. V_{ref}, L_{ref}, and S_{ref} are an arbitrarily defined reference velocity, length, and area used by FlightStream to non-dimensionalize the forces and moments. As shown in Figure 3.6, C_x and C_{M_x} can be obtained per boundary, such that the contributions due to the blades, hub, or nacelle can be isolated. For the computation of the propeller efficiency in this thesis, only the C_x and C_{M_x} contributions from the six blades of the propeller are used, such that the propeller efficiency is represented by the propeller blades. First, the thrust and power of the propeller are obtained by multiplying the C_x and C_{M_x} with the reference parameters as follows:

$$T = \frac{1}{2} C_x \rho_\infty S_{ref} V_{ref}^2 \tag{3.6}$$

$$P = \frac{1}{2} C_{M_x} \rho_\infty L_{ref} S_{ref} V_{ref}^2 \Omega \tag{3.7}$$

where Ω is the rotation speed of the propeller in rad/s. Then, Equations (2.1) and (2.3) are used to compute the thrust and power coefficient of the propeller. These are then combined in Equation (2.5) together with the advance ratio to determine the propeller efficiency. The propeller torque Q is obtained indirectly from the propeller power with Equation (3.8):

$$P = Q\Omega \tag{3.8}$$

In the next subsection, it is explained how the radial blade loading distributions predicted by the pressure mode are scaled.

3.2.5. Scaling of the Radial Blade Loading Distributions

During the implementation, discrepancies were seen between the blade thrust and torque obtained from the vorticity mode and the blade thrust and torque predicted by the pressure mode. As an example, the results of the Pareto designs from the sensitivity study are discussed here. The planforms in the XY plane of the four blades are shown in Figures 3.8a to 3.8d, while the operating settings and

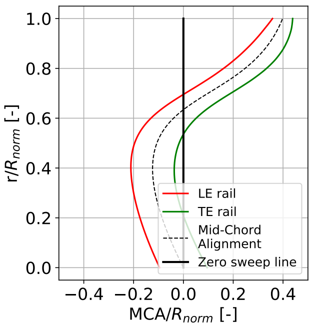

(a) Swept blade design 1 before twist and pitch is applied

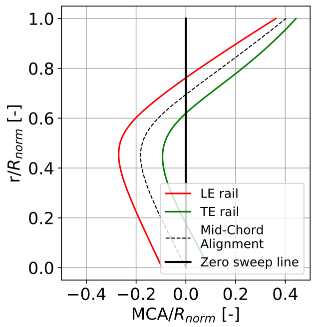

(b) Swept blade design 2 before twist and pitch is applied

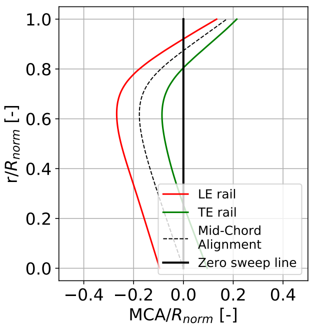

(c) Swept blade design 3 before twist and pitch is applied

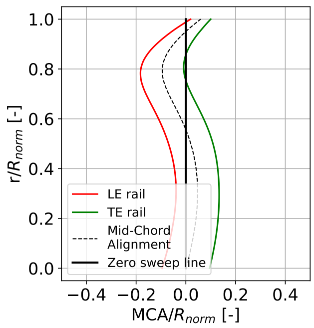

(d) Swept blade design 4 before twist and pitch is applied

Figure 3.8: Examples of the Pareto front swept designs taken from the sensitivity study, discussed in Chapter 8

Table 3.1: Operating conditions and geometric parameters used to compare the modes

Parameter	Value	Unit
Number of blades	6	-
Fluid Density	1.225	[kg m^{-3}]
Freestream velocity	60	[ms^{-1}]
Reference velocity	60	[ms^{-1}]
Reference area	0.0875	[m^2]
Pitch angle	47.14	[deg]
Advance ratio	2.23	[-]

conditions used to obtain the results are listed in Table 3.1. In Table 3.2 the C_x values for 1 blade from the vorticity mode (spreadsheet results file) and the pressure mode (force export file) are shown respectively. C_x is normalized as described in Equation (3.4). It can be seen that there is a factor of 100 to 1000 difference between the thrust of the vorticity mode and the pressure mode. Similar differences

Table 3.2: Comparison of C_x predicted by Spreadsheet results (Vorticity Mode) and Force export file (Pressure mode)

Design number	C_x 1 blade pressure mode [-]	C_x 1 blade vorticity mode [-]	Ratio VM / PM Cx
1	8.345E-06	1.187E-02	1422.0
2	1.079E-05	1.427E-02	1322.8
3	1.664E-05	1.210E-02	727.0
4	1.774E-05	1.150E-02	648.1

between the modes are also seen for the prediction of torque.

Due to the discrepancy that is seen between the modes, the radial blade loading distributions that are obtained from the pressure mode are scaled using the ratio of the blade thrust between the two modes: $\frac{T_{1B}^{VM}}{T_{1B}^{PM}}$. The force coefficient in axial direction at radial section z is scaled as follows:

$$c_{f_x}^{VM}(z) = \frac{c_{f_x}(z)^{PM}}{T_{1B}^{PM}} T_{1B}^{VM} \tag{3.9}$$

$c_{f_x}^{PM}$ is the radial loading distribution obtained from the Pressure Mode (PM). An example loading distribution can be seen in Figure 6.6. T_{1B}^{VM} is the thrust of 1 blade obtained from Vorticity Mode (VM), which was discussed in Section 3.2.3, while T_{1B}^{PM} is obtained by integrating the loading distribution $c_{f_x}^{PM}$ in the radial direction and then multiplying with the reference quantities as shown in the following equation:

$$T_{1B}^{PM} = \int_{z_h}^{1} c_{f_x}^{PM} \, \mathrm{d}z \cdot \frac{1}{2} \rho V_{ref}^2 S_{ref} \tag{3.10}$$

Finally, when the loading distributions are scaled, the coefficients that are used to predict the noise can be obtained. For more information on how the coefficients are derived which are given into the noise prediction method, the reader is referred to Section 6.3.

3.3. Solver Validation

A validation study was performed to validate the aerodynamic forces and moments predicted by FlightStream. The reference case used in the study is the N250 or ”XPROP” propeller geometry. The propeller has six blades, and the diameter is 0.4064 m. A picture of the geometry is shown in Figure 3.9.

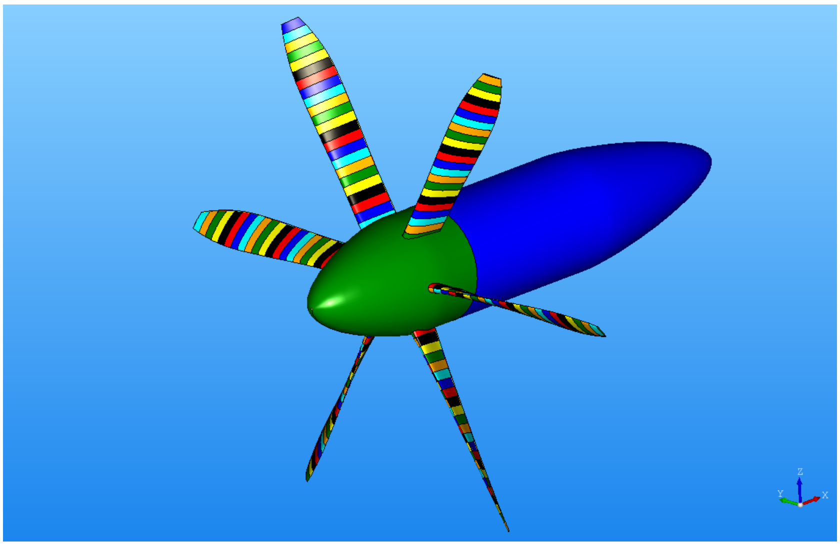

Figure 3.9: XPROP propeller topology shown inside the Multi-Model Generator

The experimental data that have been used for validation are obtained from the study by Li et al. [34]. The advance ratio is varied by changing the rotational speed, while the free stream velocity is kept constant. The flow velocity was set to 30 m/s, while the pitch angle at 70% radius was fixed to 30 degrees. The fluid properties and reference quantities (S_{ref},L_{ref},V_{ref}) that were used in the study are listed in Table 3.3. The FlightStream settings that were used are listed in Table 3.4.

A mesh convergence study was done with the XPROP before the results were gathered. For more information, the reader is referred to Section 5.5.

Results

Figure 3.10 shows the thrust coefficient versus the advance ratio. It can be seen that there are discrepancies between FlightStream and experimental data. The thrust is underestimated at a low advance ratio and overestimated at a high advance ratio with respect to the experimental data. The largest discrepancy is found at an advance ratio of 0.6, where the error is approximately 17 %. The smallest

Table 3.3: Fluid properties in the validation study

Variable	Value	Units
Free stream velocity	30	m/s
Air density	1.225	kg/m^3
Static pressure	101325	Pa
Static temperature	288.15	K
Reference velocity	30	m/s
Reference length	0.0311	m
Reference area	0.08725	m^2

Table 3.4: FlightStream settings

Variable	Value
Version	2020.1
Build	4192020
Lift model	Vorticity
Drag model	Vorticity
Moments model	Vorticity
Flow separation	Disabled
Viscous drag model	Reynolds-Averaged [2]
Boundary layer type	Turbulent [2]
Solver mode	Steady Rotary
Freestream type	Rotating

[2] These settings are not used when the lift, drag and moment models are set to ”Vorticity”

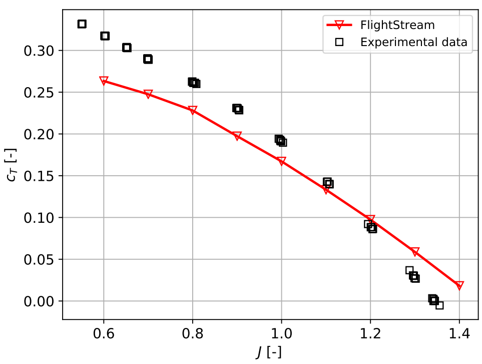

Figure 3.10: Thrust coefficient comparison of FlightStream with experimental data from [34]

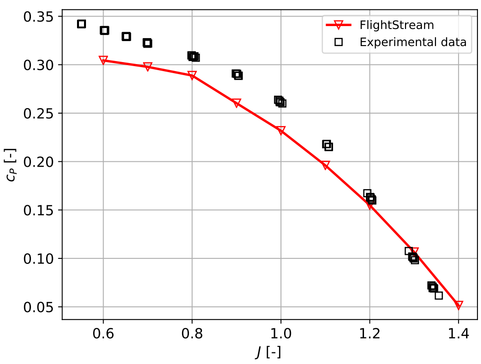

Figure 3.11: Power coefficient comparison of FlightStream with experimental data from [34]

error is obtained approximately at an advance ratio of 1.2. The further the advance ratio is increased beyond 1.2, the larger the error with respect to experimental data becomes.

The discrepancy of the thrust at a low advance ratio is partially explained by a change in the airfoil shapes. During the setup of the geometry, it was found that the original airfoil shapes were altered inside the geometry generation tool, the Multi-Model Generator (MMG). For more information on the topology generation process, see Section 5.3. The original airfoil shapes feature finite edges because of manufacturing limits. However, MMG fits a new airfoil shape such that the trailing edge of the profile becomes sharp. This is shown in Figures 3.14 and 3.15. The profiles that were used in the experiment are indicated by the solid line, while the profiles that were altered by MMG are indicated by the dashed line. It can be seen that the thickness of the fitted airfoil is slightly less than the original airfoil.

An analysis is performed to check how the change in the cross-sectional shape affects the 2D viscous lift and drag forces on the blade. The XPROP airfoils at 0.475 R_{tip} and 0.755 R_{tip} of the blade

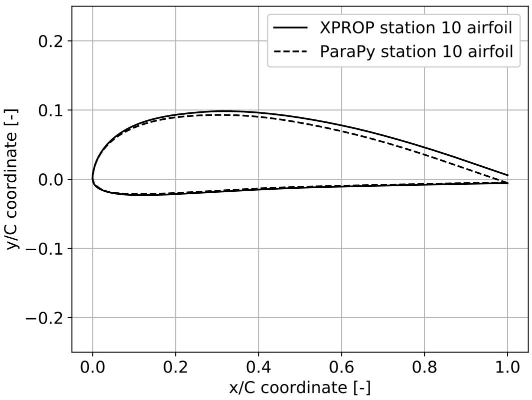

Figure 3.12: Comparison of the station 10 airfoil from the XPROP at 47.5% R_{tip} with the modified airfoil in Parapy

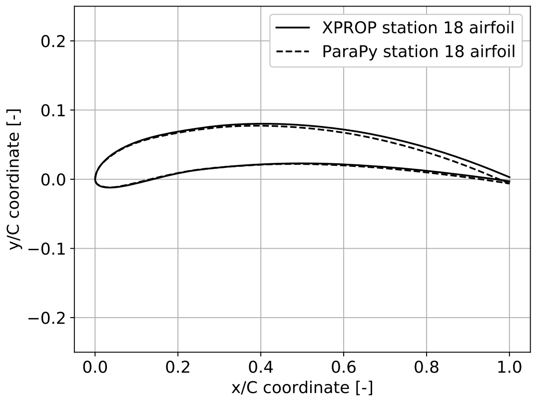

Figure 3.13: Comparison of the station 18 airfoil from the XPROP at 75.5% R_{tip} with the modified airfoil in Parapy

are analyzed with XFOIL [3] at -20 to 20 degrees angle of attack. The Reynolds number was set to 150,000, and the critical amplification factor N_{crit} [4] is set to 0.1, corresponding to an early transition of the boundary layer. Figures 3.14 and 3.15 show a comparison of the lift curve slopes of the original and modified airfoils. It can be seen that the maximum lift coefficient is decreased from approximately 1.4 to 1.25 in Figure 3.14. This is especially at a high angle of attack, which corresponds with a low advance ratio. The offset in lift is roughly 10 %. However, the maximum offset in thrust at a low advance ratio is roughly 17 %. Hence, the offset in thrust at a low advance ratio is not fully explained by the difference in the cross-sectional shape.

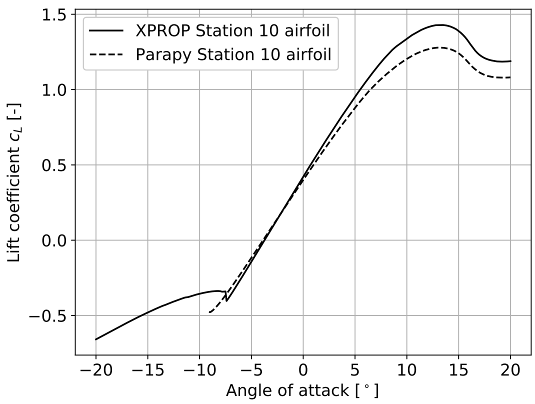

Figure 3.14: Lift polars of the station 10 airfoil from the XPROP and the modified airfoil by ParaPy

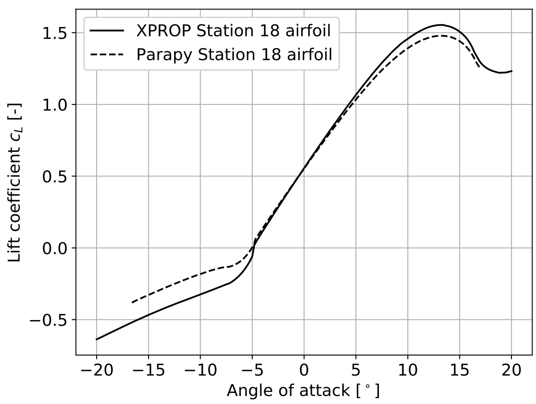

Figure 3.15: Lift polars of the station 18 airfoil from the XPROP and the modified airfoil by ParaPy

Figure 3.11 shows that the agreement between FlightStream and experimental data is better for the power coefficient with respect to the thrust. The largest error between the two is roughly 10 % and can be found at an advance ratio of 0.6. The smallest error for c_P is obtained at an advance ratio of approximately 1.2. The larger the advance ratio is increased beyond 1.2, the more the c_P from FlightStream deviates from experimental data.

Lastly, the discrepancies in Figures 3.10 and 3.11 result in expected discrepancies in the efficiency, shown in Figure 3.16. At an advance ratio lower than 1.0, FlightStream and experimental data show reasonable agreement in the slope of the curve. However, at a higher advance ratio, the discrepancy becomes larger. FlightStream overestimates both the efficiency and the advance ratio at which the maximum efficiency is obtained. FlightStream predicts a maximum efficiency of approximately 0.75 at an advance ratio of 1.2, whereas the experimental data shows a maximum efficiency of about 0.73 at an advance ratio of 1.0.

[3] https://web.mit.edu/drela/Public/web/xfoil/, accessed on 6-8-2021

[4] N_{crit} is the log of the amplification factor of the most-amplified frequency, which triggers transition via linear instability of the 2D Tollmien-Schlichting waves [35].

The discrepancy in the propeller efficiency at a high advance ratio is likely related to the Reynolds number at which the experiment was performed. As Sinnige points out in his thesis, the propeller performance is sensitive to the Reynolds number, especially in the case of small models at relatively low freestream velocities [24]. For this propeller model, the XPROP, the performance is especially sensitive to the Reynolds number for $Re_c^{0.7R} < 1,5 \cdot 10^5$ [24]. In Figure 3.16 together with the efficiency, the Reynolds number as a function of the advance ratio is shown. It can be seen that from an advance ratio of approximately 1.0, the Reynolds number is below the critical value mentioned earlier. In an attempt to reduce the discrepancy due to a low Reynolds number, the freestream velocity is increased in the sensitivity study from 30 m/s to 60 m/s with respect to the experimental data.

Although FlightStream does not show perfect agreement with experimental data, the results presented in this section are deemed acceptable for the purposes of this research. By increasing the free stream velocity, the Reynolds number is increased, and therefore the error with respect to experimental data is expected to decrease. Since this study only focuses on a relative comparison between different blade shapes and the operating conditions are kept constant, the study can be carried out with the proposed analysis method.

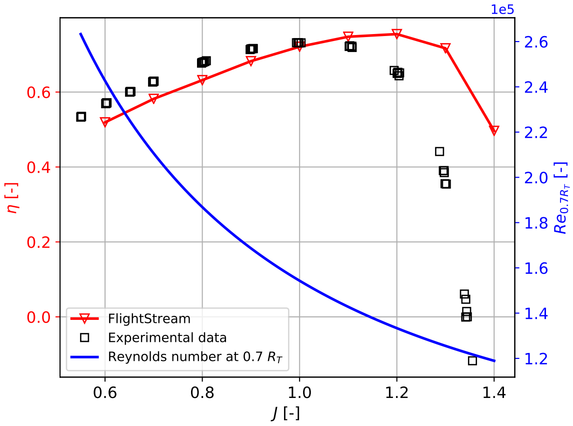

Figure 3.16: Left axis: Comparison of propeller efficiency of FlightStream and experimental data from [34]. Right axis: Reynolds number at 70 % R_{tip}

4

Propeller Noise Prediction

This chapter discusses the propeller noise prediction method used in this thesis. The far-field tonal noise frequency formulation by Hanson [36] is selected. This formulation is preferred as discrete tones can be computed separately, and no retarded blade computations are needed. The helicoidal surface theory that is formulated by Hanson [25] has been validated by Parry [37]. The implementation of the formulation is discussed next.

4.1. Far-Field Tonal Noise Formulation

Hanson's frequency domain formulation accounts for the effects of forward flight, as well as noncompactness, i.e., noise cancellation due to finite thickness and chord [36]. Blade sweep and offset (bending due normal to the chord) appear explicitly as phase lag effects. In the formulation, it is assumed that the propeller is propagating with a constant speed forward in flight, and the inflow is uniform, such that all sources are steady in blade-fixed coordinates. Furthermore, the thin-wing approximation is used, which permits satisfying the surface boundary equations on a mean surface rather than on the blade's upper and lower surfaces. For convenience, a local space-fixed helicoidal coordinate system is defined, shown in Figure 4.1, where 'PCA' is the Pitch Change Axis.

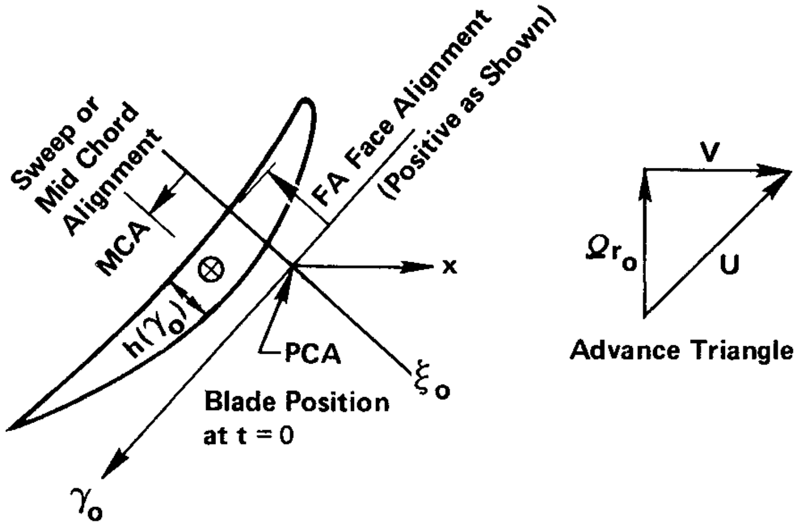

Figure 4.1: Helicoidal local blade-fixed coordinates γ_0 and ξ_0, from Ref. [36, p.2]

The mathematical basis of the theory is the linear wave equation for pressure disturbance, which is given by Equation (4.1) [38]:

$$\nabla^2 p - \frac{1}{c_0^2}\frac{\partial^2 p}{\partial t^2} = -S(\underline{r}, t) \tag{4.1}$$

where the source function S is given by :

$$S(\underline{r}, t) = \rho_0 \frac{\partial q}{\partial t} - \nabla \cdot \underline{f} \tag{4.2}$$

In the source term, q is the volume displacement per unit time per unit volume, and $\underline{f}$ is the force per unit volume acting on the fluid. These represent the thickness and loading sources respectively [38]. For convenience, only the solution will be mentioned here. For a full derivation of the far-field prediction method, the reader is referred to Chapter 5 in [38].
According to Hanson in [38], the general equation for the far-field pressure harmonic is given by Equation (4.3). Here ρ_0 is the ambient density, c_0 is the speed of sound of the fluid, B is the number of blades, θ is the radiation angle from the propeller axis to the observer point, n is the order of the harmonic, q is the unsteady loading order, y is the observer distance to the propeller axis, D is the propeller diameter, M_x is the flight Mach number, M_r is the section relative Mach number, M_t is the tip rotation Mach number, and z is the normalized radial source integration variable ($z = r/R_{tip}$).

$$\begin{aligned} P_{n,k} &= \frac{-\rho_0 c_0^2 B \sin\theta \, e^{i\left[(n+q)\frac{\Omega r}{c_0} - sign(n+q)\frac{|n|\pi}{2}\right]}}{8\pi\frac{y}{D}\left(1 - M_x\cos\theta\right)} \\ &\times \int_0^1 M_r^2 e^{i\phi_{os}} \Psi_n\left(k_x\right) J_{|n|}\left[\frac{|n+q| z M_T \sin\theta}{1 - M_x\cos\theta}\right] dz \end{aligned} \tag{4.3}$$

Equation (4.3) can basically be split up into two parts: a part which remains constant, and a radial integration part. The first part is independent of the sections, while the terms in the radial part depends on the section. Essentially four terms affect the radial integration:

- the section relative Mach number,
- the phase delays due to sweep and blade offset,
- the loading source term: $\Psi_n\left(k_x\right)$,
- and a Bessel function describing the radiation efficiency of the noise of interest.

The effects of sweep and lean (blade offset) are taken into account with the phase lag term ϕ_{os}. This factor is the summation of the separate phase delays due to sweep and lean:

$$\phi_{os} = \phi_o + \phi_s \tag{4.4}$$

The phase delays due to sweep and lean are given by Equation (4.5) and Equation (4.6), where FA and MCA were defined in **??**.

$$\phi_o = \frac{2mB}{z\sigma}\left(\frac{a^2 z^2 M_x \cos\theta}{1 - M_x\cos\theta} - 1\right)\frac{FA}{D} \tag{4.5}$$

$$\phi_s = \frac{2a}{\sigma}\left(\frac{mB}{1 - M_x\cos\theta}\right)\frac{MCA}{D} \tag{4.6}$$

Where a and σ are two velocity ratios given by Equation (4.7) and Equation (4.8):

$$a = \frac{\Omega r_T}{V} = \frac{M_T}{M_x} \tag{4.7}$$

$$\sigma = \frac{U}{V} = \frac{M_r}{M_x} \tag{4.8}$$

The general source term $\Psi_n(k_x)$ which appears in Equation (4.3) is given by Equation (4.9)

$$\Psi_{n,k}\left(k_x\right) = k_x^2 t_b \Psi_v\left(k_x\right) + i\Psi_{Fk}\left(k_x\right) + B_D \Psi_{rk}\left(k_x\right)\frac{\partial}{\partial z}(\cdot) \tag{4.9}$$

Equation (4.9) contains three terms:

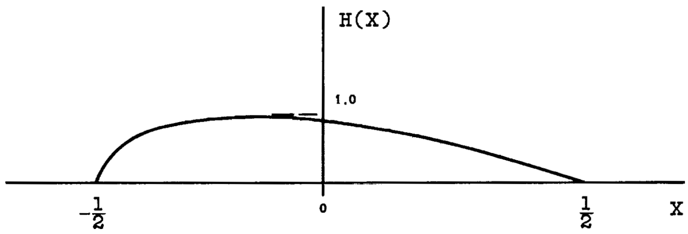

Figure 4.2: Example of a normalized sectional thickness distribution $H(X)$, from Ref. [38, p.107]

- a thickness source: $k_x^2 t_b \Psi_v(k_x)$,
- a loading source: $i\Psi_{Fk}(k_x)$,
- and a radial source: $B_D \Psi_{rk}(k_x) \frac{\partial}{\partial z}(\cdot)$

Since only linear sources are considered in this study, the radial source is neglected. This leaves the thickness and loading sources.

The thickness noise source term $\Psi_v(k_x)$ is given by Equation (4.10):

$$\Psi_v(k_x) = \int_{-\frac{1}{2}}^{\frac{1}{2}} H(X) \exp(ik_x X)\, dX \tag{4.10}$$

Where $H(X)$ is the normalized sectional thickness distribution, where the maximum thickness of the section equals 1. The normalized chord variable X, ranges from -0.5 to 0.5. Figure 4.2 shows an example of a normalized sectional thickness distribution.

Another important source term is the loading source $\Psi_{Fk}(k_x)$, which accounts for the axial and tangential loading on the blade. In the conventional formulation of Hanson [25], this loading is expressed in terms of lift and drag forces, leading to Equation (4.11):

$$\Psi_{Fk} = k_y \left(\frac{C_{Lk}}{2}\right) \Psi_{Lk}(k_x) + k_x \left(\frac{C_{Dk}}{2}\right) \Psi_{Dk}(k_x) \tag{4.11}$$

However, to compute the lift and drag forces on the blade, the angle of attack of the blade with respect to the inflow must be known, which could not be obtained from FlightStream. Therefore, an alternative derivation by Hanson is used [38], where the thrust and torque forces appear explicitly as non-dimensional force coefficients in the loading source term, given by:

$$\Psi_{Fk} = -a(\omega - n - q) B_D \left(\frac{C_{f_x}}{2}\right) \Psi_{xk}(k_x) - \frac{n}{z} B_D \left(\frac{C_{f_\phi}}{2}\right) \Psi_{\phi k}(k_x) \tag{4.12}$$

Where ω is the wavenumber integration variable in the axial direction [38]. Equation (4.12) combines the axial and tangential force components instead of the lift and drag components. The axial source term $\Psi_{xk}(k_x)$ and tangential source term $\Psi_{\phi k}(k_x)$ are determined using Equation (4.13) and Equation (4.14), respectively.

$$\Psi_x(k_x) = \int_{-\frac{1}{2}}^{\frac{1}{2}} f_x(X) \exp(ik_x X)\, dX \tag{4.13}$$

$$\Psi_\phi(k_x) = \int_{-\frac{1}{2}}^{\frac{1}{2}} f_\phi(X) \exp(ik_x X)\, dX \tag{4.14}$$

$f_x(X)$ and $f_\phi(X)$ are the normalized sectional axial and tangential force distributions, whose areas integrate to unity. An example of the normalized distribution of force in axial direction of a section can be seen in Figure 4.3. Subsequently, the force coefficient at radial position r/R_{tip} is obtained by

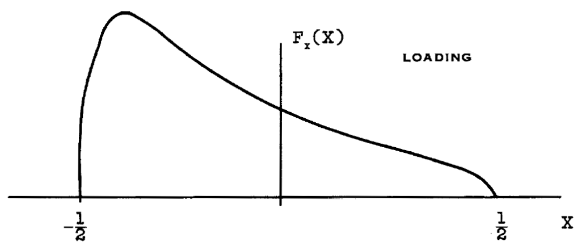

Figure 4.3: Example of a normalized axial loading distribution $F_x(x)$on a radial section, from Ref. [38, p.107]

integrating the dimensional chordwise distribution as follows (in this case for the axial loading):

$$c_{f_x} = \int_{-1/2}^{1/2} f_x(X)\mathrm{d}X \tag{4.15}$$

The equation is the same for the tangential loading, except for a subscript change. After the axial and tangential loading is scaled as described in Section 3.2.5, the coefficients that are used in the Hanson method are determined with the following equation:

$$c_f = \frac{F}{\frac{1}{2}\rho V_{eff}^2\, c\, dR} \tag{4.16}$$

Where F is the scaled force either in axial or tangential direction at radial position r/R_{tip}, V_{eff} is the effective velocity equal to $\sqrt{V_\infty^2 + z^2\Omega^2 R_{tip}^2}$, c is the chord length, and dR is the spanwise segment width. The thickness source term Ψ_v, as well as the axial loading source term Ψ_x and tangential loading source term Ψ_ϕ are functions of the non-dimensional chordwise wave number k_x. This chordwise wave number is determined with:

$$k_x = \frac{2a}{\sigma}\frac{mB}{1 - M_x\cos\theta}B_D \tag{4.17}$$

According to Hanson [38], in the far-field case, ω in Equation (4.12) can be replaced by the stationary phase point, which is given by Equation (4.18) :

$$\omega_0 = \frac{n+q}{1 - M_x\cos\theta} \tag{4.18}$$

Neglecting unsteady noise ($q = 0$), substituting Equation (4.18) in Equation (4.12), and using that $n = mB$, the following equation for the overall source term $\Psi_{mB}(k_x)$ is obtained:

$$\Psi_{mB} = k_x^2 t_b \Psi_v(k_x) + i\left(-a\left(\frac{mB}{1 - M_x\cos\theta} - mB\right)B_D\left(\frac{C_{f_x}}{2}\right)\Psi_x(k_x) - \frac{mB}{z}B_D\left(\frac{C_{f_\phi}}{2}\right)\Psi_\phi(k_x)\right) \tag{4.19}$$

Substituting Equation (4.19) for the general source term in Equation (4.3), and using the same substitutions as before, Equation (4.3) can be rewritten to finally obtain Equation (4.20) [38]:

$$P_{mB} = \frac{-\rho_0 c_0^2 B\sin\theta e^{i\,mB\left[\frac{\Omega r}{c_0} + \frac{\pi}{2}\right]}}{8\pi\frac{y}{D}(1 - M_x\cos\theta)} \times \int_0^1 M_r^2 e^{i\phi_{os}}\Psi_{mB}(k_x) J_{mB}\left[\frac{mBzM_T\sin\theta}{1 - M_x\cos\theta}\right]dz \tag{4.20}$$

Equation (4.20) is equal to Equation (36) in [36], except that the lift and drag forces in the loading source term are replaced by axial and tangential forces. The overall waveform P_{mB} is obtained by summation of the thickness, axial loading and tangential components:

$$P_{mB} = P_V + P_{F_x} + P_{F_\phi} \tag{4.21}$$

This is the waveform for each harmonic mB. To compute the waveform as a function of time, a Fourier series transformation must be applied as in Equation (4.22)

$$p(t) = 2\mathrm{Re}\left[\sum_{m=1}^{\infty} P_{mB} \exp(imB\Omega t)\right] \tag{4.22}$$

Where Re means the "real part of". The root mean square signal of the wave is obtained with Equation (4.23).

$$p_{rms} = \sqrt{\frac{1}{T_2 - T_1}\int_{T_1}^{T_2} p(t)^2 dt} \tag{4.23}$$

Where T_1 and T_2 are the lower and upper time bounds of the integration, respectively, since the sound pressure, p is cyclic, the boundaries can be chosen such that they cover exactly one rotation of the blades. The Sound Pressure Level or SPL is the logarithmic measure of the effective pressure of a sound relative to a reference pressure. The SPL of the wave can be obtained with:

$$SPL = 20\log_{10}\left(\frac{p_{rms}}{p_0}\right) \tag{4.24}$$

Where p_0 is the reference pressure, typically, a reference pressure of 2.0×10^{-5} Pa is used since this is the threshold value that the human ear can still detect. Even though the SPL gives an indication of the loudness of a noise source, this metric does not account for a difference in thrust or size between two propellers. Since this is important when comparing the noise between propellers, another metric of the sound pressure is defined, known as the Thrust Specific Sound Pressure or TSSP. The TSSP is obtained by relating the acoustic pressure p_{rms} to the pressure jump over the propeller disk (T/D^2). This allows for physics-based scaling between different propeller geometries [39]. The thrust specific sound pressure is defined as [40]:

$$TSSP = 20\log_{10}\left(p_{rms}\frac{D^2}{T}\right) \tag{4.25}$$

The TSSP similar to SPL is in deciBel (dB).

5

Propeller Blade Parameterization, Geometry Generation and Discretization

Parameterization of the propeller blade is necessary to carry out the intended research. If no form of parameterization is used, countless coordinate points will have to be altered to change the propeller blade shape. This is infeasible. By implementing a parameterization, the blade shape can be described using a mathematical representation. As a result of the parameterization, the number of design variables is reduced to only a few, and the parameterization ensures that the shape is smooth and continuous [18].

The design parameters which define a propeller blade, along with an explanation of whether they are parametrized or kept constant, are discussed in Section 5.1. Most of these parameters are a distribution along the radius of the blade. However, there are also some which are a single value, such as the collective pitch. The radial distributions are parameterized with Bézier curves. A discussion on possible parameterization methods and the choice for the Bézier curve is discussed in Section 5.2.

When all the propeller design parameters are defined, these are provided as inputs to a tool called the *Multi-Model Generator*. In Section 5.3 it is explained how a 3D propeller blade shape is generated using this tool. Besides the propeller blades, also a propeller nacelle is modeled. The nacelle shape is kept constant during this study. Finally, in Section 5.4 it is explained how the propeller geometry is discretized such that it can be evaluated using the panel method implementation, which is discussed in Chapter 3.

5.1. Propeller Design Parameters

The design parameters that define the shape of a propeller blade can be divided into three categories: the 2D cross-sectional shape, 3D design variables, and overall propeller design variables. First, the 2D cross-sectional characteristics are discussed.

2D cross-sectional shape

The **airfoil shape** of the propeller blade is a cross-sectional design variable, which varies along the blade radius. Generally, the outboard sections of the propeller blade are thinner than the sections inboard of the blade. This is related to the rotational velocity, which increases with the radius of the blade. The airfoil shape can be given by NACA airfoils, or a parameterization such as the Bézier curve that will be mentioned in Section 5.2 can be used. However, including the airfoil shape as a design variable increases the computational effort of this study. Since the focus of this thesis is on blade sweep, the airfoil shapes of the 25 sections which are used are kept constant along the blade radius. The airfoil shapes from the baseline propeller, the XPROP are used throughout this study.

3D propeller design variables

Besides the 2D cross-sectional shape, there are a number of design variables that define the propeller in three dimensions. These are the following:

- The **twist distribution** $\beta(r)$ is the distribution of the twist angle along the radius of the propeller.

The twist angle of a section at radial position r is defined as the angle between the chord line of the section and the chord line of the airfoil section at 70 % of the radius of the blade. Since the inflow angle changes along the radius of the blade, the twist angle along the blade radius should be varied as well to achieve an optimal loading distribution. However, since the focus of this study is on the effect of sweep, the twist distribution is kept constant. The twist distribution of the baseline propeller is used in this study. The twist distribution can be seen in Figure 5.1. In the figure, the pitch is 0 degrees.

- The **chord distribution** is defined as the chord length of an airfoil section at radial position r along the radius of the blade. Similarly, for the twist angle, to account for differences in inflow angle along the blade radius, the chord length should be varied to achieve an optimal loading distribution. Besides the twist distribution, also the chord distribution is kept constant in this study since the focus is to study the effect of sweep on the propeller aerodynamics and aeroacoustics. The chord distribution from the baseline propeller is used throughout this study and can be seen in Figure 5.1.

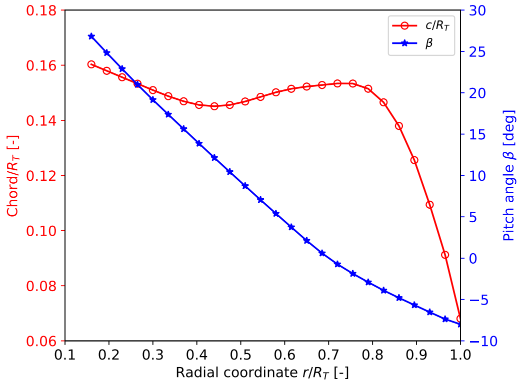

Figure 5.1: Twist and chord distribution of the XPROP propeller. The twist distribution is given with a collective pitch of 0 degrees at r/R_{tip} =0.7

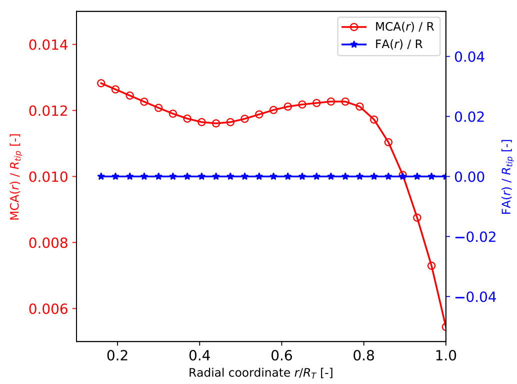

Figure 5.2: Mid-chord alignment and Face alignment distribution of the XPROP propeller. The Mid-chord Alignment is given relative to the Pitch Change Axis, which is the line parallel to the root plane at 42 % of the root chord line

- The **Mid-Chord Alignment** or sweep is defined as the offset between the mid-chord point and the pitch-change axis parallel to the root plane, which is shown in Figure 5.3.

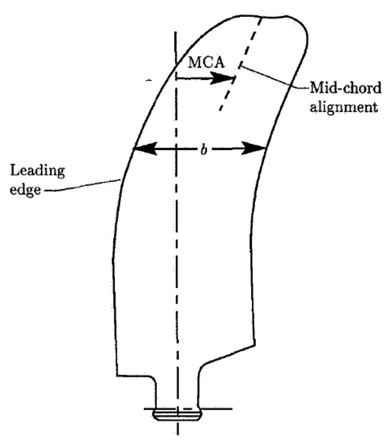

Figure 5.3: Definition of mid-chord alignment, from [23, p.16]. The letter b is defined as the chord length of the blade.

As mentioned in Section 2.2.3, blade sweep can lead to destructive interference of the noise signals emanating from different portions of the blade, which can result in a decrease in acoustic pressure of the propeller. This is the main parameter of investigation in this study. A fully dependent variable of the mid-chord alignment is the sweep angle at radial position r given by $\Lambda(r)$. It is determined with:

$$\Lambda_{\mathrm{i}} = \arctan\left(\frac{MCA_{\mathrm{i}+1} - MCA_{\mathrm{i}}}{r_{\mathrm{i}+1} - r_{\mathrm{i}}}\right) \tag{5.1}$$

The sweep angle is accurately determined if the distance between adjacent blade sections is small. In aircraft wing design, usually, the sweep angle at quarter chord length of the wing is used. However, in this thesis, the sweep angle at mid-chord is used since out of plane movement at the leading edge and trailing edge is averaged in this fashion [39]. A detailed explanation for the reason to choose for mid-chord sweep in favor of quarter-chord sweep can be found in the work of Burger [17].

- Another offset of the blade is the **Face Aligment** or lean. This is the offset normal to the advance direction of the section. Similar to the mid-chord alignment and sweep angle, the lean angle is fully dependent on the face alignment. The definitions of the mid-chord alignment and face alignments are shown in **??**. The definitions for the mid-chord alignment and face-alignment distributions of the XPROP were shown in Figure 4.1. It can be seen that the face alignment is zero, but the mid-chord alignment distribution of the XPROP is nonzero. This is not an error but is a result of the pitch change axis being located at 42 % on the chord line of the blade root. If it is located at the mid-chord point on the root section, then the MCA distribution would be zero along the blade radius. As a result of using this definition, the mid-chord alignment of the XPROP, in this case, is not zero but has an offset of 8 % of the chord length at each radial station of the XPROP. However, in the sensitivity study, the maximum amount of sweep can become 30 times greater. Therefore, it is assumed that the baseline propeller has zero sweep. For the definition of the bounds for sweep, see Section 7.1.

Overall design variables

Besides the radial distributions, there are several parameters that define the overall characteristics of the propeller:

- By increasing **the propeller diameter** D_p, the amount of air mass that the propeller accelerates is increased, thereby increasing the propeller efficiency. However, increasing the propeller diameter also increases the tip Mach number, which increases propeller noise. Additionally, increasing the diameter also leads to a penalty in terms of structural, weight, and sizing aspects, and therefore the propeller diameter is often constrained. Including the effect of the diameter is out of the scope of this thesis. Therefore, the diameter is kept constant and is set to the diameter of the baseline propeller.

- Increasing the **number of blades** B increases the propeller efficiency, as blade tip losses are reduced [41]. Additionally, increasing the blade number is also favorable in terms of noise since this affects the fundamental frequency as well as acoustic interference. However, from a structural point of view, fewer blades with a large chord are preferred to keep blade stresses low and reduce the risk of flutter [41]. A fewer number of propeller blades are also preferred, as this reduces the mechanical complexity of the hub. Including the blade number is considered out of the scope of this thesis, and thus the blade number is kept constant.

- The **collective pitch** $\beta_{.7R}$ is the angle of the chord line of the airfoil section at 70 % radius of the blade and the propeller rotation plane. This means that if the collective pitch is 0 degrees, the chord line at 0.7 R_{tip} runs parallel with the propeller rotational plane. The collective pitch is varied for each design to make sure that the thrust matches a thrust requirement, which is defined in Chapter 7.

Of the aforementioned parameters, only the Mid-chord alignment and collective pitch are varied in this thesis. The collective pitch is a single value, while the Mid-Chord Alignment is a radial distribution and therefore should be parameterized. In the next section, possible parameterizations for sweep are discussed, along with the implementation that is used in this thesis, the Bézier curve.

5.2. Parameterization of the Radial Distribution of Sweep

Different parameterizations for radial distributions exist:

- **Bézier Curves**

  The Bézier curve is a parametric curve that is frequently used in computer graphics [42]. It is defined by a set of control points, where the first and last control point are the endpoints of the curve. However, the intermediate points generally do not lie on the curve. By moving the control points, the curve's shape changes. Bézier functions are often used in shape optimizations [43] and require relatively few parameters.

- **NURBS**

  The Non-Uniform Rational B-Spline (NURBS) is also frequently used in CAD [42] and is a more generalized version of the Bézier curve. The basis of the NURBS is the B-spline or basis spline. When the weight of the NURBS is equal to 1, it is simplified to a B-spline. The NURBS offers a lot of design freedom, but the number of design variables may rise quickly.

- **Polynomials**

  Other methods are based on using polynomials to define a curve, like how the NACA airfoils are defined. Although these offer a lot of freedom, they suffer from the relatively large amount of parameters and the unpredictable behavior they can have, which might result in non-smooth shapes [18].

Most works in propeller blade or airfoil optimization rely on B-splines or Bézier curves [15]. The author prefers the Bézier curve over the B-spline because of its simplicity, and since similar research have applied it successfully [14] [17] [39]. The Bézier curve requires relatively few parameters yet allows for a wide range of sweep distributions that are continuous and smooth. The implementation of the Bézier curve is discussed in the next section.

Bézier Curve implementation for Sweep

A Bézier curve is used to parameterize sweep in this study. A Bézier curve consists of a set of Bernstein polynomials between control points to generate a curve. The explicit formula for the Bézier curve is given by Equation (5.2). In Equation (5.2), $\mathbf{P}_i$ is the i-th control point. The degree of the curve is given by n. Then the number of points of the curve should be at least $n+1$. In two dimensions, each control point is defined by the coordinates (X, Y). The X-coordinate represents the normalized sweep value, and the Y-coordinate the normalized radial position. The first and last control point are the start and endpoints for the curve. This means that the Y-coordinates of the first and last point must be 0 and 1.

$$\mathbf{B}(t) = \sum_{i=0}^{n} \binom{n}{i} (1-t)^{n-i} t^i \mathbf{P}_i \tag{5.2}$$

In this study, a degree of 3 was chosen for the sweep Bézier curve, which results in four control points and eight design variables. However, for the sweep distribution, there are two constraints:

1. The Y-coordinates of the first and fourth control point have to match the blade root and tip, so they must be 0 and 1. This leaves 6 out of 8 variables.

2. Blade sweep at the root can only be 0. The values of the upper and lower bounds of blade sweep are chosen such that 0 sweep is equal to a normalized sweep value of 0.5. This leaves five design variables to define the sweep Bézier curve: the X and Y-coordinates of the second and third control points and the X-coordinate of the fourth control point.

An example of a Bézier curve for blade sweep is given in Figure 5.6. The coordinates of the control points can be found in Table 5.1. The coordinates which are marked with an asterisk (*) are the design variables.

The control point values are randomly generated numbers that vary between 0 and 1. For some combination of control points, this range may lead to extreme gradients at the root or the tip when the relative sweep difference is large, but the points are located close to the root or tip, such as in Figure 5.4

and Figure 5.5. The gradients at the tip can be higher than for the root, since the last point's sweep value is allowed to vary. Rather than constraining the design values for blade sweep, it is chosen to constrain the radial position of the second and third control point. The Y-coordinates of the second and third control point are allowed to vary between 30 and 85 % of the normalized blade radius. This is indicated by the green shaded region in Figure 5.6. In the next section, it is explained how a sweep distribution is extracted from the Bézier curve, and is used as input to generate a blade planform.

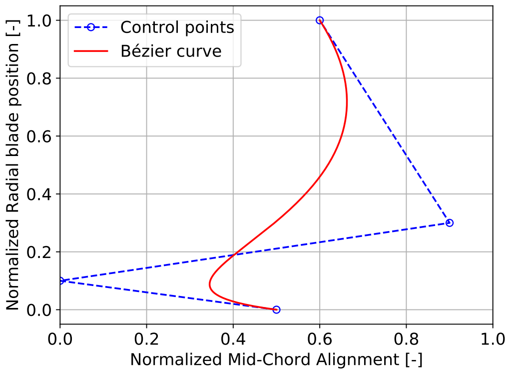

Figure 5.4: Example of a Bézier curve with extreme root sweep gradient

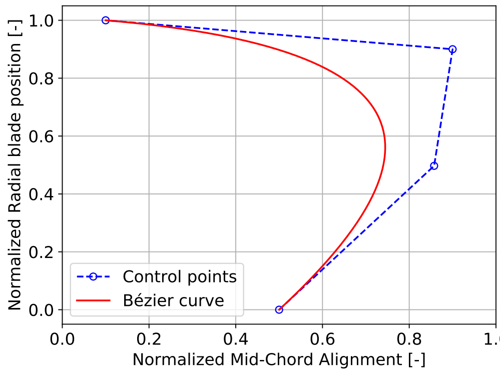

Figure 5.5: Example of a Bézier curve with extreme tip sweep gradient

Table 5.1: Example Bézier control point coordinates

X-coordinate	Y-coordinate
0.5	0.
0.8574 *	0.4971 *
0.3034 *	0.8319 *
0.6104 *	1.0

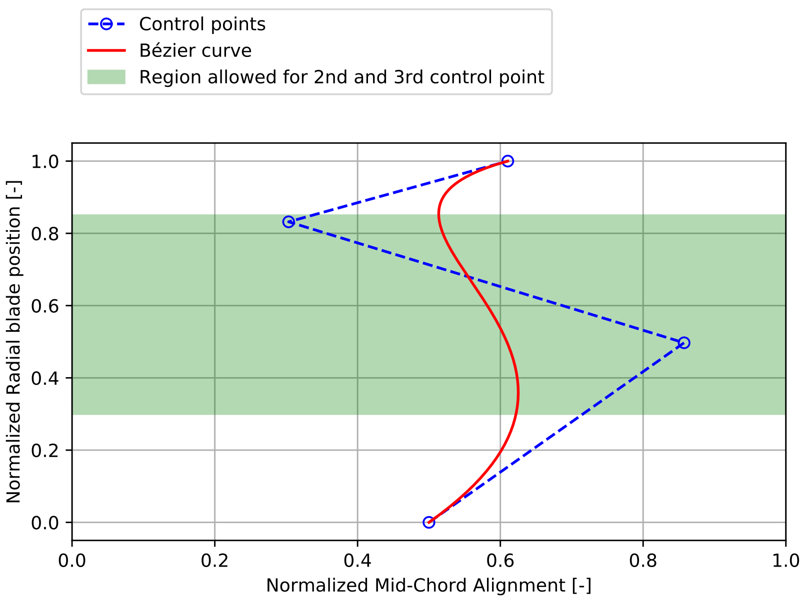

Figure 5.6: An example of a Bézier curve for sweep

5.3. Propeller Geometry Generation

Generating the blade and nacelle manually using Computer-Aided Design (CAD) programs such as CATIA is too time-consuming. Instead, an approach is preferred where new geometries can be generated by simply changing the values of the design variables. As it is the goal in this thesis to assess multiple designs within certain bounds of a list of design variables, a fully automatic rule-based topology approach is required. This can be achieved with the use of a system that incorporates Knowledge-Based Engineering (KBE). In KBE, knowledge about a process is captured and stored in dedicated software applications, such that it can be directly exploited and reused in designing new products [44]. It is often used to support Multidisciplinary Design Optimization (MDO). KBE can support hands-off manipulation of geometrical products better and faster than classical CAD systems [44]. Most of the KBE systems are based on the object-oriented language Lisp [45]. However, this programming language is outdated and difficult to learn. Instead, it is chosen to use the ParaPy [1] platform, which is based on the Python programming language.

The ParaPy Platform

The ParaPy platform is an object-oriented language, using the typical class definitions, along with setter and getter methods. ParaPy classes contain key functionalities such as dependency tracking and caching, which can reduce the execution time significantly. A Class containing a method only needs to be initiated once, taking the majority of the time, but once the class is initiated, the method that is to be repeated will take significantly less time compared to using normal function definitions. Besides the base class, there is also a geometry base class, which gives special properties to objects, such as position and orientation. Based on this platform, an aircraft-modeling tool was developed in-house at Delft University of Technology [45]. Initially, this tool was conceived to model aircraft geometries, but it has been adapted to generate propeller geometries.

The Multi-Model Generator Tool

The Multi-Model Generator (MMG) is an aircraft modeling tool conceived by La Rocca and others originally in ICAD [45]. After ICAD became unavailable, the tool was re-built with the ParaPy platform. MMG works with solids. Each geometry, e.g. blade or nacelle, represents a solid in ParaPy. A combination of topologies is generated through fusion. This leads to intersections, creating new faces and edges. The great advantage of ParaPy is that it allows dependency tracking of the fused parts. The main class or SuperClass of MMG is the **Aircraft** Class, from which an Aircraft object can be instantiated. An Aircraft object can consist of wing-, and fuselage-like geometries, which in turn are generated by separate dedicated Classes. The following three modules are the most relevant in generating the wing and fuselage-like geometries:

1. the DARWing module, from which a wing topology is generated using the *Rails* methodology.
2. the DARFuse module, from which a fuselage topology is generated.
3. and the FlightStreamMesher module, from which a mesh is generated.

These modules, in turn, consists of dozens of other classes at lower levels. For more detailed information, the reader is referred to the work of Jian Wei [45]. The topology of the propeller blades is generated using the DARWing module in MMG. This module can generate two types of wing-like topologies: a clean wing or a multi-elements wing, such as a box-wing type configuration. For the generation of propeller blades, the clean wing method was used.

5.3.1. The Clean Wing Method

The clean wing procedure consists of four steps, which are shown graphically in Figure 5.7. The first step is to generate a pair of **rails**: a leading edge rail and a trailing edge rail. These rails lie in the XY plane and contain no information about the twist and Face Alignment or lean distribution. If provided, twist and face alignment will be applied to the rails. In the second step, the airfoil curves are positioned and oriented at specified spanwise locations between the leading edge and trailing edge rails. In the third step, wing trunks are generated by ”lofting” between the airfoil curves. Finally, the clean wing is obtained by sewing all the wing trunks together into one solid shape [45].

[1] `https://parapy.nl`, accessed 18-3-2021

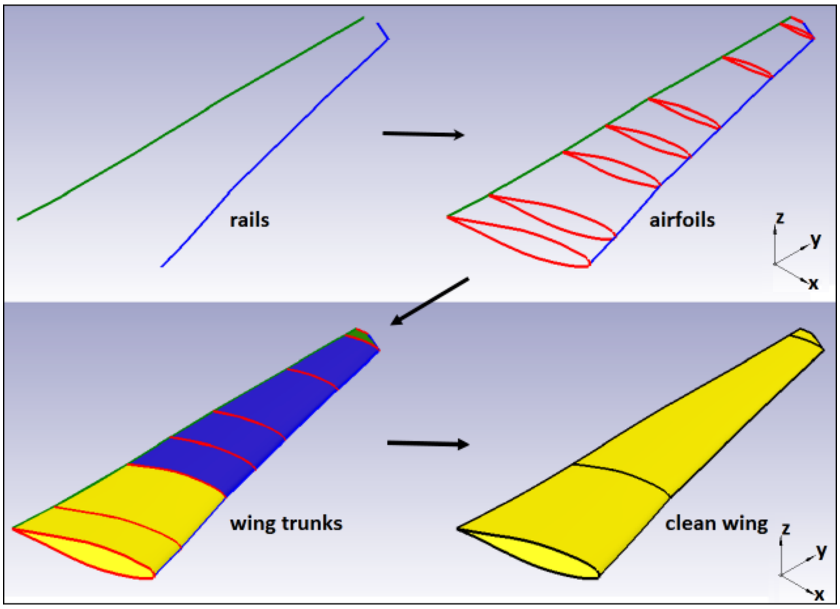

Figure 5.7: Procedure of the generation of a clean wing, from Ref. [45, p. 18]

To generate a clean wing-type geometry, two sets of inputs are required. The first relate to five curves [45]:

- **the flat leading edge curve.**
- **the flat trailing edge curve.**
- **the dihedral line.**
- **the twist axis.**
- **the twist points.**

With ”flat,” it is meant that the curve lies in the XY-plane. The leading and trailing edge curves X-coordinates are determined by adding or subtracting a half chord length to the mid-chord alignment. An example can be seen in Figure 5.8. Besides these five curves, also the airfoil shapes need to be defined to generate a blade. As mentioned before, the airfoil shapes are taken from the XPROP baseline propeller. The input parameters for the shapes are [45]:

- **airfoils**: A list of strings that contain the relative paths to the airfoil coordinate data. The length of the list determines the number of radial sections. This must be consistent with the other input parameters, such as the span positions, kink indices, airfoil thickness, etc.
- **span_positions** is a list of normalized Y-coordinates ranging from 0 to 1. These determine the spanwise position of the airfoil coordinates.
- **kink_indices** is a list of integers, where each integer represents the index of the **span_positions** input list. This index can be used to retrieve the spanwise position of a kink.
- **airfoil_thickness** is a list of thickness percentages for each airfoil curve. These are used for scaling the thickness of the airfoils. By default, the airfoil thicknesses were fixed to their original values, i.e., 100 (%).
- **airfoil_cant** is a list of strings. It determines the orientation of the airfoil curves when observed from above the wing [45]. By default, this is set to ”streamwise”. For other possible settings, see the work of J. Wei [45].

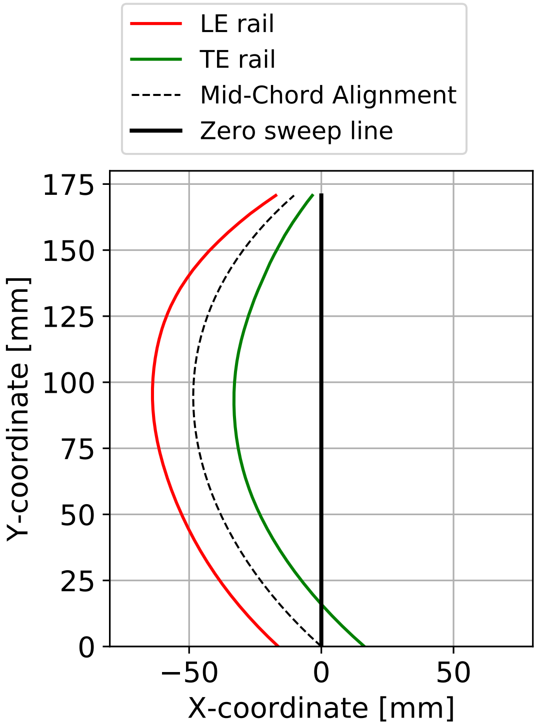

Figure 5.8: Example of a swept blade planform

- and **follow_dihedral** is a list of zeros or ones. The zeros or ones indicate the option for orienting the airfoil curves when observed from the front. The default is set to the ”vertical orientation” or 0.

These rails inputs are generated from the design parameters through a Parapy class called ”PropJSONWriter” which was created by the author. This class reads in the propeller design parameters, which are discussed in Section 5.1 and then generates a blade rails file.

A rails file consists of geometry definitions for each geometry, e.g., a blade or a nacelle, that is to be created with MMG. Inside the file, each geometry must be given as a dictionary with the following five inputs as keys:

- **is_mirrored**. This is a string that determines if a blade geometry should be mirrored in the XZ plane. By default, this is set to False. This option was not used since mirroring was not applicable to blade geometries. Instead, each blade was added separately.
- **rails**. This is a dictionary that contains data of the five rail curve inputs mentioned previously.
- **position**. This is also a dictionary that contains the position and orientation information of the blade geometry.
- **parameters**. This is a dictionary that contains the airfoil curve inputs mentioned previously. And lastly:
- **movables_parameters**. This is a dictionary containing inputs related to movables, e.g., flaps or hinges. Since there are no movables on the blades, each item in this dictionary is an empty list.

The process from control points to blade topology is summarized in Figure 5.9. Next, the generation of the nacelle geometry is discussed.

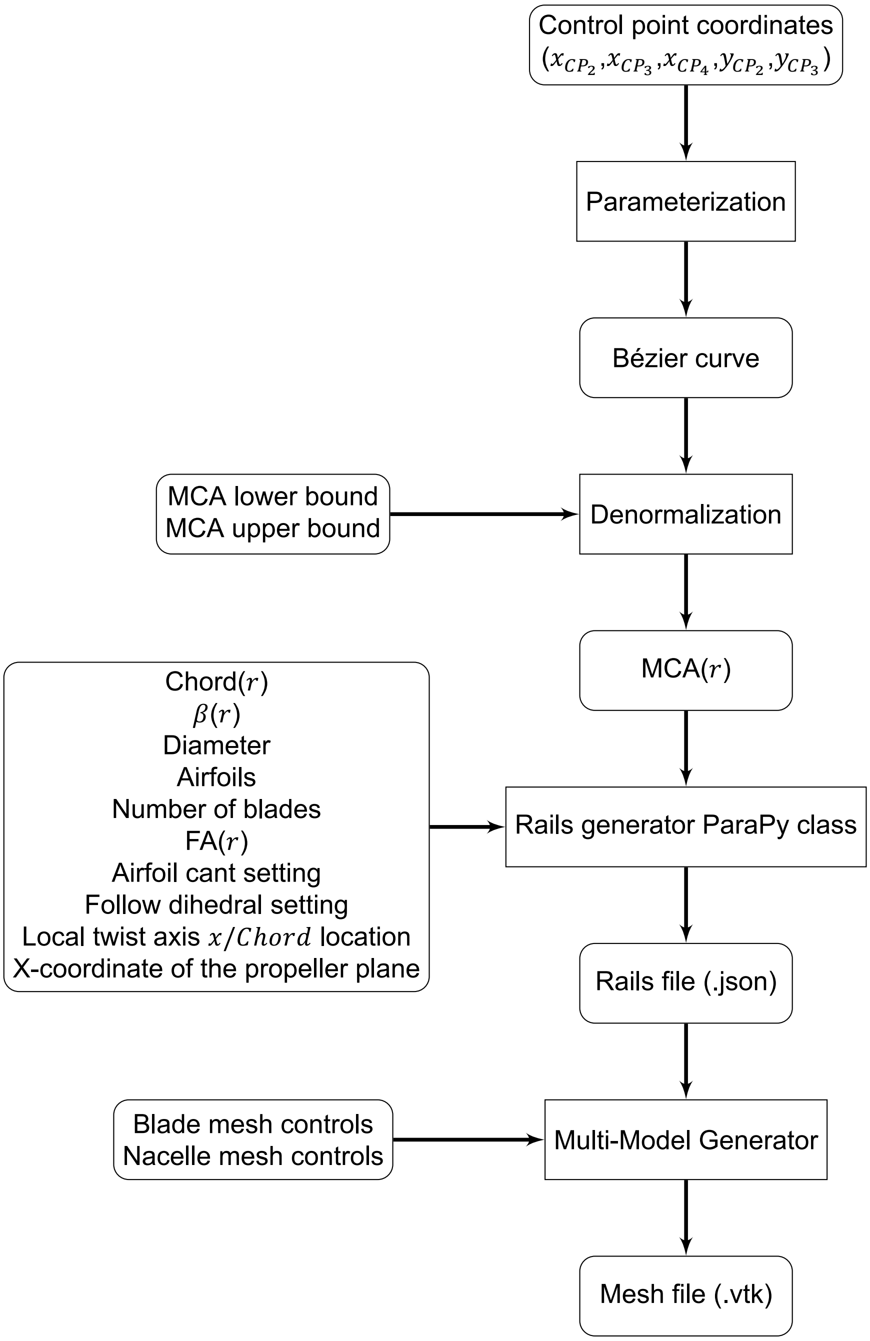

Figure 5.9: Flowchart showing how a generic swept blade mesh is obtained from a set of 5 design variables in the study

5.3.2. Nacelle Geometry

Besides the propeller blades, a nacelle was modeled to include the interaction effects of the nacelle on the blades and to validate the results of FlightStream with experimental data. The validation of FlightStream is discussed in Section 3.3. The dimensions of the nacelle were kept constant and are shown in Figure 5.10. The geometry consists of the following three sections:

1. a spinner.
2. a cylinder with a constant radius of 44.22 mm.

3. a trailing cone section

The spinner geometry has been taken from the XPROP setup in [34]. The other two sections were added manually. The radial dimensions of the XPROP spinner and the trailing cone section can be found in Appendix A. The nacelle topology was originally created with OpenVSP, a parametric aircraft geometry tool developed by NASA[2]. The geometry was exported as a STEP file and imported into MMG with the FuselageInputFromStep class. This class reads the geometry in the STEP file and then cuts the nacelle in sections along the longitudinal direction. The result is a JSON file containing the XYZ data of the sections.

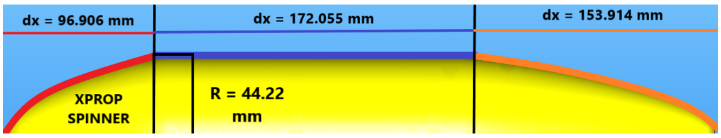

Figure 5.10: Side view of the nacelle topology from ParaPy

Using the DARFuse module inside MMG, the JSON file of the nacelle is imported, and a simplified Fuselage Solid is generated by interpolating a Surface through the point data, see Figure 5.11. After the fitting, two small holes are created at the nose and tail. These are filled by generated two small faces. The discretization of the geometry is discussed next.

5.4. Geometry Discretization

The discretization of the geometry in MMG is performed with the AircraftFlightStreamMesher() class in MMG. This class is similar to the MMGMesher class described in J. Wei's work [45], but the difference is that this class is written for the panel method FlightStream instead of VSAERO. Like the MMGMesher class, the AircraftFlightStreamMesher class is based on the built-in Parapy mesher [45]. This consists of a library of high-level, declarative classes which wrap around the low-level C++ kernel functionality in Salome [46]. It uses a set of meshing algorithms and conditions to compute the mesh on the boundaries of the solids or Boundary Representation (BRep) models in Parapy [45].

Meshing a BRep model in MMG requires three inputs, which are:

1. **shape_to_mesh**, the topology that needs to be meshed. The input can be a Solid, a Shell, a face, or an edge of a model [45]. In this case, the shape_to_mesh that is given to MMG is a fusion of blades and nacelle topology. The nacelle topology in itself consists of a small nose and tail face at the front and back, respectively, and the majority of the body. In addition, a lateral splitter curve was added slightly behind the longitudinal position of the blades, splitting the main

[2] http://openvsp.org/, accessed on 23-3-2021

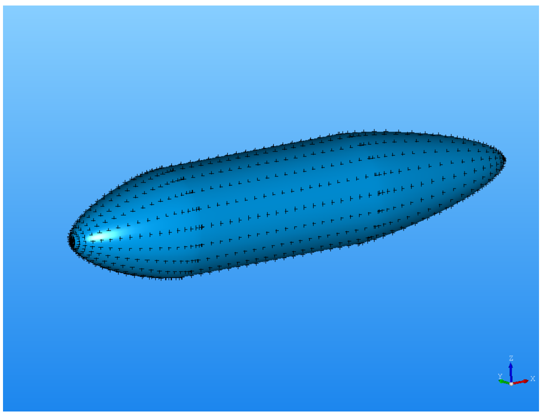

Figure 5.11: Point data and Simplified Fuselage Solid obtained by interpolation

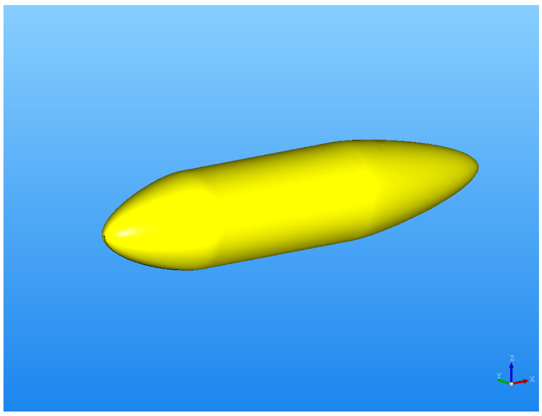

Figure 5.12: Fuselage Solid obtained by sewing the surface obtained from interpolation and the nose and tail faces

nacelle body into two groups: the spinner and a trailing part aft of the blades. This was done for post-processing purposes in FlightStream to be able to distinguish forces and moments for the spinner independently. The resulting shape_to_mesh of the XPROP blades can be seen in **??**.

2. **controls**, a set of inputs that define the rules of the mesh of the input shape.
3. **groups** is used to create a link between the sub-grids of a mesh with the sub-shapes of the input shape. It allows the user to retrieve mesh information of the sub-shapes.

The set of controls that should be used to discretize a geometry depends on the type of mesh that is desired. Two types of meshes can be generated in MMG: structured meshes and unstructured meshes. The unstructured mesher does not impose any constraints, while the structured mesher imposes restrictions on the models to obtain a checkerboard pattern. Unstructured meshes are versatile, but they take longer to compute than structured meshes [45]. For the blades, it is desirable to generate a structured mesh, even though FlightStream can also account for unstructured wing meshes [29]. The cells will be aligned in both the spanwise and chordwise directions, which is important for the evaluation of forces and coefficients on the blade. The mesh controls for the blades are the **chordwise number of points** and the **spanwise pitch**, which are shown in Figure 5.13. While the chordwise points can be any positive number, the spanwise pitch is limited by the length of the longest edge of each spanwise chain [45]. For example, if the maximum leading or trailing edge size of the blade is 7.1 mm, then this is also the maximum spanwise pitch that can be attained. If the spanwise pitch is smaller than this value, then that section will be split into two segments or more, depending on the ratio of the edge size of each segment to the spanwise pitch.

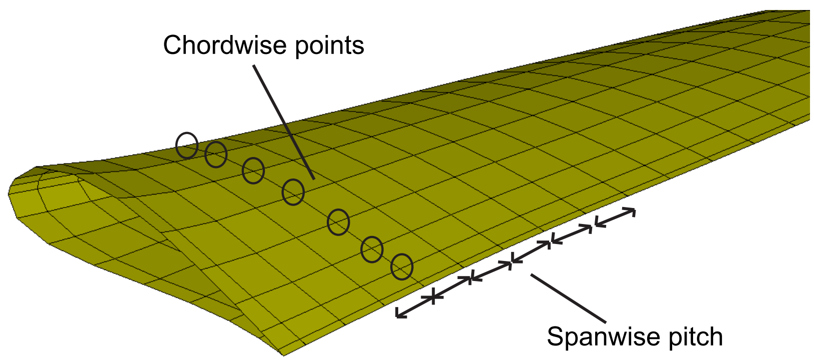

Figure 5.13: Principle mesh control of the blades: chordwise number of points and spanwise pitch

Concerning the nacelle topology, this doesn't necessarily need a structured mesh, although in terms of computational time it is preferable. However, implementing a structured mesh for the nacelle in combination with the blades would require adaptations to the existing code, along with additional testing. Since this was outside the scope of this thesis, it was chosen to use the unstructured mesher. The AircraftFlightStreamMesher in the MMG consists of three sets of controls: a set of general controls, and two sets of controls for the nose and tail regions. The parameters that define the main body are the following:

- **lateral_max_size**: determines the maximum edge size of the triangles in mm.
- **lateral_min_size**: determines the minimum edge size of the triangles in mm.
- **lateral_growth_rate**: determines the maximum growth rate between adjacent edges.

The mesh parameters for the nose and tail face regions are equivalent and are given by:

- **the maximum cell size** at the nose or tail.
- **the minimum cell size** at the nose or tail.
- **the growth rate** of cells at the nose or tail.

In the following section, a study is performed to assess how the mesh parameters for the blades and nacelle affect the forces and moments evaluation of FlightStream.

5.5. Mesh Convergence Study

The discretization of the geometry has an effect on the forces and moments evaluation. Therefore, a study is performed to assess how the mesh parameters have an effect on performance quantities such as the thrust coefficient, power coefficient, and the efficiency. The reference geometry that is used for the study is again the XPROP. However, the number of blades of the propeller has been reduced from 6 to 3. This was done since a combination of 6 blades with 80 chordwise number of points, and a spanwise pitch of 2 mm required more than 32 GB of RAM for the initialization of the solver, which exceeded the memory capacity of the hardware. As mentioned before, there are two sets of parameters for the mesh: one set for the blades and one set for the nacelle. Since the nacelle geometry will remain constant throughout this thesis, only a convergence study was performed for the blades. Table 5.3 lists the mesh parameters that are used for the nacelle. These are obtained after several iterations of adjusting the parameters manually in MMG and then checking in FlightStream whether the topology contains only feature edges and no free or overlapping edges, as shown in Figure 5.14.

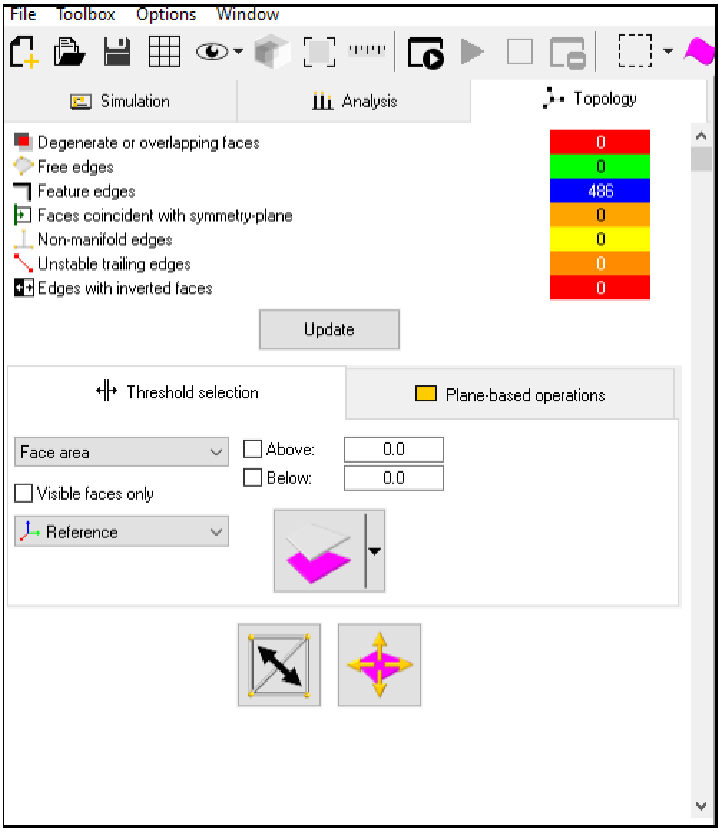

Figure 5.14: Topology Information Tab in FlightStream

For the blades, there are two main control parameters: the number of chordwise points and the spanwise pitch. Four different meshes were generated:

- a coarse mesh
- a fine mesh, with half the cell size of the coarse mesh
- an adaptation of the fine mesh with an increased spanwise pitch,
- and an extra fine mesh with half the cell size of the fine mesh

The four meshes can be seen in Figures 5.15 to 5.18, respectively.

The adapted fine mesh was added to see how fewer cells in the spanwise direction would affect the thrust, power, and efficiency in FlightStream. The mesh parameters of the four meshes can be found in Table 5.4. The operating conditions and FlightStream settings that were used are listed in Table 5.2.

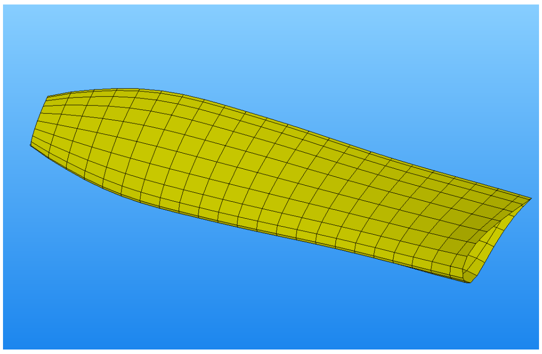

Figure 5.15: The coarse blade mesh

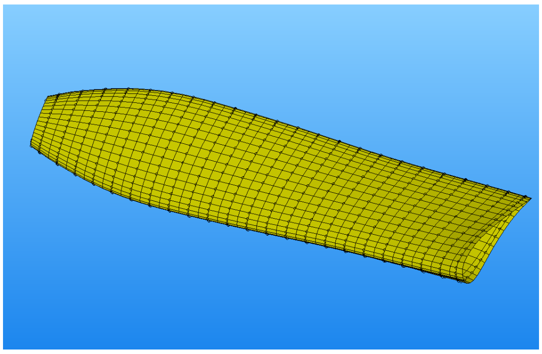

Figure 5.16: Fine blade mesh

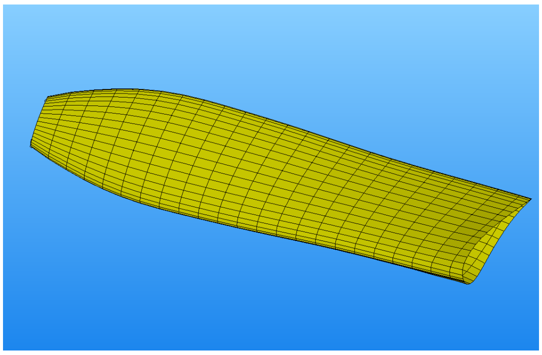

Figure 5.17: Fine mesh with increased spanwise pitch

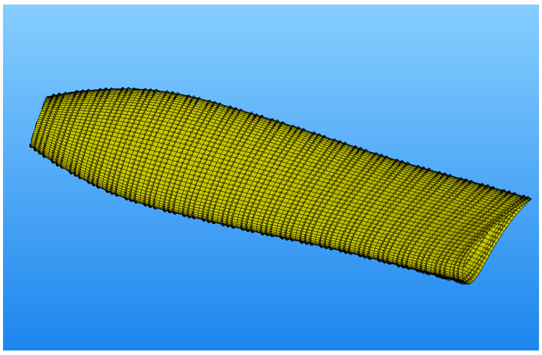

Figure 5.18: Extra fine blade mesh

Table 5.2: Operating conditions and FlightStream settings used in the mesh convergence study

Parameter	Value
Free stream velocity [m/s]	30
Density [kg/m^3]	1.225
Sonic velocity [m/s]	340.29
Viscosity [Pa·s]	$1.79{\cdot}10^{-5}$
Temperature [K]	288.15
Pressure [Pa]	101324
Collective pitch [deg]	30
Angle of attack [deg]	0
Side-slip angle [deg]	0
Solver mode	Steady (rotary)
Lift Model	Vorticity
Drag Model	Vorticity
Moments Model	Vorticity
Reference velocity [m/s]	30
Reference length [m]	0.031
Reference area [m^2]	0.087

Table 5.3: Nacelle Mesh Parameters

Parameter	Value
fuselage lateral control	15.0
lateral max size	12.0
lateral min size	2.0
lateral growth rate	0.5
tail max size	2.0
tail min size	0.5
tail growth rate	0.2
nose max size	1.5
nose min size	0.5
nose growth rate	0.4

Table 5.4: Blade mesh controls of the four meshes

Mesh	Chordwise points [-]	Spanwise pitch [mm]	Nr faces (Parapy)
Coarse	20	8	4,342
Fine v2 (increased spanwise pitch)	40	8	6,268
Fine	40	4	8,907
Extra fine	80	2	26,107

Figure 5.19 shows a comparison of the thrust coefficient against the advance ratio for the four meshes. It can be seen that the curves, in general, lie close to each other. At an advance ratio of 1.4, the delta in c_T is approximately 18% between the coarse mesh and the adapted fine mesh. When keeping the advance ratio constant as in Figure 5.20, it can be seen that the thrust coefficient is not strictly increasing or decreasing. At $J = 0.9$, the delta in c_T is at most 2.6 % between the coarse and the adapted fine mesh. With respect to the power coefficient shown in Figure 5.19, it can be seen

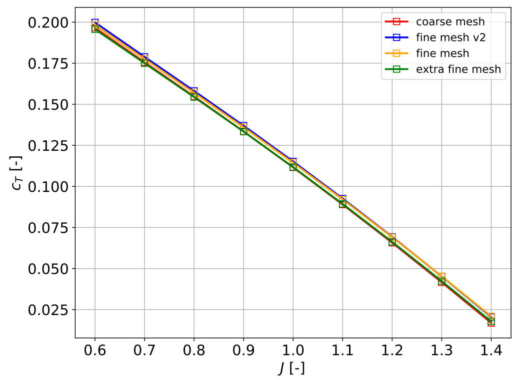

Figure 5.19: c_T versus J for four meshes

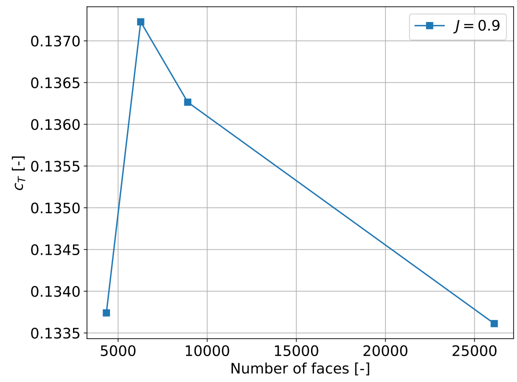

Figure 5.20: c_T versus the number of faces of the mesh at $J = 0.9$

that also here, the curves in general lie close to each other. The maximum difference between the meshes at each advance ratio is computed. At $J = 0.6$ the difference is 0.6 %, while at $J = 1.4$ it is 10 %. Figure 5.22 shows the effect of the mesh size on the thrust coefficient at an advance ratio of 0.9. The coarse mesh, adapted fine mesh, fine mesh, and extra fine mesh are shown from left to right, respectively. It can be seen that the power coefficient is only affected slightly by the first two meshes. Then, after further refinement of the mesh, the thrust decreases. The differences in thrust coefficient are at most 1 % for this advance ratio.

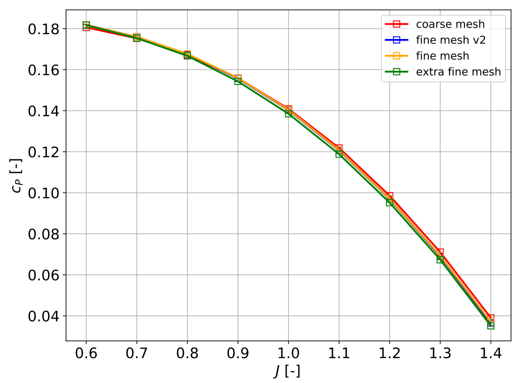

Figure 5.21: c_P versus J for four meshes

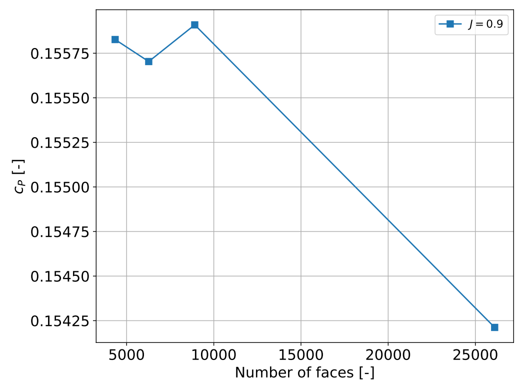

Figure 5.22: c_P versus the number of faces of the mesh at $J = 0.9$

With respect to the efficiency shown in Figure 5.23, differences between the meshes are larger than those seen for the thrust and power coefficient. Also, it can be seen that the differences are relatively larger at a high advance ratio than at a low advance ratio. At $J = 0.7$, the maximum difference between the efficiencies of the meshes is approximately 2%, while at $J = 1.4$, it is 22 %. Figure 5.24 shows a similar pattern as in Figure 5.20. The efficiency initially increases from the coarse to the adapted fine mesh, but decreases when the cell size is further reduced. The difference is at most 2.6 % between the coarse mesh and the adapted fine mesh.

Additionally, the efficiency is plotted against the T_c in Figure 5.25. This is done with the aim to check how the efficiency is affected by the mesh at the thrust requirement that is used in the sensitivity study.

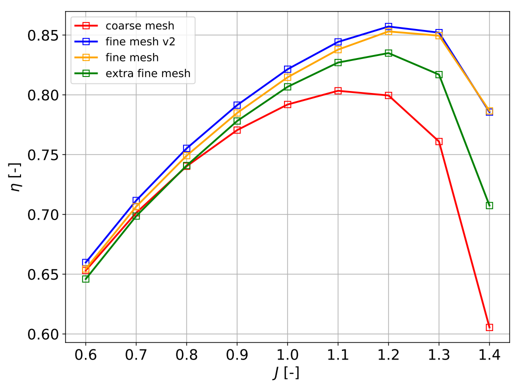

Figure 5.23: η versus J for four meshes

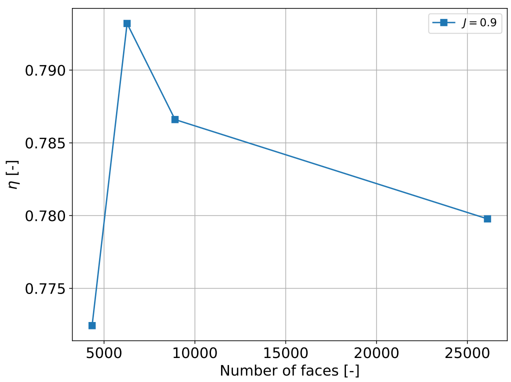

Figure 5.24: η versus the number of faces of the mesh at $J = 0.9$

For more information, the reader is referred to Section 7.2. Figure 5.25 shows an opposite behavior as was seen for the efficiency in Figure 5.23. This behavior is expected since T_c is equal to c_T divided by J to the power of two:

$$T_c = \frac{c_T}{J^2} \tag{5.3}$$

Finally, the efficiency is plotted against the four meshes at a T_c value of 0.0371. The figure shows how the mesh size affects the propeller efficiency with respect to the thrust requirement. Figure 5.26 shows a similar behavior as was shown previously with c_T and η at $J = 0.9$. The values do not strictly increase or decrease as the cell size is reduced, but rather show oscillatory behavior. Nevertheless, the maximum error is 3.2 % in propeller efficiency at the thrust requirement, which is acceptable for this study.

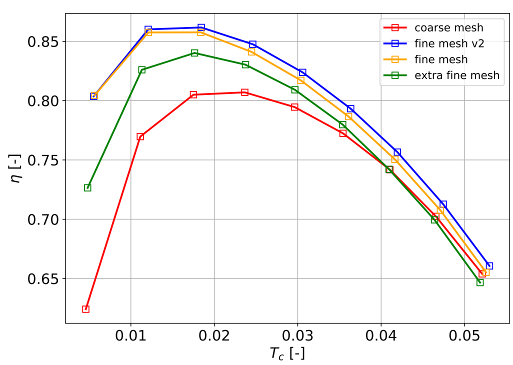

Figure 5.25: η versus T_c for four meshes

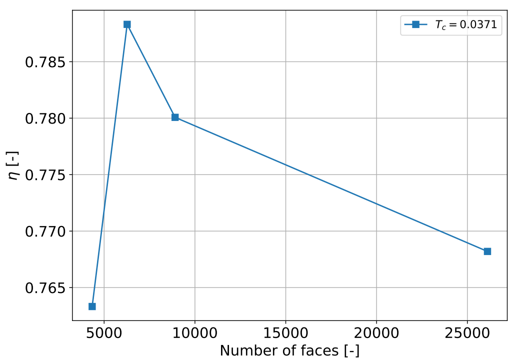

Figure 5.26: η versus the number of faces at the thrust setting used in the sensitivity study ($T_c = 0.0371$)

Besides comparing the numerical accuracy of the meshes, it is important to compare the computational effort of the four meshes, since 1000 different swept blades for three pitch angles at a constant advance ratio are evaluated in this thesis. This is equivalent to 3000 FlightStream steady rotary simulations at one advance ratio. Figure 5.27 shows the average run times in minutes for each mesh in FlightStream. If the adapted fine mesh is ignored in Figure 5.27, it can be seen that the run time increases exponentially as the number of cells is doubled for each refinement. An estimate of the total runtimes for 3000 simulations in FlightStream with each mesh is shown in Table 5.5. The table shows that when performing 3000 simulations with the extra fine mesh, the computational effort becomes unacceptable. However, the computational effort for the coarse, fine, and adapted fine mesh for this thesis is still acceptable. It is chosen to use the adapted fine mesh in the sensitivity study as this has a low computational effort and the error in the propeller efficiency at the thrust requirement with respect to the fine and extra fine meshes are acceptable.

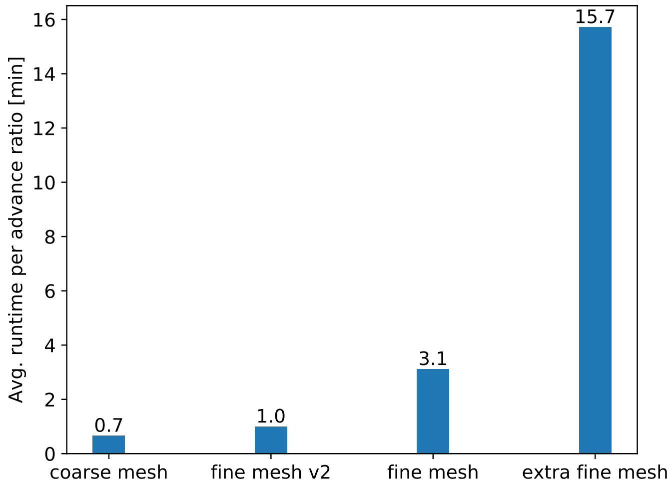

Figure 5.27: Average runtime per advance ratio for each mesh in FlightStream with the steady rotary solver

Table 5.5: Overview of the total computational effort for each mesh for 3000 simulations

mesh	nr faces [-]	avg. time per advance ratio [min]	total runtime for 3000 simulations [days]
coarse	4342	0.7	1.46
adapted fine	6268	1.0	2.08
fine	8907	3.1	6.5
extra fine	26107	15.7	32.7

6
Workflow Implementation

This chapter discusses how the analysis modules described in the previous chapters are implemented into one workflow tool. The tool can be split into three main steps:

1. a geometry generation and discretization step
2. a propeller performance analysis step
3. and a propeller noise analysis step

An overall plan of the tool can be seen in Figure 6.1.

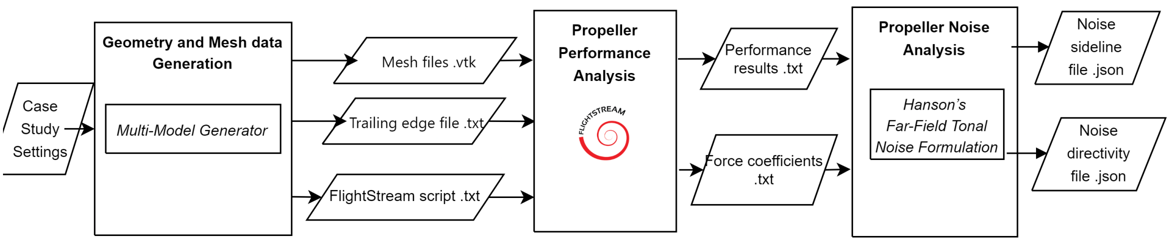

Figure 6.1: Overall Worflow implementation

Before the geometry can be initialized, first the case study inputs and settings must be defined. These relate to the following:

- The number of blade samples N that have to generated. This number will be used to size the number of rows of the Sobol sample set.
- Operating conditions such as: the advance ratio J , the free stream Mach M_x and the air density ρ. In this thesis, the operating conditions were fixed, however the current tool can be simply adapted to account for a changing set of operating conditions if desired.
- A set of constants such as: the number of blades, B and the propeller diameter D.
- Upper and lower bounds of the radial distributions of the design variables such as the twist Tw, sweep or MCA, chord length c and the collective pitch $\beta_{.7R}$.

In the next sections, the three important steps from the tool are discussed.

6.1. Geometry Generation

An overview of the Geometry Generation Process can be seen in Figure 6.2. The geometry generation and discretization process starts by generating the control point data set for the designs. This is done inside the ParaPy Base class "InitPropSettings()". This Class can be used to:

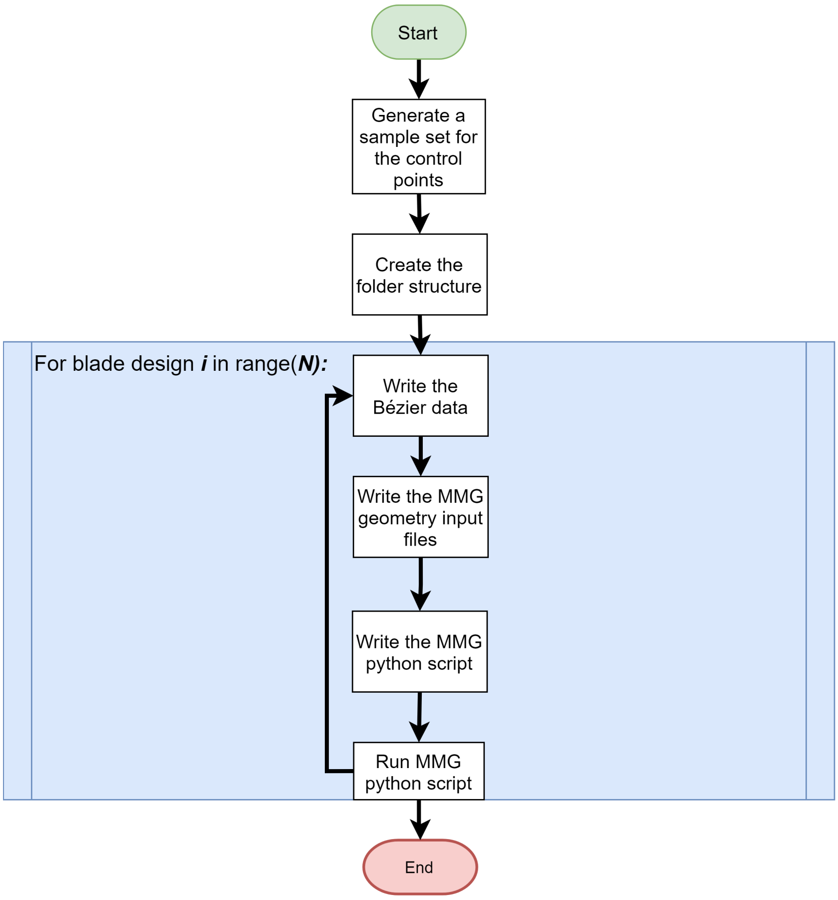

Figure 6.2: Flowchart of the geometry generation process

- Generate the control point values for N designs.
- Generate Bézier curves and retrieve the absolute distributions for the design variables.

The Bézier data and case study settings are then fed into the class "BladeGeometryDOE()". This class is then used to:

- Write a JSON file containing the Bézier control point data.
- Write the rails data to a JSON file.
- and write a Python script. This Python script will:
  1. generate the mesh files of the propeller using *MMG*,
  2. generate a file containing the XYZ-coordinates of the trailing edges of the blades using *MMG*,
  3. generate a file containing the actual mid-chord alignment and face-alignment of a blade design using *MMG*,
  4. generate a script which controls the FlightStream simulation.
  5. add the simulation to a main batch file.

The rails file is needed as an input for MMG, which is executed in the Python script. MMG takes around 30 seconds to generate the mesh files for each blade design, which for N in the order of 10^3 leads to runtimes in the order of hours. Therefore the Python script is run in parallel. After the parallel process is completed, all the files that are necessary to start the Propeller Performance Analysis are generated.

6.2. Propeller Performance Analysis

In the geometry generation a main batch script was created. This batch file contains *N* lines which will run each blade design through FlightStream via a Windows command with the FlightStream script as input. Besides the script, FlightStream also requires two other inputs:

1. Mesh files of the geometry (.vtk format)
2. A file containing the XYZ-coordinates of the trailing edges of the blades (.txt format)

A typical FlightStream script consists of the following steps:

1. Start a new (blank) simulation
2. Import the mesh files
3. Set the fluid properties
4. Import the trailing edges XYZ-coordinates
5. Set the trailing edge wake nodes
6. Specify the solver type
7. Specify the solver settings
8. Specify the free stream conditions
9. Set the solver analysis options
10. Initialize the solver
11. Start the solver
12. Export the solver analysis spreadsheet results as a text file
13. Export the solver analysis force distributions as a text file
14. Export a log of the simulation
15. Close FlightStream

Each of these steps are represented by a set of API commands inside a text file. The file is written after running MMG with the class ”FSWriter()”.

During the simulation two files are generated, which are required for the noise analysis: the solver analysis spreadsheet and the solver analysis force distributions. On the one hand the spreadsheet file will deliver the total thrust and torque of the blades, while the force coefficients file will provide chordwise and spanwise variation of the thrust and torque on the blades. The spreadsheet results will yield force and moments coefficients of the selected coordinate system of any mesh also called ”boundary” in FlightStream. These coefficients will have to be converted to obtain the thrust and torque which are needed for the noise analysis.

6.3. Hanson coefficients from FlightStream force data

Two sets of data are obtained from FlightStream to determine the TSSP for a design:

- The propeller thrust T of 6 blades. As was described in Section 3.2.3 this is obtained from the spreadsheet results, which is evaluated with the vorticity mode. The thrust is used in Equation (4.25) to compute the TSSP.
- The radial blade loading coefficients $c_{f_x}(z)$ and $c_{f_\phi}(z)$. These are given as input into Equation (4.19) of the tonal far-field noise formulation. Figure 6.3 shows the steps that are performed to obtain the coefficients.

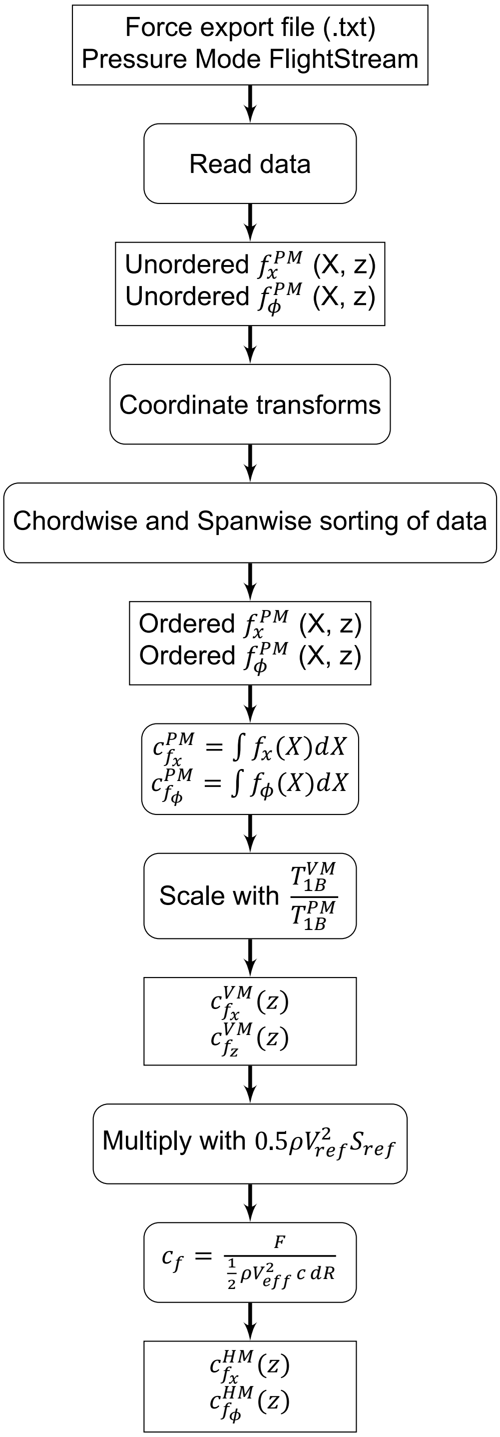

Figure 6.3: Flowchart showing how the Hanson coefficients are obtained from FlightStream force data

It must be noted that the results of the blade planform shown in **??** from the sensitivity study evaluated at $\beta_{.7R_{BSL}}$ and J_{BSL} provide as basis for the discussion in this section. The force data is read from the force export file with the ForceDataReader() class, which is a dedicated ParaPy class written by the author. Since the position of the cells in the data are in absolute coordinates, two coordinate transformations are applied to obtain the force data in chordwise and spanwise coordinates. In the first coordinate transformation, the blade is rotated such that the blade axis is aligned with the positive Y-axis. The coordinate system in FlightStream is defined such that the positive X-axis points in the downstream direction and is the same as the axis shown in the bottom right in Figure 3.9. After the first transformation, the sections are sorted in the radial direction. In the second coordinate transformation, the blade sections are de-twisted and de-pitched, such that the advance direction γ_0 shown in Figure 4.1 coincides with the flight direction, which is the opposite of the downstream direction, which is defined as positive FlightStream. Then, a comparison is made with the original thickness of the airfoils to be able to separate the force data to the pressure and suction side. Finally, the coefficients are sorted in the chordwise direction. Now a complete ordered set of coefficients in chordwise direction for the suction and pressure sides at each radial station is obtained. Then the mean distribution along the chord of the blade is obtained by summation of the two sides. An example of two chordwise force distributions is shown in Figures 6.4 and 6.5.

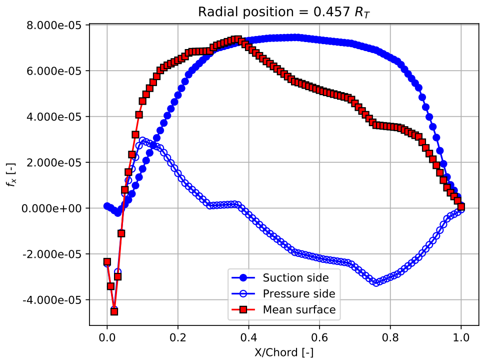

Figure 6.4: Example chordwise distribution of thrust at radial position $r/R_T = 0.457$

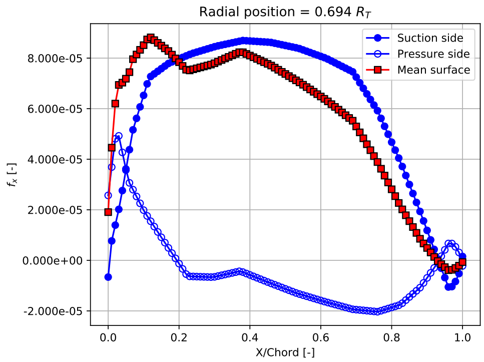

Figure 6.5: Example chordwise distribution of thrust at radial position $r/R_T = 0.694$

After the coordinate transformations and sorting has been applied, an ordered set of force data in chordwise and spanwise direction is obtained. The chordwise distributions are integrated along the chord to obtain the axial and tangential force coefficient per radial station. Figures 6.6 and 6.7 show the radial distributions of axial force of the pressure mode before and after the scaling procedure, respectively. In the figures, the actual spanwise width of the segments is shown. It can be seen that for some segments, the spanwise width is twice as large as the others. A discussion on this will follow in Section 8.5. With respect to the scaling for the example used in this section, the ratio of the thrust of the vortex mode with respect to the pressure mode: T_{1B}^{VM}/T_{1B}^{PM} was equal to 1224. For information about the scaling procedure, the reader is referred to Section 3.2.5. After the scaling is applied, the final step is to multiply the force coefficients with the reference quantities: V_{ref}, S_{ref} to obtain the force and then use **??** to obtain the coefficients for the Hanson Formulation, which are shown in Figure 6.8. In the figure, a sudden drop in loading can be seen at around 60 % radius of the blade. This is a discontinuity that was seen on more designs. The discontinuities are discussed in Section 8.5.

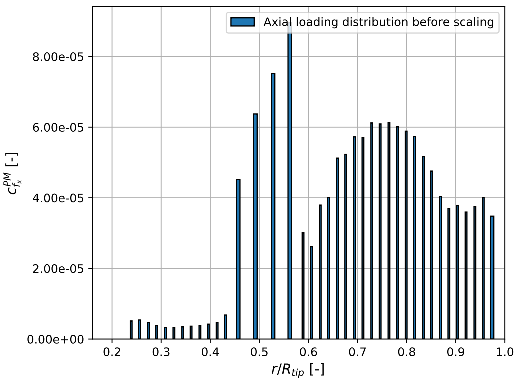

Figure 6.6: Radial distribution of axial loading of Pareto design 3 in sensitivity study before scaling.

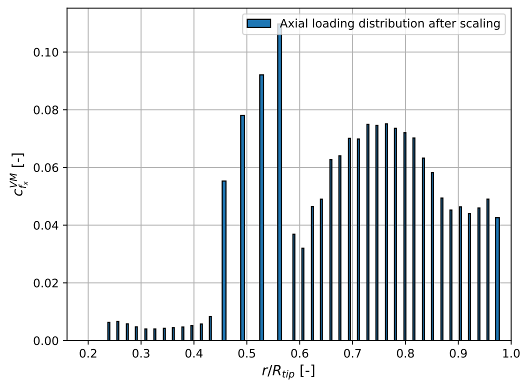

Figure 6.7: Radial distribution of axial loading of of Pareto design 3 in sensitivity study after scaling. Note the different scale on the y-axis with respect to the distribution on the left side

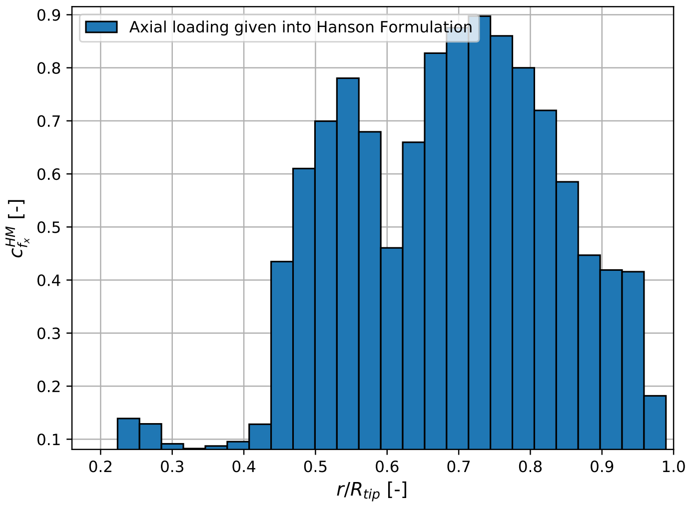

Figure 6.8: Radial distribution of axial loading of Pareto design 3 in sensitivity study as given into the Hanson formulation

III

Sensitivity Study

7 Study Set-up

This chapter covers the set-up of the sensitivity study that is performed between blade sweep and the propeller noise and efficiency. As mentioned in Section 5.2, the design parameters of the propeller which are only considered are blade sweep and the pitch setting. The design space and the physical bounds are described in Section 7.1. The operating conditions and the thrust requirement used to match the thrust of each design are defined in Section 7.2. Then, the thrust matching process is discussed in Section 7.3.

7.1. Design Space Definition

The design space is defined by the design parameters that are studied. In this study, these are sweep and the pitch angle. Sweep is parameterized by the Bézier Curve, resulting in 5 design variables. The pitch setting is varied to match a thrust requirement and therefore is not considered part of the design space. Thus, effectively there are only five design variables relating to sweep. The design variables for sweep are normalized using lower and upper bounds, such that the values for each variable lie between 0 and 1. Although the design variables for sweep control the amount of sweep directly, the sweep bounds are defined such that they dictate the maximum amount of tip sweep. It is chosen to use the same definition for the sweep bounds as those defined in Burger [17], since then the sensitivity results in this study can be compared with respect to Burger. The tip angle of the blade can be maximum 20 degrees measured from the root in a forward or backward direction. The sampling points should be chosen such that maximum information of the relationship between the design variables and the propeller efficiency and noise is obtained, and the design space is filled as effectively as possible. This is done by choosing a suitable Design of Experiments method, which is discussed next.

7.1.1. Design of Experiments Method Selection

The design of experiments (DoE) is the study of how to "select inputs at which to compute the output of (computer) experiments to achieve specific goals" [47]. The topic originated in the context of designing physical experiments [47]. In physical experiments, the outcome of an experiment is not repeatable due to random error [48]. Therefore, the sample points are placed at the extremes of the parameter space in order to account for the contaminating influence of measurement noise. Examples of classical DoE techniques designed for these types of experiments are the central composite design, Box - Behnken design, and full and fractional-factorial design [48]. In contrast to physical experiments, computer experiments are not subject to random error. Therefore, it does not make sense to employ classical DoE techniques, which place the sample points at the extremes of the design space [48]. In order to extract maximum information on the underlying input-response relationship that is studied with computer experiments, the sample points for the design variables should be chosen such that they fill the design space in an optimal sense [48]. This definition agrees with the goal of the sensitivity study. From Kean [48], and Giunta [49], a list of the most well-known DoE methods are summarized:

- **Monte Carlo methods**

  Monte Carlo methods rely on generating random numbers to cover the design space. Typically, they are also referred to as pseudo-Monte Carlo methods to indicate that the algorithm only mimics a process that is truly random [49]. While Monte Carlo methods are relatively easy to implement, a drawback is that due to the points being randomly generated, they often leave large regions of the design space unexplored [48]. This issue can be addressed with an improvement called Stratified Monte Carlo sampling.

- **Stratified Monte Carlo Sampling**

  In Stratified Monte Carlo sampling, each of the n intervals is divided into subintervals or "bins" of equal probability [49]. When the design variables all have a uniform probability distribution, the bins are of equal size. Once the bins are defined, a sample is then randomly placed within each bin. Stratified Monte Carlo sampling provides better overall coverage of the design space compared to MC methods. However, a drawback of this method is that the computation cost rises quickly when the number of samples becomes large.

- **Latin Hypercube Sampling**

  Latin Hypercube sampling (LHS) is also based on dividing the parameter space into bins of equal probability. Under certain assumptions, LHS provides a more accurate estimate of the mean value of the function than with Monte Carlo sampling [49]. Another advantage of the method is that the number of samples can be tailored to the available computational budget [49]. This is because LHS samples are not limited to specific multiples or powers of n, but can be configured with any number of samples. However, LHS suffers from the same flaw as the MC methods, which is that the space-filling characteristics are not guaranteed to be good all the time [48].

- **Minimum Discrepancy Sequences**

  Minimum discrepancy sequences focus on minimizing the discrepancy of the samples, which is defined as a measure of how much the distribution of points deviates from an ideal uniform distribution [48]. Due to their deterministic nature, minimum discrepancy sequences or quasi-Monte Carlo methods can provide more uniformly spaced distributions than pseudo-MC methods [49]. Some examples of minimum discrepancy sequences are the Halton, Faure, and the Sobol sequence. A comparison by Morokoff et al. [50], shows that all sequences seem to experience issues with non-uniformity as the number of dimensions becomes very large. However, this is least severe for the Sobol sequence.

A comparison between the described methods shows that the rate of convergence for quasi-Monte Carlo methods is higher than for pseudo-MC methods [49]. This, together with the added benefit of the flexibility of adding points to the design matrix incrementally, supports the choice for quasi-MC methods. The author prefers the use of the Sobol sequence, as this is shown to perform best out of the mentioned sequences and was also used in the study by Burger [17].

7.1.2. Selecting the Number of Sample Points

The Sobol sequence is the preferred method to generate a uniform space-filling design as it provides more uniformly spaced designs than pseudo-random methods. However, as Keane [48] and Santner [47] point out in their books, minimum discrepancy sequences as the Sobol sequence are only considered space-filling if the number of sample points is increased, as is demonstrated in Figure 7.1.

With ten points, the Sobol sequence does not cover the entire domain of $[0, 1]$, whereas a design with a hundred points results in a more uniformly filled space design. Hence, more sample points than ten are preferred. However, more sample points also mean a higher computational cost. Therefore, a trade-off is performed in terms of the number of sample points that should be used for this study. Three space-filling designs are generated using the Sobol sequence implementation from the UQToolbox package by Daniele Bigoni [1]. This implementation combines the Sobol sequence with a scramble function by Owen [51]. The number of dimensions is set to 5, and the first 1000 numbers of the sequence are skipped. The three space-filling designs are compared based on their uniformity and the run time in FlightStream, which is estimated using an average run time of 1 minute per advance ratio evaluation per pitch setting as mentioned in Section 5.5. Figures 7.2 to 7.4 show the three space-filling designs in the first and second dimension on $[0, 1]$. It can be seen that a hundred points result

[1] https://pypi.org/project/UQToolbox/, Accessed on 12-8-2021

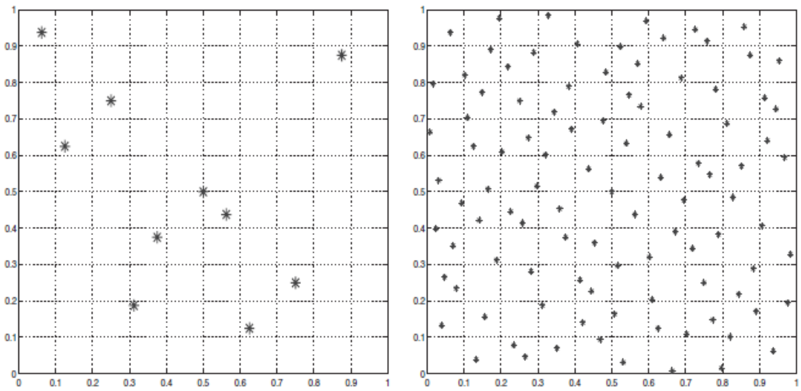

(a) First 10 points of the Sobol sequence (b) First 100 points of the Sobol sequence

Figure 7.1: Comparison of two space-filling designs on $[0, 1]$, from Ref [48]

in a sparse space-filling design in the first two dimensions. Design 2 is already much more densely spaced, while design 3 is very densely filled on the unit interval. The same behavior is also seen when the designs are plotted against other dimensions, as shown in Figures 7.5 to 7.7. Hence, from the figures, it is clear that, in terms of uniformity, it is preferred to use more than a hundred sample points, since a larger portion of the design space is covered, thereby providing more information to analyze the trade-off between the noise and efficiency.

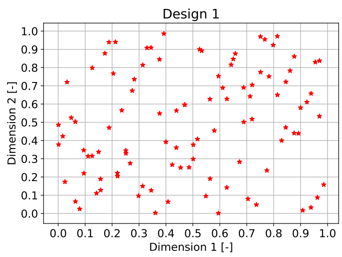

Figure 7.2: Space-filling design 1 in the first and second dimension on $[0, 1]$

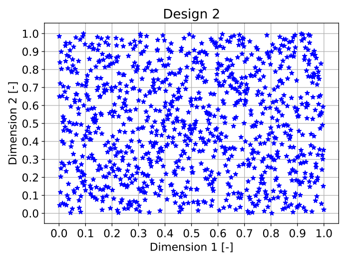

Figure 7.3: Space-filling design 2 in the first and second dimension on $[0, 1]$

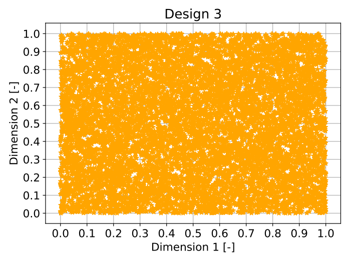

Figure 7.4: Space-filling design 3 in the first and second dimension on $[0, 1]$

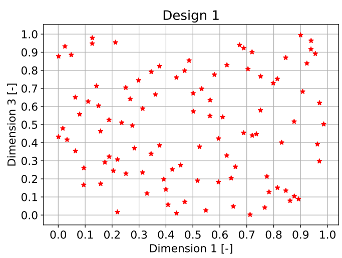

Figure 7.5: Space-filling design 1 in the first and third dimension on $[0, 1]$

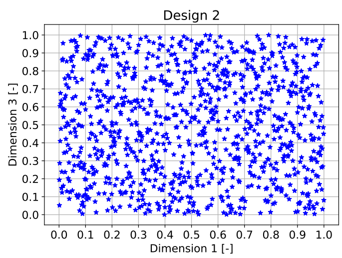

Figure 7.6: Space-filling design 2 in the first and third dimension on $[0, 1]$

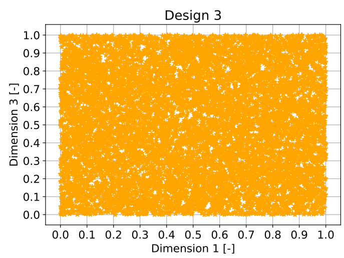

Figure 7.7: Space-filling design 3 in the first and third dimension on $[0, 1]$

Besides the uniformity, the expected computational effort of the three designs is compared. In the Sensitivity study, three pitch angle evaluations will be performed for each design. As mentioned before, it is assumed that a complete simulation in Flightstream for each design for one advance ratio and one pitch setting takes on average, 1 minute. The corresponding run times for the three designs are given in Table 7.1.

Combining the information from the figures and the table, it is clear that the cost for design 1 is

Table 7.1: Expected total runtime with FlightStream for three space-filling designs

Space design	Number of sample points	Total runtime (hours)
Design 1	100	5
Design 2	1000	50
Design 3	10000	500

low, but due to the sparse spreading of the points, this option is not preferred. On the other hand, design 3 yields a very dense design, but the corresponding computational time is considered to be too high. Therefore, Design 2 is used to generate a Design of Experiments (DoE) as this provides a good compromise between uniformity and the computational effort. In the next section, the operating settings and the thrust requirement are discussed.

7.2. Operating Conditions and Thrust Requirement

In the study, the same ambient conditions are used as in the study by Burger [17]. These correspond to those at sea level specified by the international standard atmosphere, and are listed in Table 8.2. As was discussed in Section 3.3, the flow velocity for the remainder of the study is doubled from 30 m/s to 60 m/s to reduce discrepancies due to low Reynolds numbers.

Table 7.2: Operating settings used in the sensitivity study

Property	Value	Unit
Free stream velocity	60	m/s
Air density	1.225	kg/m^3
Altitude	0	m
Static temperature	288.15	K

Besides the properties listed in Table 8.2, another important flow parameter is the advance ratio J, which, combined with the free stream velocity, dictates the rotation speed of the propeller. The advance ratio is kept constant in this study. Thus, the tip Mach number M_t for each design is equal.

The different propeller blade designs should achieve the same thrust if the propeller efficiency and noise are to be compared fairly. Therefore a thrust requirement needs to be defined. It is chosen to use the same thrust condition as from the study by Burger [17]. The ATR72-500 is used as reference aircraft. The properties that are used to determine the thrust coefficient T_c of one propeller are listed in Table 7.3.

Table 7.3: ATR72-500 properties

Property	Value	Unit
Freestream velocity	141.67	m/s
Maximum landing mass	21850	kg
Propeller diameter	3.93	m
Cruise altitude	7620	m
Air density	0.5489	kg/m^3
L/D	17	-

$$T_c = \frac{T}{\rho_\infty V_\infty^2 D^2} \tag{7.1}$$

For the calculation of the T_c it is assumed that the aircraft is in steady, horizontal flight such that lift equals weight ($L = W$), and thrust equals drag ($T = D$). A lift-over-drag ratio of 17 for the aircraft is assumed. Then, combining the properties in Table 7.3 and Equation (7.1), a T_c of 0.0371 for one propeller of the aircraft was determined. The thrust matching process, where the efficiency and noise are obtained for each design satisfying the thrust requirement, is discussed in the next section.

7.3. Thrust matching

This section describes how the efficiency and TSSP matched to the thrust requirement, referred to as η^{TR} and $TSSP^{TR}$ are obtained for each design. There are 5 design variables for sweep, which are denoted by $x_{CP_2}, x_{CP_3}, x_{CP_4}, y_{CP_2}$, and y_{CP_3} respectively. Furthermore, the pitch setting required for each design to meet the thrust requirement $\beta_{.7R}^{TR}$, and the advance ratio J that is kept constant, has to be determined. A general overview of the thrust matching process is shown in Figure 7.8. In the first step, a baseline advance ratio J_{BSL} and baseline pitch setting $\beta_{.7R_{BSL}}$ are determined. This is discussed in Section 7.3.1. Then Section 7.3.2 explains how a lower $\beta_{.7R_{lb}}$ and upper $\beta_{.7R_{ub}}$ pitch angle bound is obtained. Finally, Section 7.3.3 explains how the three pitch setting measurements ($\beta_{.7R_{lb}}, \beta_{.7R_{BSL}}, \beta_{.7R_{ub}}$) are used to estimate $\beta_{.7R}^{TR}$, $\eta^{TR}, TSSP^{TR}$ of each design.

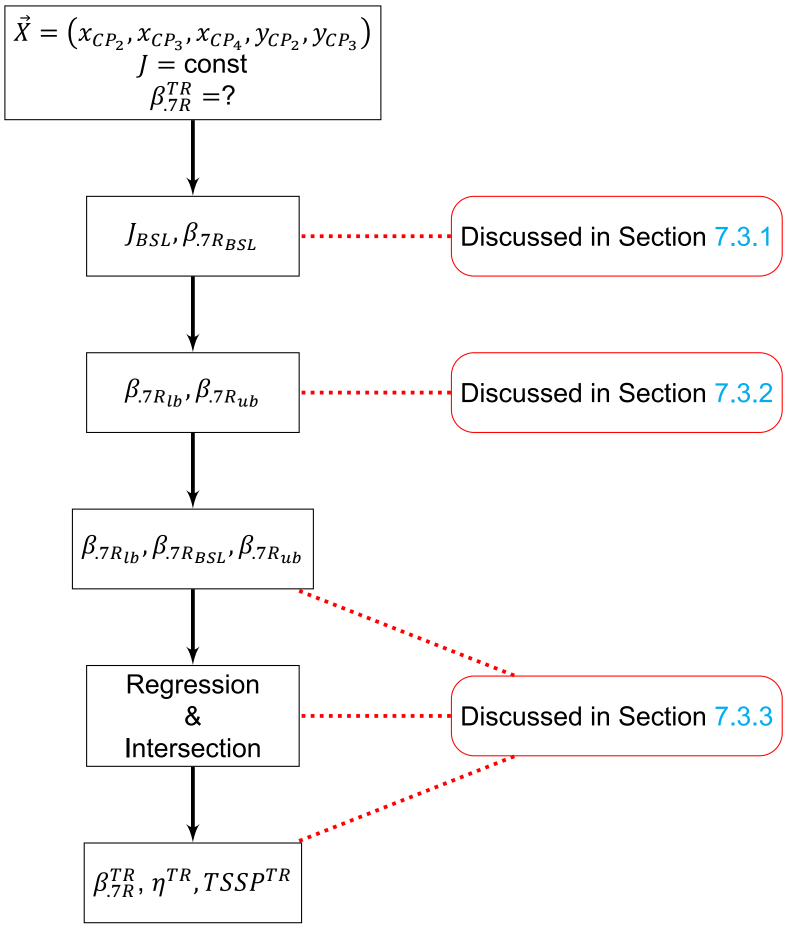

Figure 7.8: General method to obtain η^{TR} and $TSSP^{TR}$ for each design

7.3.1. Baseline advance ratio and pitch setting

The XPROP is used to provide an initial estimate of the advance ratio and pitch setting used in the Design of Experiments. Figure 7.9 shows an overview of steps that are taken.

Figure 7.9: Overview of the process to obtain the baseline advance ratio J_{BSL} and pitch setting $\beta_{.7R_{BSL}}$

Using the operating conditions mentioned in Table 8.2, the reference propeller or XPROP is used to evaluate the c_T, c_P, T_c and η at a combination of J and $\beta_{.7R}$. The settings that were used for FlightStream are the same as listed in Table 3.4. Figures 7.11 to 7.13 show the data that was generated with the

XPROP. The step size for the pitch setting is set to 10 degrees, while the step size for the advance ratio varies with each pitch setting to generate a similar number of data points per pitch setting.

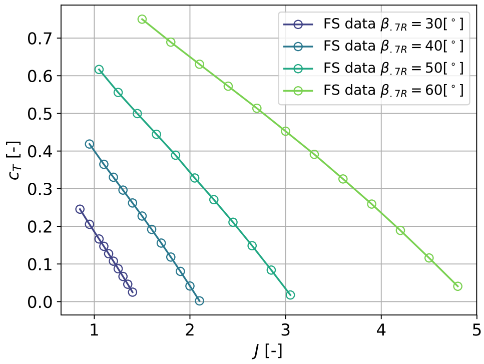

Figure 7.10: c_T versus J of the XPROP evaluated at four pitch settings

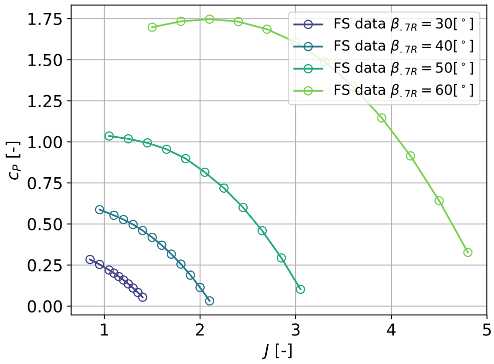

Figure 7.11: c_P versus J of the XPROP evaluated at four pitch settings

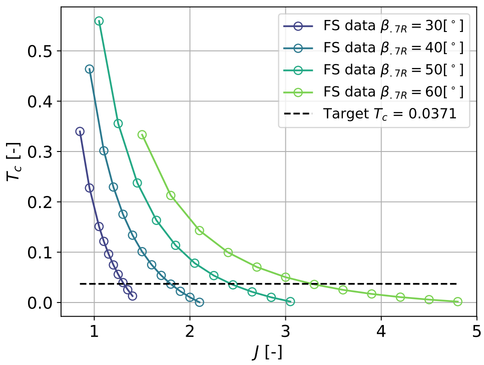

Figure 7.12: T_c versus J of the XPROP evaluated at four pitch settings

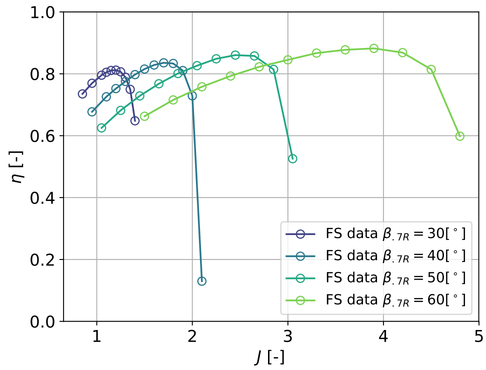

Figure 7.13: η versus J of the XPROP evaluated at four pitch settings

Regression

Linear regression is applied to the input data to obtain approximate functions for the c_T and c_P. The regression function that was used to fit for c_T and c_P is a third-order polynomial of the form:

$$f(\beta_{.7R}, J) = B_0 + B_1\beta_{.7R} + B_2 J + B_3\beta_{.7R}J + B_4\beta_{.7R}^2 + B_5 J^2 + B_6\beta_{.7R}^2 J + B_7\beta_{.7R}J^2 + B_8\beta_{.7R}^3 + B_9 J^3 \tag{7.2}$$

Where $B = [B_0, B_2, \ldots, B_9]^\mathrm{T}$ represents the column vector of unknown coefficients. Then the principle of least-squares minimization is used to obtain the coefficients for c_T and c_P. These can be found in Table 7.4.

Table 7.4: Fitted parameters to the XPROP input data for c_T and c_P using a 3rd order polynomial function

Response variable	B_0	B_1	B_2	B_3	B_4	B_5	B_6	B_7	B_8	B_9
c_T	2.334E-01	-3.691E-01	2.031E-03	4.325E-05	-6.526E-02	3.652E-04	1.437E-03	3.480E-05	-3.259E-03	-2.752E-06
c_P	-6.408E-01	1.004E+00	2.523E-02	-2.922E-02	-6.130E-01	4.908E-06	8.876E-03	3.454E-04	-1.244E-02	1.343E-06

The response functions for T_c and η are obtained by filling the c_T and c_P functions in Equations (7.3) and (7.4).

$$T_c = \frac{T}{\rho V^2 D^2} = \frac{T}{\rho n^2 D^4}\frac{n^2 D^2}{V^2} = \frac{c_T}{J^2} \tag{7.3}$$

$$\eta = \frac{c_T}{c_P} J \tag{7.4}$$

Surface plots were made from the response functions and are shown in Figures 7.14 to 7.17 for the c_T, c_P, T_c and η, respectively. In Figure 7.17, a distinctive line can be identified, with sharp peaks in the positive and negative direction around the line. This line corresponds to the solutions when the response model predicts c_P is zero. If J or $\beta_{.7R}$ is increased beyond this line, then c_P becomes negative. When the data is filtered to show only real values, Figure 7.18 shows the region of efficiency on the side for which c_P and c_T are still positive. The purple shaded region that is shown represents the boundary that was mentioned before.

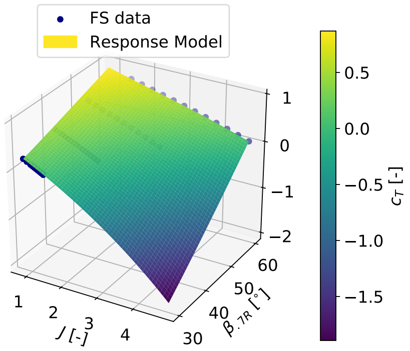

Figure 7.14: c_T data from FlightStream and response model obtained by linear regression

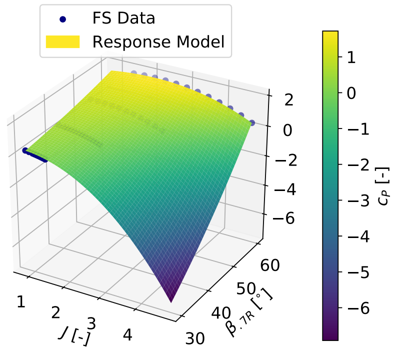

Figure 7.15: c_P data from FlightStream and response model obtained by linear regression

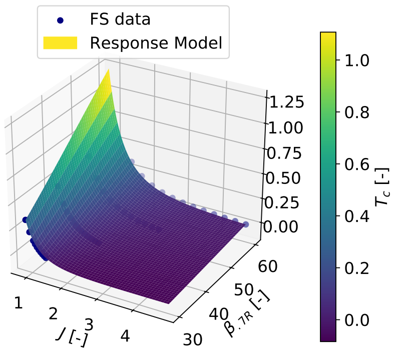

Figure 7.16: T_c data from FlightStream and response model obtained with c_T response model and Equation (7.3)

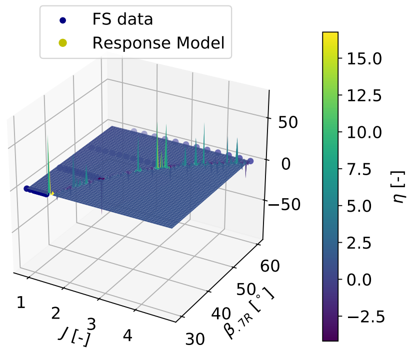

Figure 7.17: η data from FlightStream and response model obtained with c_T and c_P response models and Equation (7.4)

The goodness-of-fit of the response models is assessed by computing the square root of the mean of the residuals between the observations and the predictions, the so-called Root-Mean Square Error (RMSE). The Root-mean-square error can be computed with:

$$RMSE = \sqrt{\frac{1}{N}\sum_{i}^{N} r_i^2} \tag{7.5}$$

Where r_i is the residual between the i-th observation and prediction. Table 7.5 shows the Root-mean square error (RMSE), the mean of the observations (μ_O), the mean of the predictions (μ_P), the standard deviation of the observations (σ_O), and the standard deviation of the predictions (σ_P) for the c_T, c_P, T_c and η, respectively.

The fifth column in Table 7.5, which is the RMSE divided by the mean of the observed values, provides an indication of the magnitude of the residuals for each response. It can be seen that the

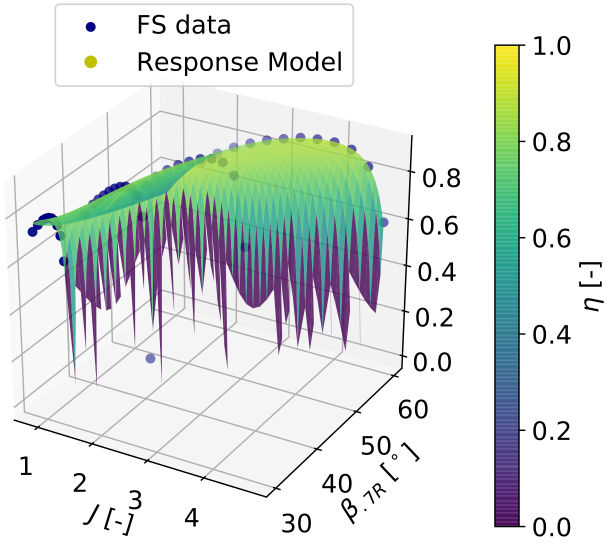

Figure 7.18: η data from FlightStream and Response model showing only realistic efficiencies between 0 and 1

Table 7.5: Root-means square error (RMSE), mean (μ) and standard deviation (σ) of the observations and predictions

Model	RMSE	μ_O	μ_P	RMSE / μ_O	σ_O	σ_P
c_T	0.001094	0.27134	0.27134	0.00403	0.19671	0.19671
c_P	0.00442	0.66556	0.66556	0.006637	0.53777	0.53775
T_c	0.000714	0.11962	0.11961	0.005973	0.12927	0.12906
η	0.03255	0.76158	0.76466	0.042745	0.12250	0.10398

residuals for c_T, c_P and T_c are similar order (10^{-3}), while the residuals for η are one order higher (10^{-2}). Still, the error for η is approximately 4%. This error is acceptable considering that a relatively wide range for the advance ratio ($J = [0.85, 4.95]$) and pitch setting ($\beta_{7R} = [30, 60]$) was used. Thus, the response models are deemed sufficiently accurate to continue for further analysis.

The thrust requirement is applied to the T_c response model by finding the solutions where $T_c = 0.0371$. This gives a subset of J and $\beta_{.7R}$ solutions. These solutions are then filled in the η response model, resulting in Figure 7.19. This line represents the combinations of J and $\beta_{.7R}$ that satisfy the T_c constraint. On the line, the point of maximum efficiency is indicated by the red dot, which is achieved at J = 2.23, and $\beta_{.7R}$ = 47.1 degrees. These values are selected as the baseline advance ratio J_{BSL} and baseline pitch setting $\beta_{.7R}$.

7.3.2. Pitch Bounds Determination

To determine η^{TR}, and $TSSP^{TR}$ for each design, a lower and upper bound pitch value are needed besides $\beta^{TR}_{.7R}$. Figure 7.20 shows how these two extreme values are obtained. First, an initial set of T_c values has to be gathered. This is obtained by evaluating 200 designs at the baseline pitch angle $\beta_{.7R_{BSL}}$. Since the pitch angle at which the design is evaluated is not equal to $\beta^{TR}_{.7R}$, there will be a difference in T_c with respect to the thrust requirement T_c. This delta in T_c, denoted by ΔT^{TR}_c is then converted into a delta in $\beta_{.7R}$ using the following equation:

$$\Delta\beta^{TR}_{.7R} = \Delta T^{TR}_c \cdot \frac{\Delta\beta_{.7R}}{\Delta T_c} \tag{7.6}$$

Solving Equation (7.6) requires two data sources:

1. The difference between the estimated T_c and the T_c of the thrust requirement: $\Delta T^{TR}_c = T_{c_i} - T^{TR}_c$, and
2. the slope of the pitch setting with respect to the thrust coefficient: $\dfrac{\Delta\beta_{.7R}}{\Delta T_c}$.

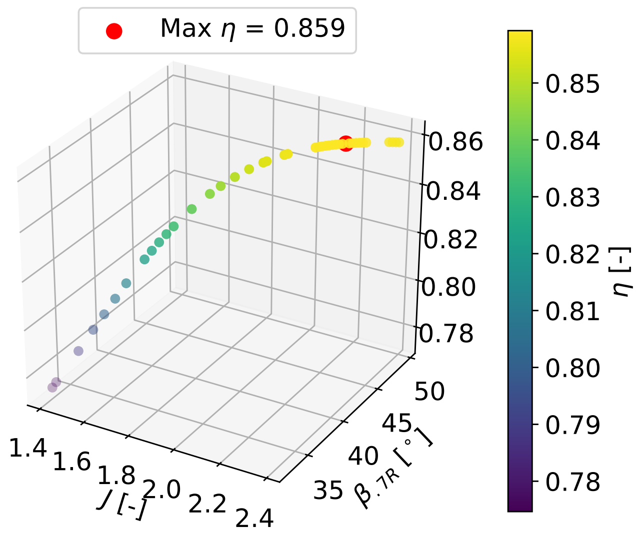

Figure 7.19: η solutions obtained from XPROP reference data for which $T_c = 0.0371$

as mentioned before the first data source is obtained by evaluating 200 designs at $\beta_{.7R_{BSL}}$. Figure 7.21 shows the spread in T_c values of these designs. In addition, the slope of the pitch angle with respect to the T_c is needed to obtain $\Delta\beta_{.7R}^{TR}$. To obtain this slope, five swept blade designs are selected from the sensitivity study and evaluated at 10, 25, 40, and 55 degrees pitch. The blade planforms of these designs can be seen in Figure 7.22. The average slope of the five designs is obtained by regressing the T_c and $\beta_{.7R}$ with a first-order polynomial. The slope of the least-squares solution is then used as an estimate in Equation (7.6).

Figure 7.23 shows the result of the regression for the five designs. The average $\frac{\mathrm{d}\beta_{.7R}}{\mathrm{d}T_c}$ of the 5 designs is 155.9 [deg] / [-]. Multiplying this times ΔT_c^{TR} gives the $\Delta\beta_{.7R}^{TR}$. This operation is repeated for the 200 designs that are evaluated at $\beta_{.7R_{BSL}}$. Then, the $\beta_{.7R}^{TR}$ of the 200 samples is estimated by adding the pitch difference to the baseline pitch as follows:

$$\beta_{.7R}^{TR} = \beta_{.7R_{BSL}} + \Delta\beta_{.7R}^{TR} \tag{7.7}$$

Figure 7.24 shows a bar plot of the different $\beta_{.7R}^{TR}$ from 200 swept designs. This represents an estimate of the pitch angles needed to obtain η^{TR} and $TSSP^{TR}$ for the 1000 designs in the Design of Experiments. As mentioned before, it is preferred to select a wide enough range such that the $\beta_{.7R}^{TR}$ of each design falls inside it. The probability density function of the pitch angles can be approximated by a normal distribution, as shown in Figure 7.25. The mean of the distribution is 47.28 deg, while the standard deviation is 0.54 deg. For a normal distribution, it holds that 99.7 % of the data falls within three standard deviations from the mean. This means that 99.7 % of the pitch values should be accounted for within three standard deviations from the mean. This range is considered sufficient to cover the variation in pitch for the 1000 swept designs. Thus, the lower pitch bound is set to 45.6 deg and the upper pitch bound to 48.9 deg.

7.3.3. Pitch data regression

From the previous sections, three pitch angles were obtained: a baseline pitch angle β_{BSL}, a lower bound $\beta_{.7R_{lb}}$, and an upper bound: $\beta_{.7R_{ub}}$. In the Design of Experiments, the 1000 designs are evaluated at these three pitch settings, resulting in a low T_c, a mid T_c, and a high T_c value. These data are then regressed with a linear function $y = a + bx$, giving a relation between T_c and $\beta_{.7R}$ for each design. This relation is then set equivalent to $T_c = 0.0371$ to find the matching pitch angle $\beta_{.7R}^{TR}$, which is shown in Figure 7.26.

The η and $TSSP$ for the 3 pitch observations are also regressed, but with a second-order polynomial,

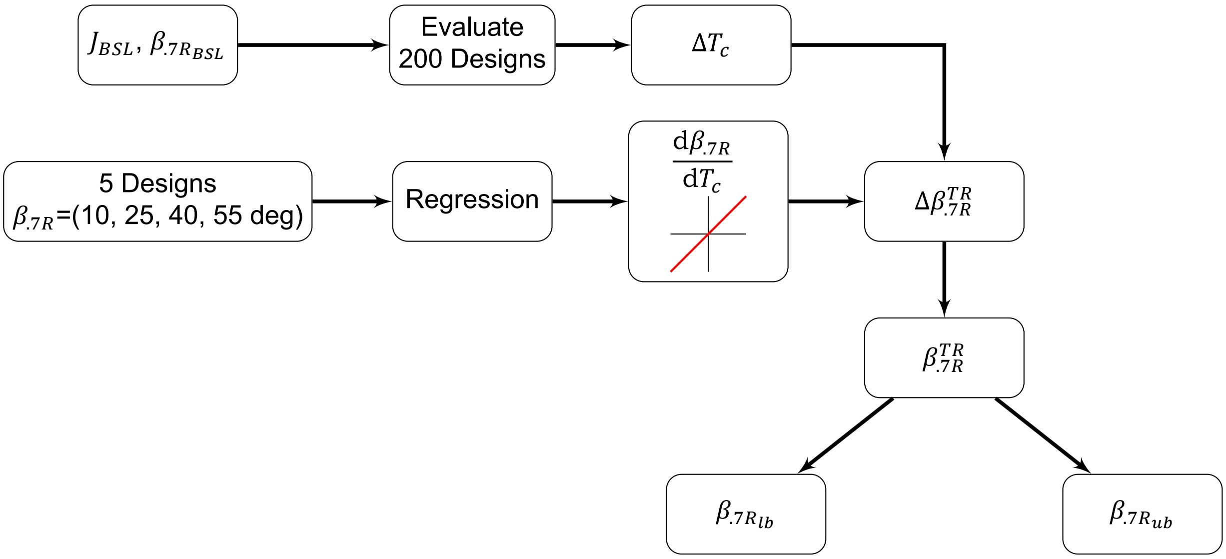

Figure 7.20: Overview of the process to obtain the lower and upper bound for the pitch, $\beta_{.7R_{lb}}$ and $\beta_{.7R_{ub}}$, respectively

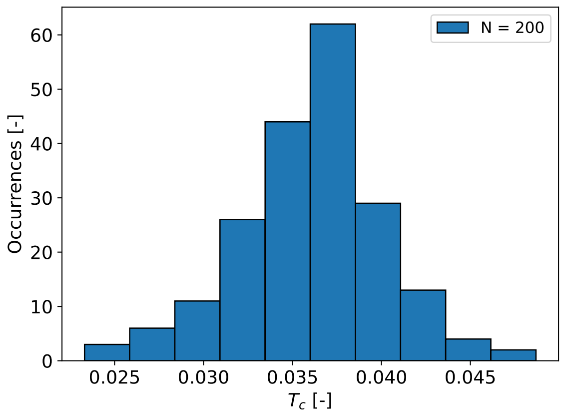

Figure 7.21: Histogram of the T_c values generated from 200 blades from the DoE

as in:

$$y = ax^2 + bx + c$$

Then, by filling in $\beta_{.7R}^{TR}$ in the obtained functions for η and $TSSP$, η^{TR} and $TSSP^{TR}$ are obtained. The pitch range estimate used for the study is verified and discussed in the next chapter.

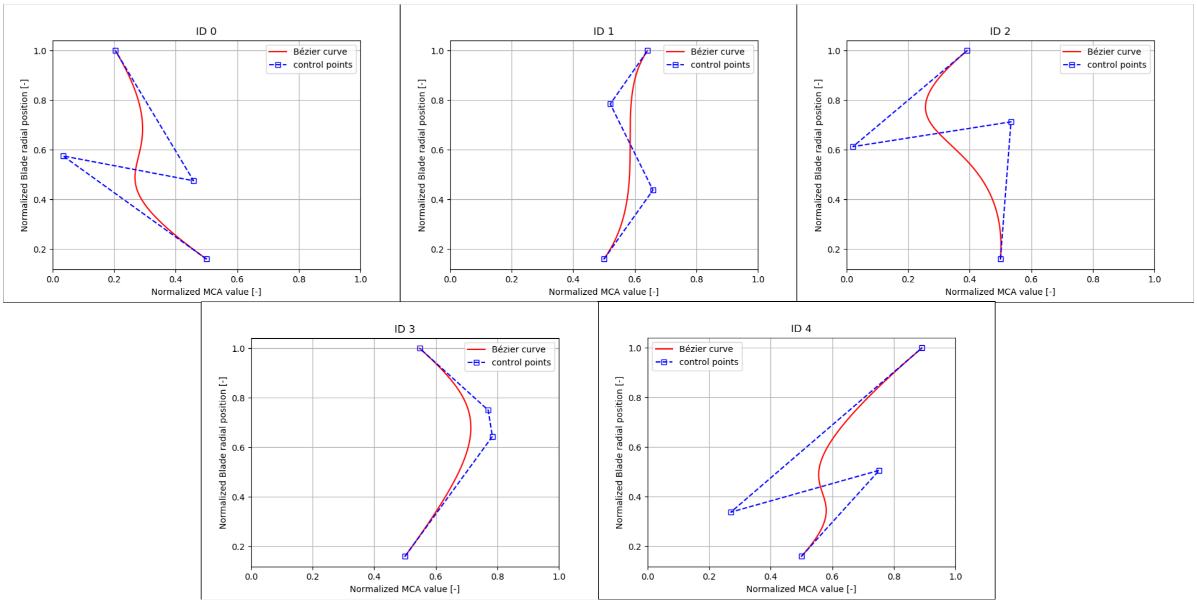

Figure 7.22: Five selected blade designs used to obtain an estimate of the average slope of the thrust coefficient versus pitch angle

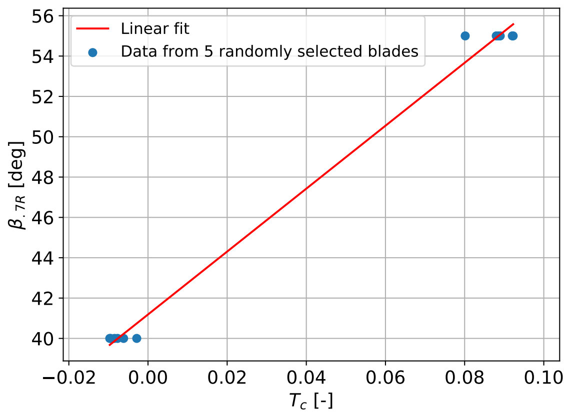

Figure 7.23: Linear regression of T_c and $\beta_{.7R}$ data of 5 blades

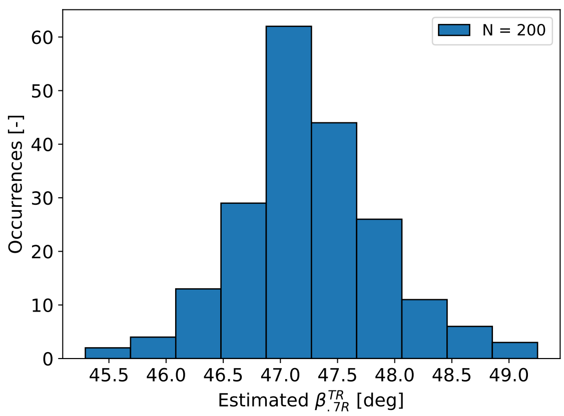

Figure 7.24: Estimated $\beta_{.7R}^{TR}$ by evaluating 200 designs at $\beta_{.7R_{BSL}}$

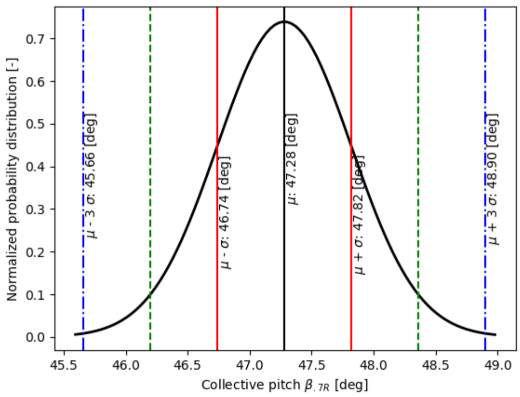

Figure 7.25: Probability density function of the pitch angle variations of the 200 first designs from the DoE

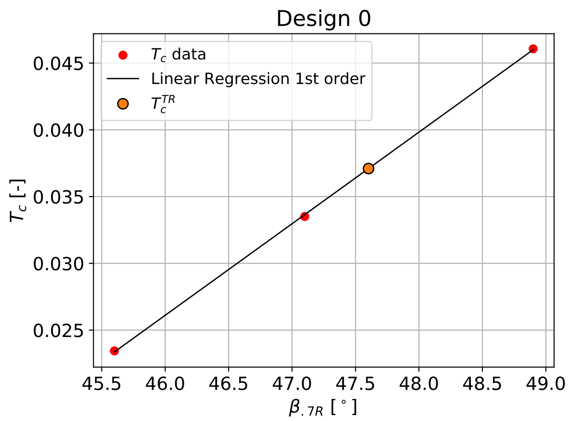

Figure 7.26: Regression of the 3 $\beta_{.7R}$ and intersection with $T_c = 0.0371$ to obtain $\beta_{.7R}^{TR}$

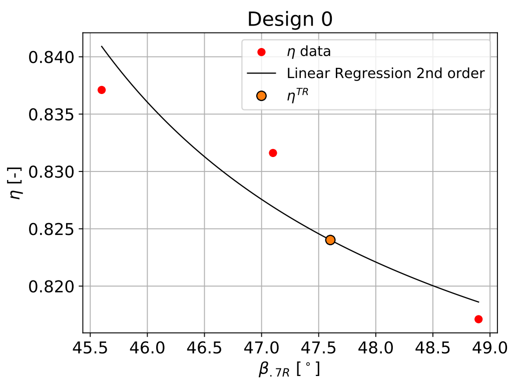

Figure 7.27: Regression of η of one design from the Design of Experiments study

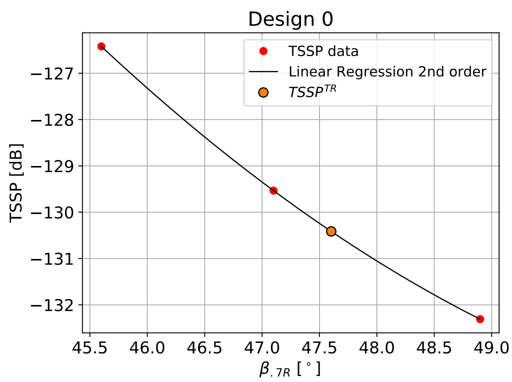

Figure 7.28: Regression of $TSSP$ of one design from the Design of Experiments study

8

Study Results

This chapter discusses the numerical results of this thesis. First, the settings used to obtain the results in Section 8.1. Then, the pitch range obtained in Chapter 7 is verified in Section 8.2. Section 8.3 then compares the results of the three different noise components. In Section 8.4 the general relation of the efficiency versus noise is discussed. Section 8.5 discusses the discontinuities that were found in the radial blade loading distributions. Section 8.6 discusses the effect of sweep on the efficiency and noise. Finally, Section 8.7 discusses an analysis of the Pareto-front.

8.1. Settings

One thousand swept propeller blades have been evaluated at three pitch angles. The details of the machine that was used is listed in Table 8.1. The operating settings that were used are listed in Table 8.2. The settings used for FlightStream can be found in Table 8.3.

Table 8.1: Machine details

Property	Value
Operating OS	Microsoft Windows Server 2019 Data center
Windows version	10
Processor type	Intel Xeon Gold 6148
CPU nr cores	8
Processor speed	2.40 Ghz
RAM	32 GB

Table 8.2: Operating settings used in the sensitivity study

Property	Value	Unit
V_∞	60	m/s
ρ_∞	1.225	kg/m^3
H	0	m
T_s	288.15	K
J	2.23	-
D	0.4064	m
$\beta_{.7R_{lb}}$	45.6	deg
$\beta_{.7R_{BSL}}$	47.1	deg
$\beta_{.7R_{ub}}$	48.9	deg

Table 8.3: FlightStream settings used in the sensitivity study

Property	Value
Version	2020.2
Build	3182021
Lift model	Vorticity
Drag model	Vorticity
Moments model	Vorticity
Solver mode	Steady Rotary
Freestream type	Rotating

From the 1000 designs, 767 had three successful pitch evaluations, which could be used for further analysis. This means that there were in total 2327 successful simulations, resulting in a success ratio of 82 %. This means that 18 % of the simulations failed. The exact cause of the failed simulations is uncertain, as no log file or data was saved from these failures. The 767 successful designs with three pitch evaluations are used as a basis for further discussion in this chapter.

8.2. Pitch Range Verification

A verification of the pitch range derived in Chapter 7 is performed. Table 8.4 lists the mean, standard deviation, and 3σ confidence bounds of the pitch angle at the thrust requirement that was estimated in the study set-up and the interpolated pitch angle obtained from the results. In the table, it can be seen

Table 8.4: Comparison of pitch range of estimate and results obtained from the sensitivity study

	$\beta_{.7R}^{TR}$ [deg]		
Property	Study Set-up	Study Results	Difference
μ	47.26	47.3	0.04
σ	0.54	0.65	0.11
$\mu - 3\sigma$	45.6	45.36	-0.24
$\mu + 3\sigma$	48.9	49.24	0.34

that the difference in the mean pitch angle between the study set-up and results is just 0.04 degrees. However, the standard deviation between the set-up and in the results is increased by 0.11 degrees. Therefore, the confidence bounds for 99.7 % of the pitch angles are 0.24 deg lower and 0.34 deg higher, respectively. In 18 cases of the 767 successful designs, the upper pitch bound $\beta_{.7R_{ub}}$ was exceeded by on average 0.258 deg. For these 18 designs the matching thrust was found by extrapolating outside of this upper bound. Thus, in total 767 designs are used as a basis for further discussion in the results.

8.3. Noise Components Comparison

The individual noise components due to volume, axial loading, and tangential loading are compared. Figures 8.1 to 8.3 show the results of the three components for the 767 designs, respectively. When comparing the components, it can be seen that the thickness component is dominant in the results. This result is striking, since the freestream Mach number used in the study is relatively low. According to literature, thickness noise is expected to be dominant at a high freestream Mach number [23]. As will be discussed in Section 8.5, the axial and tangential loading from FlightStream are wrongly predicted. Therefore, the conclusions that are made in this thesis will only apply to the thickness noise component and not to the loading noise component. The acoustic effects of blade sweep are captured when considering the dominant thickness noise component.

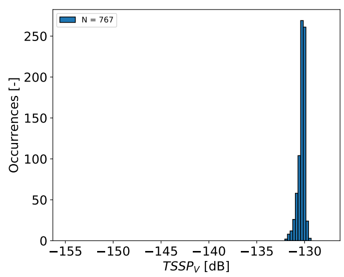

Figure 8.1: Histogram of the thickness noise for the 767 designs

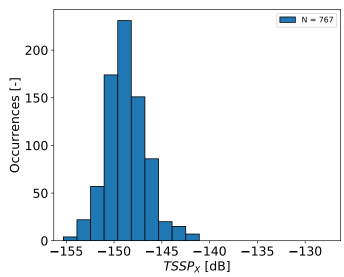

Figure 8.2: Histogram of axial loading noise for the 767 designs

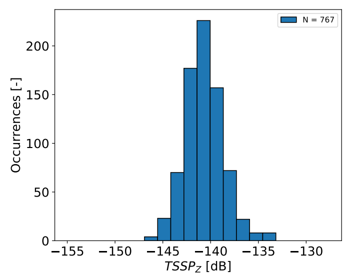

Figure 8.3: Histogram of the tangential loading noise for the 767 designs

8.4. Relation between Efficiency and Noise

The estimates for η^{TR} and $TSSP^{TR}$ for the 767 successful designs are combined into a scatter plot in Figure 8.4. It can be seen that most of the designs achieve a relatively high η and are lumped together into a point cloud. The mean η of the point cloud is approx. 0.85. On the other hand, several designs stand out due to their relatively low η, which are indicated in red. The spread in η for these designs is rather high: approximately 22 %. The three designs with the lowest propeller efficiency are picked and discussed in more detail in Section 8.4.1. Ignoring the low η designs and focusing on the dense region, the difference in η due to sweep is 7.7 %, while the difference in TSSP is 4.4 dB. Although it is difficult to get a feeling of what the values for TSSP mean in terms of the loudness, due to the comparison at constant thrust, a difference in TSSP is actually the same as a difference in Sound Pressure Level (SPL) [17]. In Table 8.5 it is summarized how a difference in SPL is perceived subjectively. According to the table, a difference of 4 dB in SPL sits in between the subjective effect of being ”just perceptible” and ”clearly noticeable”. This means that the impact of sweep on the thickness noise at constant advance ratio is noticeable.

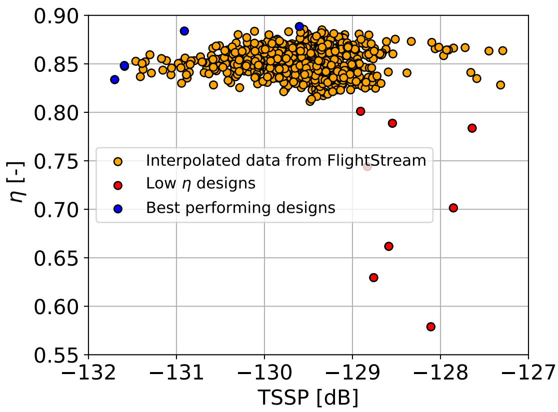

Figure 8.4: Scatter plot of the relation between η and $TSSP$ matched to a thrust constraint at constant advance ratio.

Table 8.5: Subjective effect of a change in sound pressure level [a]

Sound awareness	Change in Sound Pressure Level (dB)
Insignificant	1
Just perceptible	3
Clearly noticeable	5
Twice or half as loud	10
Significant	15
Much louder or quieter, four times as loud	20

[a]Reference: `https://www.engineeringtoolbox.com/sound-pressure-d_939.html` accessed on 12-5-2021

8.4.1. Low efficiency designs

Figures 8.5 to 8.7 show the three designs which achieve the lowest efficiency. When comparing the designs, it can be noticed that all three designs feature a relatively low amount of sweep, although the maximum amount of sweep is highest for design 1. Distinct for design 1 is that the sweep angle changes direction twice: at approximately 20 % radius and around 80 % radius. Design 2 has a similar MCA distribution as design 1, but the maximum MCA is lower compared to design 1. This reduced MCA distribution might explain the higher propeller efficiency. Plots of the radial distributions of axial and tangential loading would shed light on this. However, the radial distributions cannot be compared, since the thrust levels of the designs are not equivalent. Furthermore, it is interesting to note that all three designs feature a slightly forward swept tip. Overall, design 3 features less variation in sweep than designs 1 and 2. In the next section, the designs with the best acoustic and aerodynamic performance are discussed.

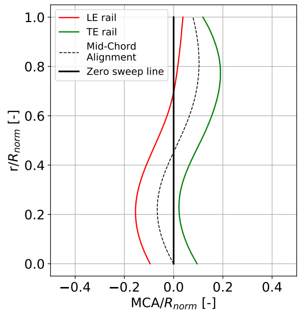

Figure 8.5: Blade planform of low efficiency design 1 without twist and sweep in the OXY-plane

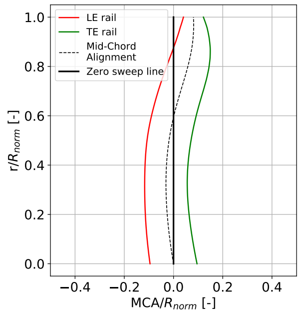

Figure 8.6: Blade planform of low efficiency design 2 without twist and sweep in the OXY-plane

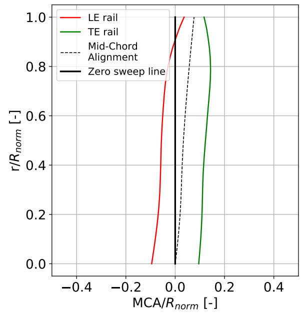

Figure 8.7: Blade planform of low efficiency design 3 without twist and sweep in the OXY-plane

8.4.2. Best performing designs

A scatter plot of the efficiency versus noise of the designs which achieve the best aerodynamic and acoustic performance of the results is shown in Figure 8.8. The designs are numbered from 1 to 4, where design 1 achieves the lowest noise, while design 4 achieves the highest efficiency. The spread in propeller efficiency of the four designs is roughly 5.5 %, while the spread in TSSP is 2 dB. The blade planforms of the four designs are shown in Figures 8.9 to 8.12, respectively. Figure 8.9 shows the blade that achieves minimum noise. The propeller blade starts with forward sweep, but around 50 % of the radius sweep changes sign from positive to negative. Design 2 has a slightly higher efficiency, but also more noise than design 1. The design is quite similar to design 1. However, there are two differences. First of all, the gradient in blade sweep along the blade is more constant than for design 1, and second, the mid-chord alignment at 50 % radius is higher than for design 1. Design 3 also starts with a forward swept root and ends with a backward swept tip segment, similar to designs 1 and 2. However, it can be seen that the location where sweep changes sign, moves from approximately 50 % to 70 % of the blade radius. The implication of moving the point of sweep inversion outboard is significant: the efficiency is increased by 3.55 %. On the other hand, the increase in noise is less than 1 dB. In contrast to the previous designs, the design which achieves maximum efficiency has relatively little amount of sweep across the blade. Also, in the figure, it can be seen that the location of maximum sweep has moved further outboard to roughly 80 % of the radius. The reduction in sweep from design 3 to 4 results in an 0.46 % increase in propeller efficiency but comes with a relatively large noise penalty: 1.3 dB.

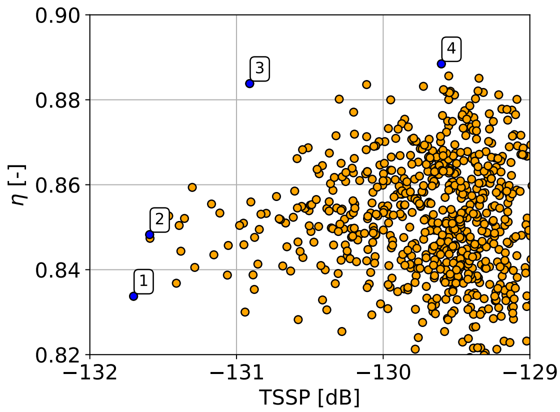

Figure 8.8: Scatter plot of efficiency versus noise focusing on the best performing designs

The loading distributions for Designs 1 to 4 are shown in Figures 8.13 to 8.16. The axial loading is indicated in red, while the tangential loading is indicated in green. It can be seen that the axial loading

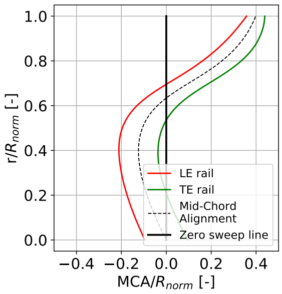

Figure 8.9: Best performing design 1 planform without twist and sweep in the OXY-plane

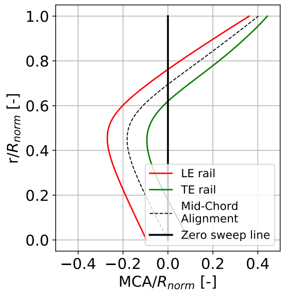

Figure 8.10: Best performing design 2 planform without twist and sweep in the OXY-plane

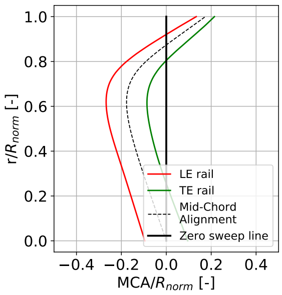

Figure 8.11: Best performing design 3 planform without twist and sweep in the OXY-plane

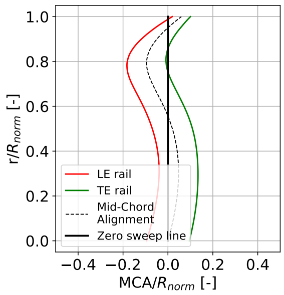

Figure 8.12: Best performing design 4 planform without twist and sweep in the OXY-plane

is the dominating loading on the blade. However, striking in the figures are the sudden losses of thrust on portions of the blade radius. These discontinuities are seen across all designs in the results. In the next section, the cause of the discontinuities is discussed.

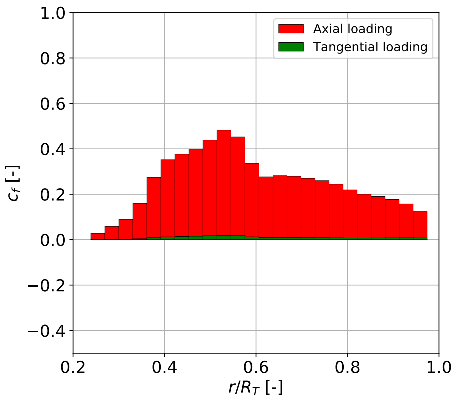

Figure 8.13: Radial loading distribution of best design 1 at $\beta_{.7R_{BSL}}$

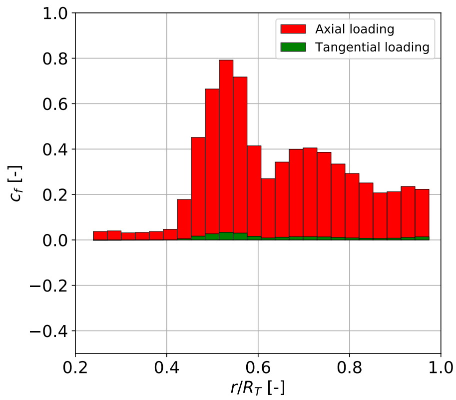

Figure 8.14: Radial loading distribution of best design 2 at $\beta_{.7R_{BSL}}$

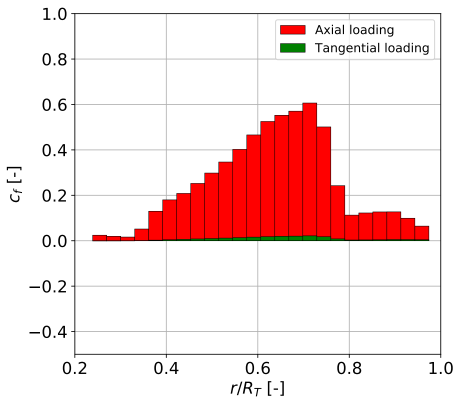

Figure 8.15: Radial loading distribution of best design 3 at $\beta_{.7R_{BSL}}$

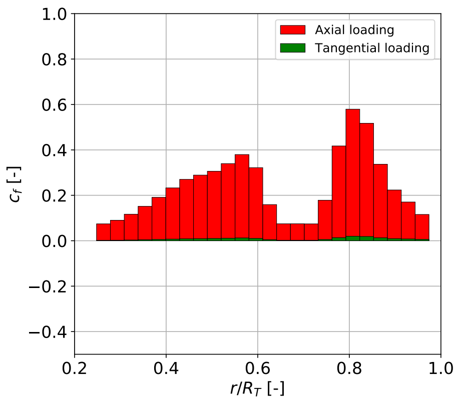

Figure 8.16: Radial loading distribution of best design 4 at $\beta_{.7R_{BSL}}$

8.5. Discontinuities in the Radial Blade Loading Distribution

Besides the discrepancy found between the two modes, discontinuities were seen in the radial distributions, see Figures 8.13 to 8.16. Furthermore, in Figure 6.8 it could be noticed that the spanwise width of several segments is twice as large as others. Why this happens is related to the way the Multi-Model Generator discretizes the topology. As mentioned in Section 5.4, if the ratio of the edge length to the spanwise pitch is larger than 1, the spanwise width of the mesh will be equal to the spanwise mesh of the topology. However, if the ratio is smaller than 1, the section will be split up into two or more spanwise segments. Due to the application of sweep, the edge lengths of the blade can vary. However, the spanwise pitch for each design was not adjusted in the sensitivity study to account for the change in edge size, but instead a constant spanwise pitch of 7.5 mm was used. Thus, depending on the sweep distribution some radial stations, as shown in Figure 8.17 have a different spanwise segment width. This means that the spanwise segment width of the mesh of the blades in this thesis is not constant.

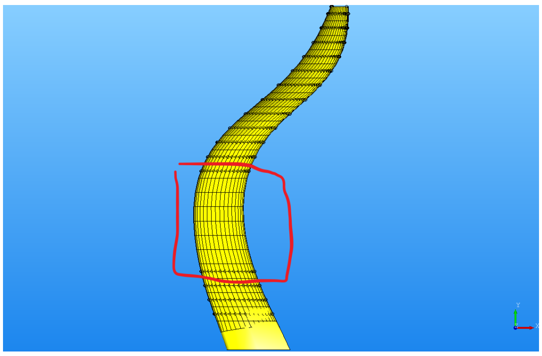

Figure 8.17: Blade topology (yellow) and mesh (black) of Pareto design 1 in the sensitivity study with 7.5 mm spanwise pitch

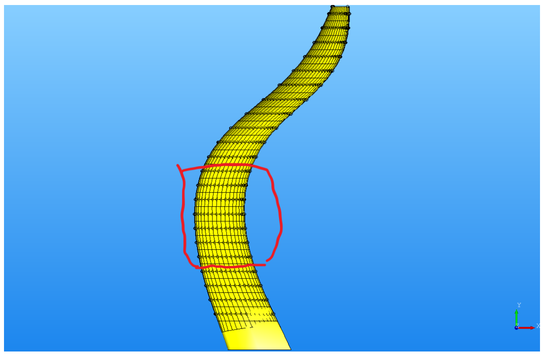

Figure 8.18: Blade topology (yellow) and mesh (black) of Pareto design 1 in the sensitivity study with 7.0 mm spanwise pitch

It is suspected that this non-uniformity in the spanwise direction is related to the discontinuities that are observed in the radial blade loading distributions. The four Pareto designs shown in Figures 8.13 to 8.16 are evaluated with a uniform spanwise mesh to see if a varying spanwise pitch affects the radial blade loading distributions. The spanwise pitch for each design is reduced from 7.5 to 7.0 mm, which results in constant spanwise width as shown in Figure 8.18 Furthermore, the four designs are evaluated using the interpolated pitch angle, such that the thrust setting of the designs is approximately equal. In Table 8.6 the propeller efficiency, TSSP, pitch angle, and T_c values of the four designs with a constant segment width can be seen. In the table, it can be seen that the thrust levels of designs 1,2, and 4 are comparable and within 10 % of the target thrust. However, it can be seen that the thrust, as well as the TSSP and η of design 3, differ significantly. The result is surprising since the pitch angle of

Table 8.6: Details of the pareto designs evaluated at the interpolated pitch angle

Design	TSSP [dB]	η [-]	$\beta_{.7R}^{TR}$ [deg]	T_c [-]
1	-128.8	0.8432	47.16	0.0402
2	-129.2	0.8461	45.81	0.0376
3	-120.9	0.6149	46.76	0.0785
4	-128.1	0.8923	47.27	0.0383

the design is comparable. Also, the sweep distribution shown in Figure 8.11 does not show anything unusual or different compared to the other designs. The blade was re-evaluated in FlightStream to verify the result. However, this produced the same result. Despite the outlier of design 3, Figure 8.19 shows that the radial blade loading distributions have become more smooth. This shows that a change in spanwise segment width of the mesh has an effect on the radial blade loading distributions predicted by FlightStream.

In the sensitivity study the varying spanwise segment width was accounted for in the Hanson frequency formulation, as shown in Equation (4.16). However. as could be seen in Figures 8.13 to 8.16 there are discontinuities in the radial blade loading distributions. As a result, the loading noise in the results is incorrectly predicted. Therefore, only the acoustic effects of sweep on the thickness noise are captured in this thesis. In the remainder of this chapter, the results that are shown are obtained with the same spanwise pitch that was used to obtain the results shown before this section, which means that the mesh of the blade is non-uniform in spanwise direction.

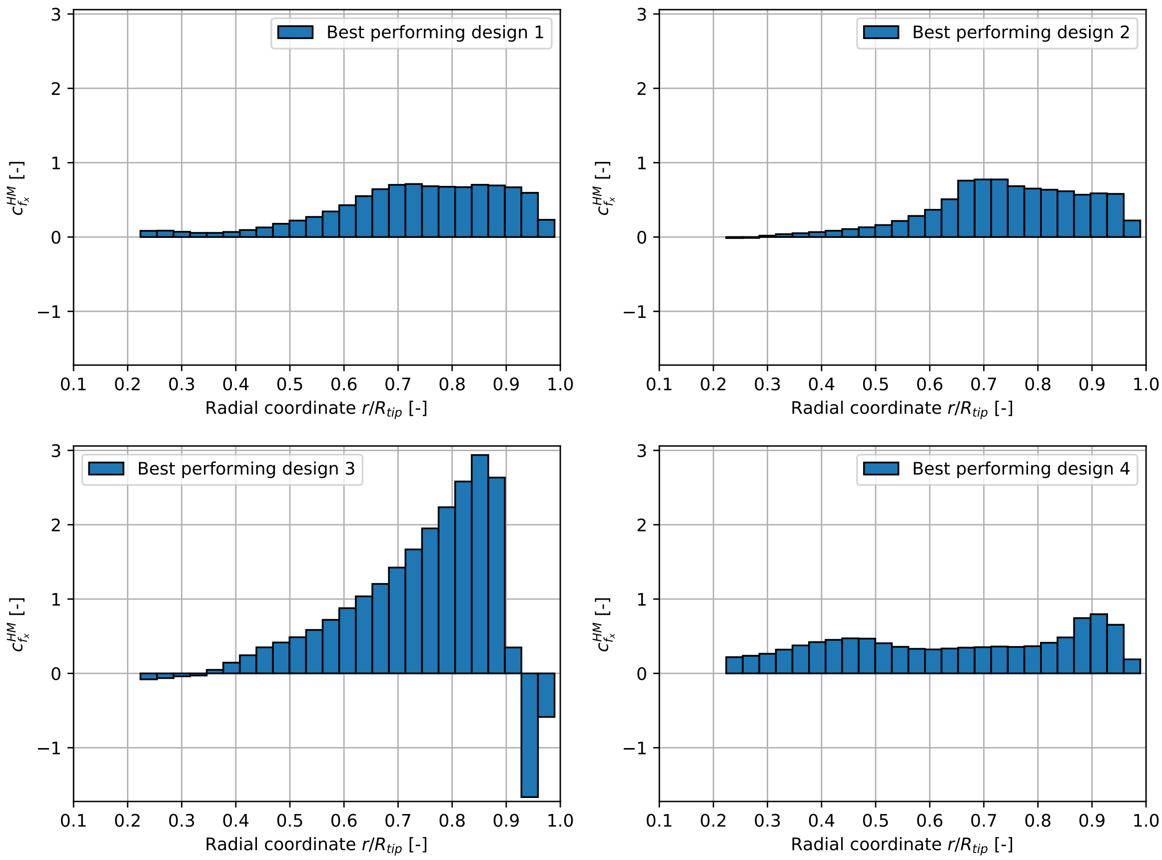

Figure 8.19: Radial axial distributions of the four Pareto designs evaluated at $\beta_{.7R}^{TR}$ and with a constant segment width in the mesh

8.6. Effect of sweep on efficiency and noise

The effect of sweep on the efficiency and noise has been investigated. The blade has been split into three segments with equal radial length, as shown in Figure 8.20. For each blade, the gradients along the MCA distribution are computed. The sweep angle is then determined with Equation (5.1). Then, the average of the angles is taken for each respective radial segment. An example of this is shown in Figure 8.20. A positive sweep angle is defined as a backward sweep, while a negative angle is defined as a forward sweep. Figures 8.21 to 8.23 show the variation of efficiency with the root, mid, and tip sweep angles, respectively.

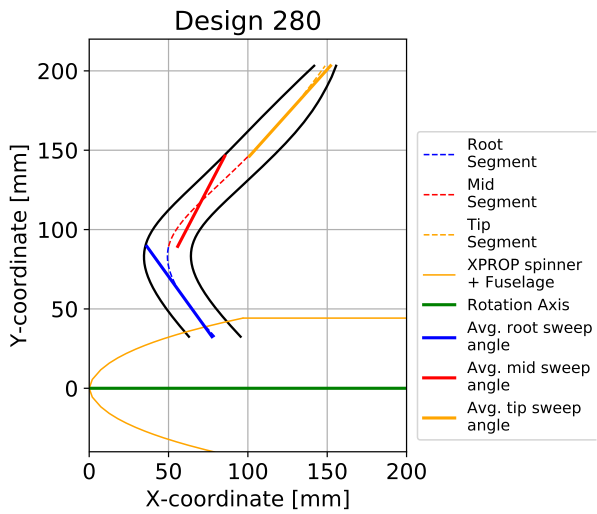

Figure 8.20: Example showing the 3 sweep segments of a blade including the average sweep angles. The Fuselage geometry is added for reference.

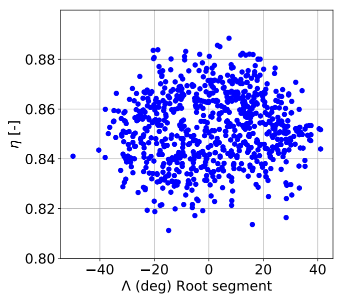

Figure 8.21: Scatter plot of efficiency versus the sweep angle of the Root segment

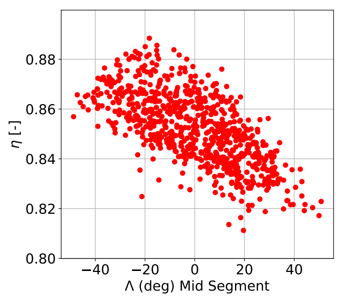

Figure 8.22: Scatter plot of efficiency versus the sweep angle of the mid segment

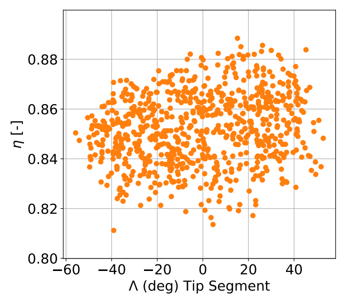

Figure 8.23: Scatter plot of efficiency versus the sweep angle of the tip segment

For the root segment shown in Figure 8.21, no distinct relation between sweep and efficiency is seen. High efficiencies are obtained at -20 and +8 degrees sweep. The design which achieves the highest efficiency has a backward sweep of 8 degrees. For the mid segment, a clear trend can be recognized between sweep and efficiency: a higher forward sweep is more favorable in terms of efficiency. The design with the highest efficiency is obtained at -20 degrees sweep. For higher forward sweep angles sweep, however, the efficiency degrades. For the tip segment, an opposite trend can be seen with respect to the mid segment. Here, higher efficiencies are seen for designs with a higher backward sweep. The highest efficiency is obtained for approximately +18 degrees sweep. The results indicate that a blade with an unswept root segment, a forward swept mid segment, and a backward swept tip is most preferred in terms of efficiency. A forward swept root segment is preferred, as this can lead to a favorable radial loading distribution, which was mentioned already by Burger [17]. When comparing the results of sweep on efficiency with those from Burger, it can be noticed that similarities

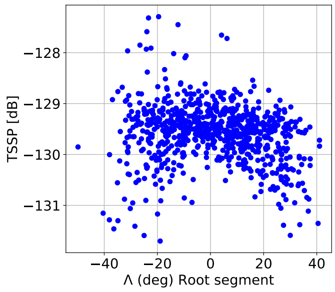

Figure 8.24: Scatter plot of the noise versus sweep angle for the root segment

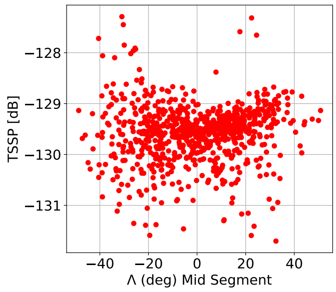

Figure 8.25: Scatter plot of the noise versus sweep angle for the mid segment

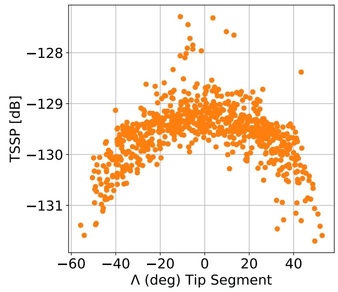

Figure 8.26: Scatter plot of the noise versus sweep angle for the tip segment

are found between the two studies for the mid and tip segments. However, in terms of the root segment, a difference is seen with respect to the root segment. In Burger, it was found that a forward swept root segment is favorable for efficiency [17]. In contrast, in this study no clear trend with respect to sweep and efficiency. In Burger three control points were used in the parameterization, which means that only banana-shaped or straight blades can be generated [17]. Therefore, the local variation in sweep is limited. Since four control points are used in this study, more local variation in sweep allowed. This can explain why a different result is seen for the root segment with respect to the efficiency.

In a similar fashion, the TSSP has been plotted against the sweep angles, shown in Figures 8.24 to 8.26. For the root segment, a distinct trend can be distinguished. Low noise designs are obtained at -30 and +30 degrees sweep. The design with the lowest noise is obtained at 30 degrees forward sweep. For the mid segment, the same trend can be seen: designs with lower noise are obtained for negative and positive sweep angles. The designs of minimum noise are achieved at lower angles than for the root segment. The lowest noise for the mid segment is achieved at 20 degrees backward sweep. For the tip segment, a clear trend can be seen: high sweep angles lead to lower noise. Low noise designs for this segment are achieved around -50 and 50 degrees sweep, while the design with minimum noise is obtained at approximately 55 degrees backward sweep. The results indicate that applying any sweep on each of the segments will result in lower noise. A higher sweep angle means a greater variation of sweep for that segment. The phase delay is proportional to the amount of (normalized) mid-chord alignment [25]. This means if by increasing sweep the amount of potential phase delay is increased. However, as mentioned before in Section 2.2.3, the total amount of noise reduction depends on the relative phase between the radial stations of the propeller blade [25].

8.7. Pareto-front

The objective of this study is to quantify the trade-off between noise and efficiency. The Pareto front is the trade-off between two or more quantities, where an improvement of the performance of one quantity cannot be achieved without a reduction of another. This is represented by the designs which are marked in Figure 8.8. Table 8.7 lists the η and TSSP of the designs. A relation for the Pareto front was found by using the curve fitting toolbox in MATLAB, which is based on a non-linear least-squares method. Several function types were fitted to the data:

- an error function,
- an exponential function,
- a smoothing spline,
- and a power-law function.

Ultimately, the power law function with three terms yielded the best fit. The Power law function equation that was used for the fit is given by:

$$a \cdot x^b + c \tag{8.1}$$

Where the three constants of the solution are:

$$a = 2.0590 \cdot 10^{10}$$

Table 8.7: Pareto front design data

Design	η [-]	TSSP [dB]
1	0.8337	-131.7
2	0.8483	-131.6
3	0.8838	-130.9
4	0.8885	-129.6

$$b = 194.75$$

$$c = -131.65$$

The resulting fit can be seen in Figure 8.27. From the figure, a distinct trend can be noticed for the trade-off between aerodynamic and acoustic performance due to sweep. At the design point of maximum efficiency, a noise reduction can be achieved for a small penalty in propeller efficiency. At the design point of maximum efficiency, a noise reduction of 1.81 dB is achieved for 1 % penalty in propeller efficiency. However, a penalty of 2 % in propeller efficiency results in a noise reduction of 2 dB. This illustrates that the sensitivity of noise reduction reduces as the maximum allowed penalty in propeller efficiency is increased.

This conclusion is further quantified with the gradient of the power fit, which is shown in Figure 8.28. The figure shows the increase in noise emissions for each 1 % increase in propeller efficiency. At the design point of minimum noise, the gradient is approximately $2 \cdot 10^{-5}$ dB per 1 % penalty in efficiency, while at the design point of maximum propeller efficiency, the gradient is 4.48 dB change in TSSP per 1% change in propeller efficiency. The figures shows that penalty to reduce noise emissions is relatively low for propeller designs that are close to the design point of maximum efficiency, while the penalty becomes relatively high for designs that have already achieved a certain reduction in noise emissions. This knowledge can be used to reduce the noise emissions of future propellers more effectively.

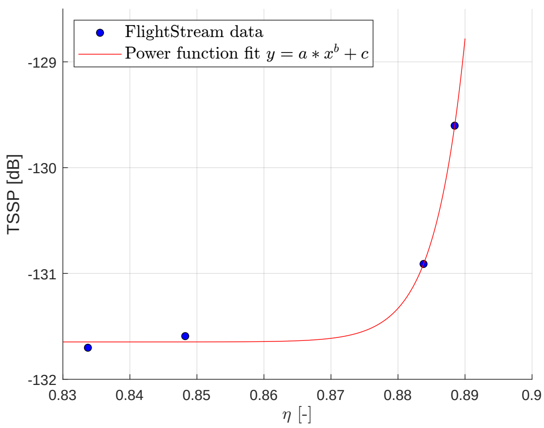

Figure 8.27: Trade-off plot between propeller efficiency and noise for a design vector including sweep based on a Power function fit

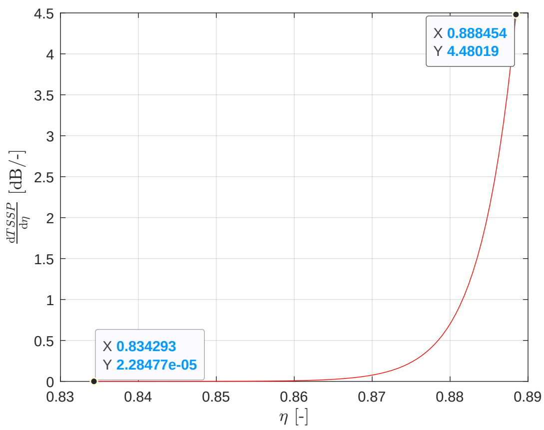

Figure 8.28: Derivative of the power function fit shown in Figure 8.27. The derivative shows the increase in noise emissions for each 1 % increase in propeller efficiency

IV

Conclusion

9 Conclusions and Recommendations

This chapter concludes the work that is performed in this thesis. Seven hundred and sixty-seven blade designs were analyzed successfully to quantify the trade-off between the efficiency and noise of an isolated, unducted propeller. First, the conclusions of the research are presented. Then, recommendations for future work are made.

9.1. Conclusions

The research objective of this thesis was to quantify the trade-off between propeller efficiency and noise for an unducted, isolated propeller by means of a sensitivity study. This objective was achieved successfully, and therefore the main research questions can be answered.

1. *How does sweep affect the propeller aerodynamics and acoustics of an isolated, unducted propeller?*

A sensitivity study was performed between sweep and the propeller efficiency and noise. The results show that thickness noise is dominant. This is striking, considering the low freestream Mach number in the study. Investigation of the loading noise revealed discrepancies in the radial blade loading distributions predicted by the panel method. This means that the loading noise component in the thesis is not predicted accurately. In addition it was found that the spanwise segment width in the study was not constant. However, the acoustic benefit of sweep on the thickness noise component is still captured.

The relation between propeller efficiency and noise of the successfully evaluated designs is analyzed. This shows a spread of 4.4 dB in TSSP and 7.7 % in propeller efficiency. The majority of designs form a point cloud, where the efficiency is in between 80 and 90 %. However, the efficiency of several designs is significantly lower than the point cloud. The difference in TSSP that is seen for the designs implies that the effect of sweep on the thickness noise for conventional propellers at a constant advance ratio is noticeable.

In addition, the effect of the sweep angle on the propeller efficiency and noise has been investigated. It is concluded that a blade with a moderate forward swept mid-segment and backward swept tip is most favorable in terms of propeller efficiency. For the root segment, no distinct relation between the sweep angle and efficiency could be found. The results that are shown are similar to the results in Burger in the case of constant advance ratio. However, in constrast to Burger, in this study no particular relation could be found between the rppt segment sweep angle and the propeller efficiency. The difference in the studies is likely due to the difference in parameterizations.

Analysis of the effect of the sweep angle on the propeller noise shows that for any of the three segments, a higher sweep angle will be more favorable in terms of the noise. A higher sweep angle is associated with a higher mid-chord alignment, which is related to the amount of phase delay. However, as mentioned by Hanson the amount of total noise reduction depends on the relative phase between the stations.

2. *How is the trade-off in propeller efficiency and noise due to sweep for an isolated, unducted propeller quantified?*

The Pareto front between propeller efficiency and noise is represented by four designs. The spread in terms of efficiency is roughly 5.5 %, while the spread in TSSP is 2 dB. A power-law function fit is applied to the results. The gradient is derived to quantify the amount of noise reduction in dB for each % penalty in propeller efficiency. This quantification shows that the amount of noise reduction decreases as the amount of allowable penalty in propeller efficiency is increased. The results highlight that propeller efficiency and noise emissions are conflicting requirements. At the design point of maximum efficiency, the gradient is equal to 4.48 dB change in TSSP for a penalty of 1% in efficiency, while at the design point of minimum noise, the gradient is approximately 2×10^{-5} dB per 1% penalty in propeller efficiency. This shows that the penalty to reduce noise emissions is relatively low for propeller designs that are close to the design point of maximum efficiency, while the penalty becomes relatively high for designs that have already achieved a certain reduction in noise emissions. This knowledge can be used to reduce the noise emissions of future propellers more effectively.

9.2. Recommendations

Based on the work in this thesis, several recommendations for future work are made:

- Future research should validate FlightStream, including the effect of viscosity. In this thesis, an offset was seen at a high advance ratio with respect to experimental data, which is likely due to neglecting viscosity. Validation of the panel method should be performed, including a model that accounts for viscosity, to know more accurately what the modeling error of the panel method is with respect to experimental data.

- Future work should consider alternative flow analysis methods in FlightStream to obtain the radial blade loading distributions. In this thesis, the force export file format was used to estimate the radial blade loading distributions. This file format relies on the pressure mode to compute the force coefficients. However, it was shown that the pressure mode underestimates the forces with respect to the vorticity mode. Furthermore, it is shown that due to discontinuities in the radial blade loading distributions predicted by this mode, the loading noise component is incorrectly estimated. Alternative methods which can be used instead of the force file format are:

  - Probe points or
  - Surface sections

  These are described under the chapter ”Flow analysis” in the FlightStream manual [33].

- Besides considering an alternative flow analysis method, future work should also investigate how the spanwise segment width of the mesh affects the prediction of the forces using this analysis method. In the thesis, it was shown that a uniform spanwise mesh improved the smoothness of the radial blade loading distributions.

- Future work should consider the periodic symmetry modeling option in FlightStream, which uses a periodic boundary condition to model the propeller. If this option is selected, only $1/N$th radial slice of the geometry is required instead of the full geometry mesh. As a result, the memory requirement is reduced by a factor N. Furthermore, the simulation time can also be reduced. Due to time constraints, however, this option was not implemented in this thesis.

- In this study, the effect of blade sweep on the trade-off between the propeller efficiency and the propeller noise was investigated. However, other blade parameters such as the blade number, propeller diameter, or twist can also provide a reduction in noise. Including these parameters can provide valuable insight into propeller noise reduction by design.

- Since this study was focused on isolated propellers, effects due to the installment of the propeller on the aircraft are not considered. Future studies should include these effects to obtain a more realistic estimate of the aerodynamic and acoustic performance of the propeller.

- Structural aspects were not considered in this thesis. The bounds for sweep were based on a similar study. However, it is uncertain whether the designs are structurally feasible. Future studies should include a structural model to assess the feasibility of the propeller design. In addition, by including aeroelastic effects, the estimation of the propeller aerodynamic and acoustic performance is improved.

A

Nacelle Geometry details

A.1. Spinner section

Table A.1: XPROP Spinner dimensions

Section NO	X [mm]	R [mm]
1	0.000	0.000
2	1.906	5.498
3	6.906	11.345
4	11.906	15.374
5	16.906	18.557
6	21.906	21.253
7	26.906	23.627
8	31.906	25.766
9	36.906	27.725
10	41.906	29.537
11	46.906	31.230
12	51.906	32.821
13	56.906	34.325
14	61.906	35.754
15	66.906	37.115
16	71.906	38.417
17	76.906	39.667
18	81.906	40.868
19	86.906	42.025
20	91.906	43.142
21	96.906	44.222

A.2. Tail section

Table A.2: Fuselage tail dimensions

Section NO	X [mm]	R [mm]
1	268.96	44.22
2	270.0085	44.21275
3	273.1255	44.1215
4	278.2258	43.81674
5	285.1705	43.20157
6	293.77	42.22496
7	303.7897	40.86753
8	314.9565	39.13
9	326.9656	37.02648
10	339.4895	34.58073
11	352.1866	31.82368
12	364.7105	28.79178
13	376.7196	25.5256
14	387.8864	22.06866
15	397.9061	18.4665
16	406.5056	14.76618
17	413.4503	11.01693
18	418.5506	7.275814
19	421.6676	3.648905
20	422.7161	1.127952
21	422.8745	0

Bibliography

[1] F. Nicolosi, S. Corcione, V. Trifari, and A. De Marco. "Design and Optimization of a Large Turboprop Aircraft". In: *Aerospace* 8.5 (2021), p. 132. URL: https://www.mdpi.com/2226-4310/8/5/132.

[2] P. Della Vecchia and F. Nicolosi. "Aerodynamic Guidelines in the Design and Optimization of New Regional Turboprop Aircraft". In: *Aerospace Science and Technology* 38 (2014), pp. 88–104. URL: https://linkinghub.elsevier.com/retrieve/pii/S1270963814001515.

[3] R. Singh, G. Ameyugo, and F. Noppel. "Jet engine design drivers: past, present and future". In: *Innovation in Aeronautics* (2012), pp. 56–82.

[4] B. Brelje and J. Martins. "Electric, hybrid, and turboelectric fixed-wing aircraft: A review of concepts, models, and design approaches". In: *Progress in Aerospace Sciences* 104 (2019), pp. 1–19. URL: https://www.sciencedirect.com/science/article/pii/S0376042118300356.

[5] M. D. Moore. "Misconceptions of electric aircraft and their emerging aviation markets". In: *52nd Aerospace Sciences Meeting*. 2014, p. 0535.

[6] J. P. Barnes. "Regenerative electric flight: Synergy and integration of dual-role machines". In: *53rd AIAA Aerospace Sciences Meeting* (2015). URL: https://arc.aiaa.org/doi/abs/10.2514/6.2015-1302.

[7] A. Sakharkar. *Pipstrel Velis Electro, the world's first EASA Type certified electric aircraft*. 2020. URL: https://www.inceptivemind.com/pipistrel-velis-electro-world-first-easa-type-certified-electric-aircraft/13805/.

[8] M. Basner and S. McGuire. *WHO environmental noise guidelines for the european region: A systematic review on environmental noise and effects on sleep*. 2018. URL: https://pubmed.ncbi.nlm.nih.gov/29538344/.

[9] A. Hansell, M. Blangiardo, L. Fortunato, S. Floud, K. de Hoogh, D. Fecht, R. Ghosh, H. Laszlo, C. Pearson, L. Beale, S. Beevers, J. Gulliver, N. Best, S. Richardson, and P. Elliott. "Aircraft noise and cardiovascular disease near Heathrow airport in London: small area study". In: *BMJ* 347.oct08 3 (2013), f5432–f5432. URL: https://www.bmj.com/lookup/doi/10.1136/bmj.f5432.

[10] A. Nassur, D. Léger, M. Lefèvre, M. Elbaz, F. Mietlicki, P. Nguyen, C. Ribeiro, M. Sineau, B. Laumon, and A. Evrard. "Effects of aircraft noise exposure on heart rate during sleep in the population living near airports". In: *International Journal of Environmental Research and Public Health* 16.2 (2019). URL: https://pubmed.ncbi.nlm.nih.gov/30669300/.

[11] C. J. Miller and J. P. Sullivan. "Noise constraints Effecting Optimal Propeller Designs". In: *SAE Gen. Aviat. Aircr. Meet. Expo.* 1985.

[12] O. Gur and A. Rosen. "Optimization of Propeller Based Propulsion System". In: *J. Aircr.* 46.1 (2009), pp. 95–106.

[13] O. Gur and A. Rosen. "Multidisciplinary Design Optimization of a Quiet Propeller". In: *14th AIAA/CEAS Aeroacoustics Conf.* Aeroacoustics Conferences. American Institute of Aeronautics and Astronautics, 2008.

[14] A. Pagano, L. Federico, M. Barbarino, F. Guida, and M. Aversano. "Multi-Objective Aeroacoustic Optimization of an Aircraft Propeller". In: *12th AIAA/ISSMO Multidisciplinary Analysis and Optimization Conference*. American Institute of Aeronautics and Astronautics, 2008, pp. 1–14. URL: http://arc.aiaa.org/doi/10.2514/6.2008-6059.

[15] B. Marinus, M. Roger, and R. Van Den Braembussche. "Aeroacoustic and Aerodynamic Optimization of Aircraft Propeller Blades". In: *16th AIAA/CEAS Aeroacoustics Conference*. American Institute of Aeronautics and Astronautics, 2010. URL: http://arc.aiaa.org/doi/10.2514/6.2010-3850.

[16] D. Ingraham, J. Gray, and L. V. Lopes. "Gradient-based propeller optimization with acoustic constraints". In: *AIAA Scitech 2019 Forum* (2019), pp. 1–12.

[17] S. Burger. "Multi-Fidelity Aerodynamic and Aeroacoustic Sensitivity Study of Isolated Propellers". MA thesis. Delft University of Technology, 2020.

[18] B. G. Marinus. "Multidisciplinary Optimization of Aircraft Propeller Blades". PhD thesis. University Lyon, 2011, pp. 5–8.

[19] M. K. Rwigema. "Propeller Blade Element Momentum Theory with Vortex Wake Deflection". In: *Int. Congr. Aeronaut. Sci.* (2010), pp. 1–9.

[20] O. Gur and A. Rosen. "Comparison between blade-element models of propellers". In: *Aeronaut. J.* 112.1138 (2008), pp. 689–704.

[21] O. Gur and A. Rosen. "A Novel Approach To Actuator Disk Modeling". In: *32nd Eur. Rotorcr. Forum* (2006), pp. 1–35.

[22] E. Branlard, K. Dixon, and M. Gaunaa. "An improved tip-loss correction based on vortex code results". In: *Proc. EWEA–The European Wind Energy Association* (2012).

[23] B. Magliozzi, D. Hanson, and R. Amiet. "Propeller and Propfan Noise". In: *Aeroacoustics of Flight Vehicles: Theory and Practice* 1 (1991), pp. 1–64.

[24] T. Sinnige. "Aerodynamic and Aeroacoustic Interaction Effects for Tip-Mounted Propellers". PhD thesis. Delft University of Technology, 2018.

[25] D. B. Hanson. "Influence of Propeller Design Parameters on Far-Field Harmonic Noise in Forward Flight". In: *AIAA J.* 18.11 (1980), pp. 1313–1319.

[26] L. Erickson. "Panel Methods–An Introduction, NASA Technical Paper 2995". In: *National Aeronautics Space Administration, Washington* (1990).

[27] J. Katz and A. Plotkin. *Low-speed aerodynamics*. 2nd ed. Cambridge University Press, 2001.

[28] J. D. Anderson Jr. *Introduction to Flight*. 7th ed. McGraw-Hill, 2012.

[29] V. Ahuja and R. J. Hartfield. "Aerodynamic Loads Over Arbitrary Bodies By Method Of Integrated Circulation". In: *J. Aircr.* 53.6 (2016), pp. 1719–1730.

[30] D. L. Ashby, M. R. Dudley, S. K. Iguchi, L. Browne, and J. Katz. *Potential Flow Theory and Operation Guide For The Panel Code PMARC_14*. Tech. rep. NASA, 1999.

[31] N. Curle. "A Two-Parameter Method for Calculating the Two-Dimensional Incompressible Laminar Boundary Layer". In: *The Journal of the Royal Aeronautical Society* 71.674 (1967), pp. 117–123.

[32] J. F. Nash and J. G. Hicks. "An Integral Method Including the Effect of Upstream History on the Turbulent Shear Stress". In: *Proceed. AFOSR-IFP-Stanford Conference*. Stanford University Press, 1969.

[33] R. in Flight inc. *FlightStream User Guide Version 2020.2*. `https://researchinflight.com/Manual/Version_2020_2/`, Accessed on 10-10-2021. 2020.

[34] Q. Li, K. Öztürk, T. Sinnige, D. Ragni, G. Eitelberg, L. Veldhuis, and Y. Wang. "Design and experimental validation of swirl-recovery vanes for propeller propulsion systems". In: *AIAA J.* 56.12 (2018), pp. 4719–4729.

[35] M. Drela and H. Youngren. *XFOIL 6.9 User Primer*. `https://web.mit.edu/drela/Public/web/xfoil/xfoil_doc.txt`, Accessed on 6-8-2021. 2001.

[36] D. Hanson. "Helicoidal Surface Theory for Harmonic Noise of Propellers in the Far Field". In: *AIAA J.* 18.10 (1980), pp. 1213–1220.

[37] A. Parry and D. Crighton. "Theoretical prediction of counter rotating propeller noise". PhD thesis. University of Leeds, 1988.

[38] D. Hanson. *Unified aeroacoustics analysis for high speed turboprop aerodynamics and noise - Volume I: Development of Theory for Blade Loading, Wakes and Noise*. Tech. rep. NASA, 1991.

[39] W. de Haan. "Impact of Blade Sweep on Aerodynamic and Aeroacoustic Performance Optimization of Isolated Propellers". MA thesis. Delft University of Technology, 2021.

[40] X. Geng, T. Hu, P. Liu, T. Sinnige, and G. Eitelberg. “Analysis of Thrust-Scaled Acoustic Emissions of Aircraft Propellers and their Dependence on Propulsive Efficiency”. In: *ICAS* (2021).

[41] C. A. Negulescu. “Airbus AI-PX7 CROR Design Features and Aerodynamics”. In: *SAE International Journal of Aerospace* 6.2 (2013).

[42] G. Farin. *Curves and surfaces for computer-aided geometric design: a practical guide*. Elsevier, 2014.

[43] Y. Seo, H. Kim, and S. Youn. “Shape optimization and its extension to topological design based on isogeometric analysis”. In: *Int. J. Solids Struct.* 47.11-12 (2010), pp. 1618–1640.

[44] J. Sobieszczanski-Sobieski, A. Morris, and M. van Tooren. *Multidisciplinary Design Optimization Supported by Knowledge Based Engineering*. 1st. Wiley, Ltd., 2015, pp. 1–378.

[45] J. H. Wei. “Parametric modelling for determining aircraft stability & control derivatives”. MA thesis. Delft University of Technology, 2016. URL: https://repository.tudelft.nl/islandora/object/uuid%3Acd095318-3272-400a-822d-e7990480a904?collection=education.

[46] https://www.salome-platform.org/, Accessed on 30-9-2021. 2021.

[47] T. Santner, B. Williams, and W. Notz. *The Design and Analysis of Computer eExperiments*. 2nd. Springer, 2003, p. 279.

[48] A. Keane and N. Prasanth. *Computational Approaches for Aerospace Design*. 1st. John Wiley & Sons, Ltd, 2005, p. 606.

[49] A. Giunta, S. Wojtkiewicz, and M. Eldred. “Overview of modern design of experiments methods for computational simulations”. In: *41st Aerospace Sciences Meeting and Exhibit*. 2003, p. 649.

[50] W. Morokoff and R. Caflisch. “Quasi-random sequences and their discrepancies”. In: *SIAM Journal on Scientific Computing* 15.6 (1994), pp. 1251–1279.

[51] A. Owen. “Scrambled net variance for integrals of smooth functions”. In: *The Annals of Statistics* 25.4 (1997), pp. 1541–1562.